2019-04-01

Analysis of Distortion Transfer and Generation through a Fan and a Compressor Using Full-annulus Unsteady RANS and Harmonic Balance Approaches

Daniel Robert Soderquist
Brigham Young University

BYU ScholarsArchive Citation
Soderquist, Daniel Robert, "Analysis of Distortion Transfer and Generation through a Fan and a Compressor Using Full-annulus Unsteady RANS and Harmonic Balance Approaches" (2019). *All Theses and Dissertations*. 7401.
https://scholarsarchive.byu.edu/etd/7401

Analysis of Distortion Transfer and Generation Through a Fan and a Compressor Using Full-Annulus Unsteady RANS and Harmonic Balance Approaches

Daniel Robert Soderquist

A thesis submitted to the faculty of
Brigham Young University
in partial fulfillment of the requirements for the degree of

Master of Science

Steven E. Gorrell, Chair
S. Andrew Ning
R. Daniel Maynes

Department of Mechanical Engineering

Brigham Young University

ABSTRACT

Analysis of Distortion Transfer and Generation Through a Fan and a Compressor Using Full-Annulus Unsteady RANS and Harmonic Balance Approaches

Daniel Robert Soderquist
Department of Mechanical Engineering, BYU
Master of Science

Understanding distortion transfer and generation through fan and compressor blade rows is able to assist in blade design and performance prediction. Using full annulus unsteady RANS simulations, the effects of distortion as it passes through the rotor of a transonic fan at five radial locations (10%, 30%, 50%, 70%, and 90% span) are analyzed. The inlet distortion profile is a 90-degree sector with a 15% total pressure deficit. Fourier distortion descriptors are used in this study to quantitatively describe distortion transfer and generation. Results are presented and compared for three operating points (near-stall, design, and choke). These results are used to explain the relationship between inlet total pressure distortion, pressure-induced swirl, total pressure distortion transfer, total temperature distortion generation, and circumferential rotor work variation. It is shown that very large changes in pressure-induced swirl and distortion transfer and generation occur between near-stall and design, but only small changes are seen between design and choke. The greatest changes are shown to be near the tip. Local power variations are shown to correlate with total pressure distortion transfer and total temperature distortion generation.

It can be difficult to predict the transfer of distortion through a fan or compressor because traditional experimental and computational methods are very expensive and time consuming. The Harmonic Balance approach is a promising alternative which uses Fourier techniques to represent fluid flow solutions and which can provide unsteady solutions much more quickly than traditional unsteady solvers. Relatively little work has been done to assess how much Fourier information is necessary to calculate a sufficiently accurate solution with the Harmonic Balance Solver. A study is performed to analyze the effects of varying the amount of modal content that is used in Harmonic Balance simulations. Inlet distortion profiles with varying magnitudes are used in order to analyze trends and provide insight into the distortion flow physics for various inlet conditions. The geometry is a single stage axial compressor that consists of an inlet guide vane followed by the NASA Stage 37 rotor. It is shown that simulations with greater magnitudes of distortion require more modal content in order to achieve sufficiently accurate results. Harmonic Balance simulations are shown to have significantly lower computational costs than simulations with a conventional unsteady solver.

Keywords: distortion, URANS, harmonic balance, Fourier, modes, efficiency, pressure ratio, work, power, swirl, operating point, stall, choke

ACKNOWLEDGMENTS

I wish first to thank my graduate advisor Dr. Steven E. Gorrell for granting me an opportunity to study jet engines on a graduate level and for being an invaluable mentor to me throughout the process. He was patient and encouraging when I encountered obstacles and setbacks. Most importantly, he taught me through words and example that my family is so much more valuable than my work.

I would also like to thank the others on my committee, Dr. S. Andrew Ning, and Dr. R. Daniel Maynes for taking the time to assess my work and offer guidance along the way. I am also grateful for the many other faculty members and fellow students at BYU who inspired in me an excitement for learning and helped me to succeed.

I gratefully acknowledge the Fulton Supercomputing Lab at BYU for supporting this effort with generous allocations of computer resources. I am also grateful for the technical expertise of Dr. Michael List of the Air Force Research Lab and Dr. Chad Custer of Siemens.

Finally, I wish to thank my wife Rachel for loving me and supporting me wholeheartedly in this adventure, and my daughter Mae for joining our family and brightening up our lives this last year.

TABLE OF CONTENTS

LIST OF TABLES

LIST OF FIGURES

NOMENCLATURE

A	Area
a_f	Face area vector
BR	Number of blade rows
c_p	Specific heat evaluated at constant pressure
E_n	Fourier coefficient for energy
e_1	Specific energy
η_f	Fan Efficiency
γ	Ratio of specific heats
h	Height
j	Operator used to show complex number
$\dot{m}$	Mass flow rate
N	Total number of Fourier modes
N_1	Rotational speed in rad/s
$N_{effective}$	Effective number of cells in mesh
N_i	Number of cells in a given blade row
n	n-th mode of the Fourier series expansion
ω	Frequency of an unsteady disturbance
p	Fundamental period of a repeating profile
P	Static pressure
PD	Percent distortion
ϕ	Fourier modal phase
ϕ_f	Face value of a selected scalar (efficiency or pressure ratio)
PR	Pressure Ratio
P_t	Total or stagnation pressure
R_n	Fourier coefficient for mass
r	Radius
ρ	Density
ρ_f	Face density
s	Summation of Fourier series terms
ΣA	Total Fourier amplitude
θ	Circumferential location around the fan annulus
T_t	Total or stagnation temperature
TL_i	Number of time levels associated with a blade row
t	time
U	Blade speed
U_n	Fourier coefficient for x-momentum
u	Velocity in x-direction
V_{axial}	Axial component of velocity
V_n	Fourier coefficient for y-momentum
V_{tang}	Tangential component of velocity
v_f	Face velocity vector
v	Velocity in y-direction
$\dot{W}$	Power

CHAPTER 1. INTRODUCTION

Inlet flow distortion is a critical concept in jet engine design because it greatly affects an engine's overall performance. Inlet distortion is a non-uniform distribution of flow properties at the entrance to the first fan or compressor stage of an engine. This distortion may be caused by curvature in the duct leading to the compressor, flying at high angles of attack, ingestion of missile exhaust, ingestion of hot gas from vertical take-off/landing, and interactions between the engine and the body of the airplane such as ingested boundary layers in embedded engines. Inlet distortion is usually characterized by one or more regions of low total pressure. (Visualization of a distorted total pressure field at a compressor inlet is shown in Figure 1.1.) As this total pressure distortion transfers through the compressor, the rotating blade rows perform non-uniform work on the fluid. The local work often varies both radially and circumferentially. This uneven distribution of work generates additional distortion in the form of total temperature. These non-uniform effects also vary based on the operating point of the fan or compressor. All of these effects can significantly impact the overall performance of a jet engine.

The ability to describe and quantify distortion as it progresses through a fan or compressor when subject to inlet distortion is very valuable during the design process because it can help guide designers to make improvements to predict engine performance and better handle distortion. For example, if designers know the local pressure rise as well as the blade loading and local power for multiple operating points at various locations within a fan or compressor, then they can begin to understand the sensitivity of a design to inlet distortion. This could ultimately lead to tools that predict performance based on distortion without needing to run high-fidelity simulations. Additionally, these tools could help designers to more quickly see how changes in the design will affect the stall margin. This would allow designers to examine more of the design space to find a design that minimizes losses in stall margin due to distortion.

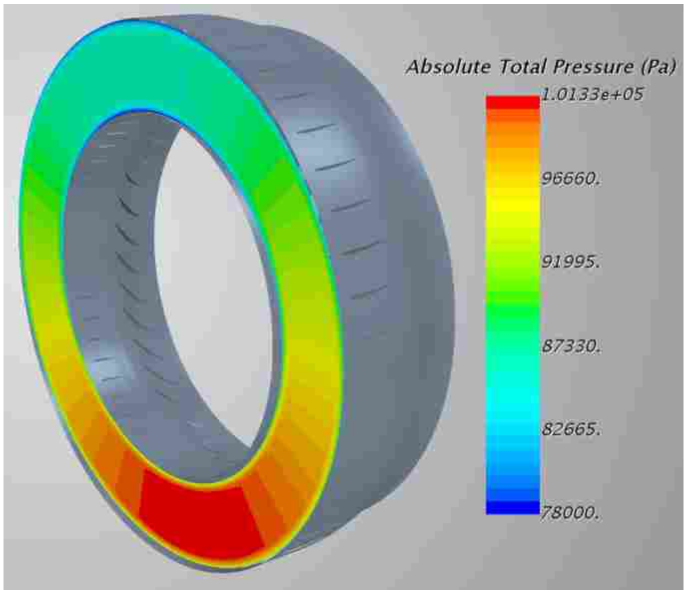

Figure 1.1: Example of inlet distortion on a compressor. The total pressure field is non-uniform at the inlet.

Conventional methods for determining the amount of distortion transfer and generation have many limitations. Physical experimentation has long been used in the research and development of jet engines. It often gives valuable insight into the flow physics of distortion, but it is very time-consuming and the necessary hardware is expensive. Analytical methods can be relatively quick and inexpensive, but they don't provide the necessary accuracy for most scenarios. Computational Fluid Dynamics (CFD) methods such as Unsteady Reynolds Averaged Navier-Stokes (URANS) solvers have been shown to accurately capture distortion, but the required computing resources often limit their effectiveness [1–3].

The Harmonic Balance (HB) technique is a CFD method that has recently been applied to turbomachinery problems involving inlet distortion. The HB solver can accurately capture both distortion transfer and generation through turbomachinery for a fraction of the computational cost that a URANS simulation would require.

For turbomachinery applications, the HB technique requires that a number of modes or harmonics be specified at the inlet boundary and at each blade row. A mode in this sense is a per-rev component of distortion. If one mode is specified at a location, then the solver considers only the 1-per-rev component of distortion in the calculations at that location, and it passes only this information on to the other blade rows. If two modes are specified at a location, then the solver considers both the 1-per-rev and the 2-per-rev components of distortion, and it passes all of this information on to the other blade rows. In other words, the number of modes is the number of terms from the Fourier series approximation that are used in the calculations in a blade row and passed on to the other blade rows. As greater numbers of modes are specified, the overall solution is expected to become more accurate; however, using more modes generally causes a longer solve time, and so it is desired to use the minimum amount of modes that will give sufficiently accurate results. The convention for referring to a mode combination is to state the numbers of modes in order of the direction of flow. For example, an HB simulation that uses three (3) modes for the inlet, two (2) modes for the first blade row, and one (1) mode for the second row would be referred to as an HB321 simulation. This example is illustrated in Figure 1.2.

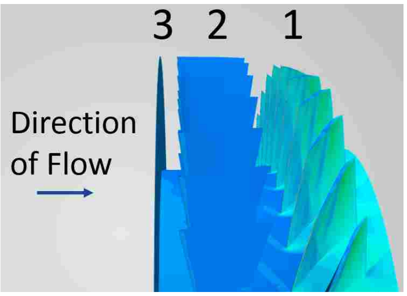

Figure 1.2: Example illustrating the convention for referring to an HB mode combination for the blade rows in a compressor. This combination would be referred to as HB321.

It is important to understand that the number of modes included in a blade row does not limit the amount of distortion information that the upstream or downstream locations impart on the flow. For example, if five modes are included at the inlet boundary, and zero modes are included in each blade row (HB500), this does not mean that the flow will be uniform after passing through the blade rows. Effects of the components of distortion calculated at the inlet boundary will still be present after passing through the blade rows. This is illustrated in Figure 1.3 which is taken from Marshall Peterson's thesis [4]. When no rotor or stator modes are included (Figure 1.3a, HB500), the wakes from the rotor blades are attenuated at the end of the first blade row, but the effects of the main inlet distortion components can be seen throughout the entire domain. When five modes are included in the rotor blade row (Figure 1.3b, HB550), both the effects of the inlet distortion and the rotor blade row wakes can be seen throughout the entire domain.

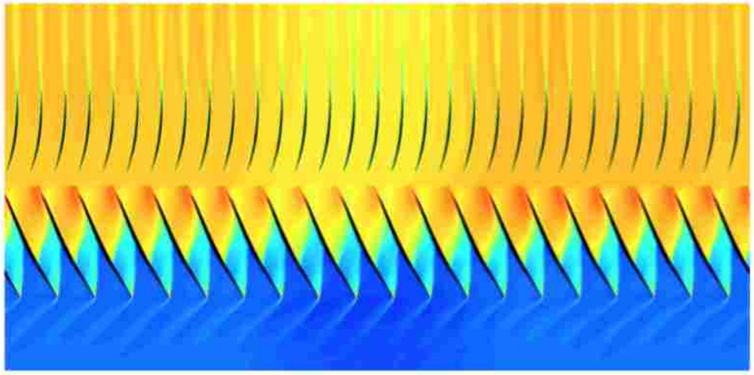

(a) Without rotor modes (0-0).

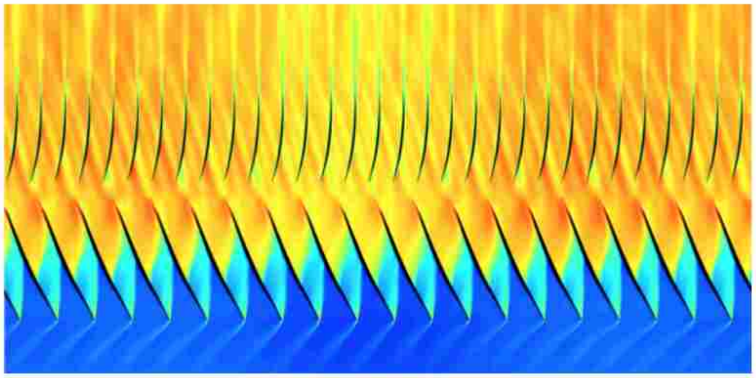

(b) With rotor modes (5-0).

Figure 1.3: Example illustrating that the number of modes in a blade row does not limit the amount of distortion information passed on from other locations. Flow is traveling in the upward direction. Taken from Marshall Peterson's thesis. [4]

In a recent study that was performed to determine recommendations for applying the HB solver to capture total pressure and total temperature distortion, simulations were run for three different combination of modes [4, 5]. Much, however, can still be done to assess how many modes are required for sufficiently accurate solutions in different scenarios. Such scenarios include different rotor geometries, greater magnitudes of distortion, and different shapes of distortion. It is also of interest to know what trends can be found in distortion descriptor values based on mode combinations.

In addition to analyzing trends with HB mode combination, it is of interest to understand how distortion results vary both radially and with operating point. Hub and tip effects often have a great effect on distortion amplitude and phase shift. Similarly, whether the simulations are being run at a near-stall operating point versus in choke can impact the results greatly. An analysis of the relationships between total pressure, total temperature, swirl, and power at various operating points could offer valuable insight for fan/compressor designers. A full-annulus unsteady solver is more suitable to analyze the radial variations and the operating point effects than an HB solver because using a full-annulus unsteady solver eliminates the dependency of the results on the HB mode combination.

The purpose of this thesis is to increase the understanding of distortion flow physics through a fan or a compressor and to determine quicker methods to achieve convergence for simulations involving inlet distortion. This will be accomplished by completing the following objectives:

- Present and analyze distortion results for a distorted Full-Annulus URANS simulation of Parametric Blade Study (PBS) Rotor 4 at five evenly-spaced radial locations and at three operating points to offer insight into how distortion flow physics vary radially and with operating point. Examine swirl, total pressure, and total temperature. The three operating points are near-stall, design, and choke.

- Introduce two methods of quantifying spatial variations of power within a fan or compressor. Use these methods to analyze power variations inside Rotor 4, and examine the relationships between swirl, power, total pressure, and total temperature.

- Perform HB and Full-Annulus URANS simulations of NASA Rotor 37 with varying profiles of inlet total pressure distortion. Present and analyze trends in Fourier distortion descriptor values, efficiency values, and total pressure ratios as inlet distortion profile is varied. Analyze how the application of the URANS solver and the HB solver affects the solutions. Determine recommendations of HB mode combinations that ought to be specified for various inlet boundary distortion profiles based on the simulations of NASA Rotor 37. Vary magnitude and shape of distortion. Use three magnitudes and two shapes.
- Compare conclusions from this NASA Rotor 37 study to some of the conclusions from Peterson's PBS Rotor 4 study [4]. Specifically compare conclusions of HB mode recommendations and trends in distortion descriptors with respect to mode combinations. Based on comparisons of these two studies, make overall recommendations for applying the HB solver to simulations with inlet distortion.

The thesis proceeds in the following manner: First, a literature review is presented to provide necessary background information about inlet distortion and turbomachinery. Next, the methodology of this thesis is outlined including mesh generation, boundary conditions, solver parameters, and power approximation methods. Results are then presented first for the study involving PBS Rotor 4, and second for the study involving NASA Rotor 37. Finally, conclusions are drawn from the results.

CHAPTER 2. BACKGROUND AND LITERATURE REVIEW

This chapter gives applicable history and background of previous work to provide a foundation for the research presented in this thesis. This includes a description of causes of inlet distortion as well as the analytical, experimental and computational efforts that have been made to predict and analyze the effects of distortion.

2.1 Causes of Inlet Distortion

Inlet distortion was first recognized as a concern in the 1960s when jet engine designers noticed that the total pressure profile at the inlet affected the performance of the engine [6]. Later, total temperature distortions were noticed to also have an effect. The distortion adversely affected the efficiency, pressure ratio, and mass-flow rate, and it caused unfavorable structural responses. The non-uniform total pressure and total temperature properties were found to have several causes including curvature in the duct leading to the compressor, interactions between the engine and the body of the airplane, high angles of attack, and ingestion of missile exhaust [7].

A generic curved inlet with an embedded engine is depicted in Figure 2.1. The sharp bends in a curved duct can create adverse pressure gradients that cause the boundary layer to separate. When this happens, the total pressure flow field can be significantly distorted. If the boundary layer does not separate, the curvature can still cause distortion due to its longer length of duct which causes local variations in boundary layer growth around the duct [7]. Figure 2.2 shows the formation of regions of low total pressure in a generic curved duct.

Swirl distortion is another form of distortion that often accompanies total pressure and total temperature distortion. Swirl is defined as the flow angle with respect to the axial direction.

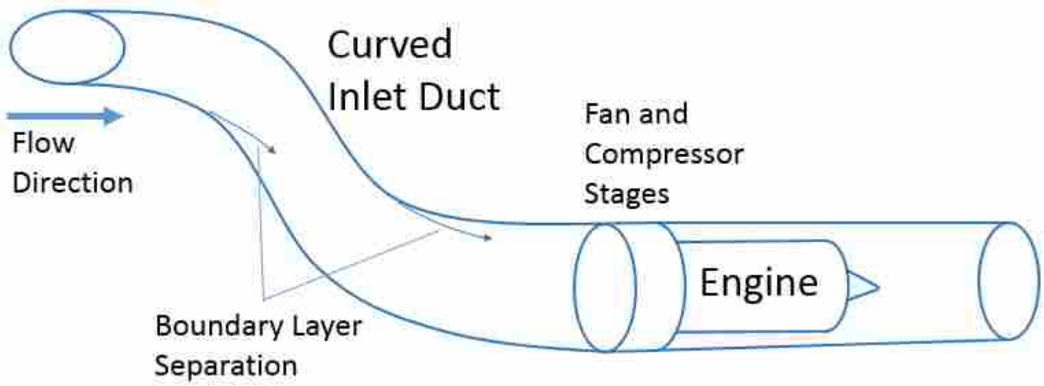

Figure 2.1: Visualization of a curved inlet duct to a jet engine. The sharp curves in the duct can cause boundary layer separation which distorts the flow field.

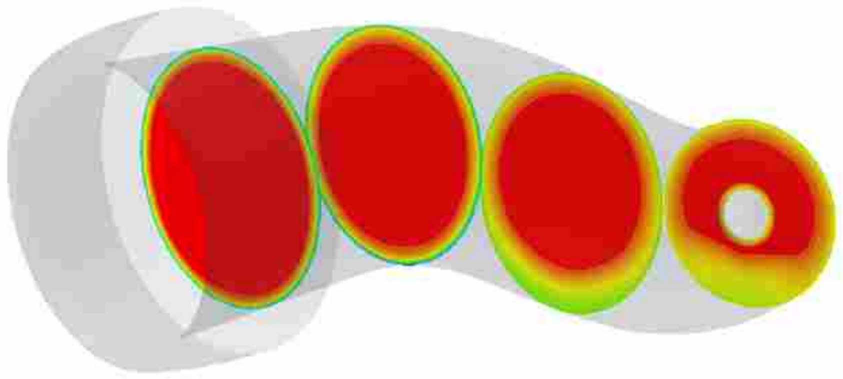

Figure 2.2: Visualization of the formation of total pressure distortion due to duct curvature. Red, green, and blue represent the high, medium, and low values of total pressure, respectively.

Figure 2.3 is a graphic that shows how circumferential swirl is defined. When the swirl angle for a cross-section of an engine is non-uniform, this location contains swirl distortion.

2.2 Off-Design Performance of Fans and Compressors

In the development of fans and compressors, it is important to consider performance at operating points far from design. A typical performance map for a fan or compressor is shown in Figure 2.4. On a given rotational speed line, as mass flow is increased, pressure ratio decreases until the flow becomes choked (the flow reaches mach 1). At this point, mass flow rate can increase no further even if back pressure continues to decrease. By contrast, as mass flow is decreased,

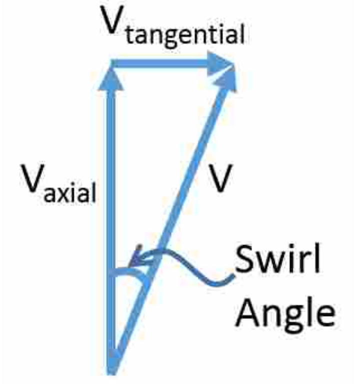

Figure 2.3: Swirl is the angle between the velocity vector and the axial component of velocity.

pressure ratio increases. The rate of increase of pressure ratio decreases for progressively lower mass flow rates until the stall line is reached. At operating points past the stall line, the exact behavior of the flow becomes difficult to predict. Separation occurs and inhibits the blades' ability to do work. This can lead to abrupt drops in pressure ratio and other undesirable effects. Extreme cases result in violent reversed flow known as surge. To reduce the risk of unanticipated stall or surge, the design operating line is defined such that there is an acceptable margin (known as stall margin) between the operating line and the stall line.

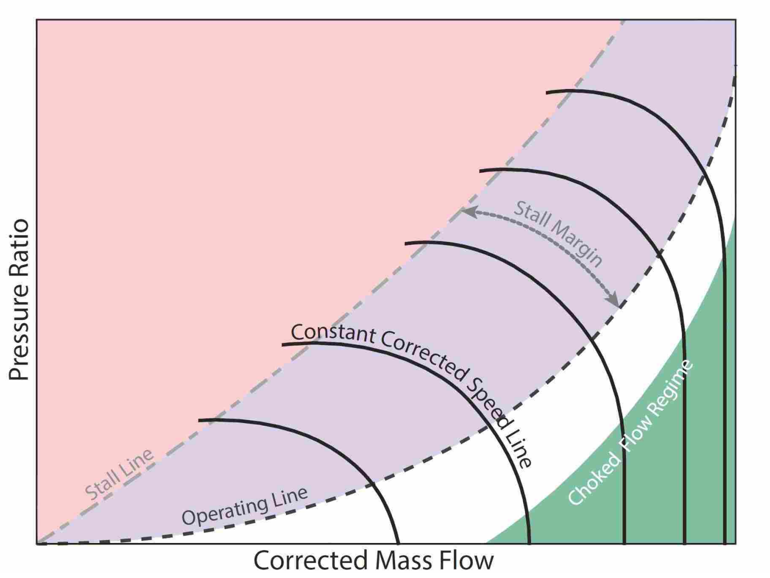

Figure 2.4: Typical performance map for a fan or a compressor.

2.3 Analytical and Experimental Methods for Predicting Effects of Distortion

Since the discovery that inlet distortion can affect the performance of turbomachines, many analytical and experimental methods have been developed and used to predict those effects on performance. These methods have provided great insight, but they also have several limitations in this application.

In 1959, Pearson and McKensie introduced a method they called the parallel compressor theory [8]. In this analytical method a distorted inlet profile is approximated by considering multiple compressors, each having a different uniform inlet profile such that each of the regions of low or high total pressure in the distorted inlet profile is accounted for. Figure 2.5 illustrates a simple application of the parallel compressor theory. The example distorted inlet profile has a low total pressure region (represented in blue) and a high total pressure region (represented in red) that are the same size. The average of these two pressures would correspond to the clean inlet total pressure. In order to predict the resulting pressure ratio for the distorted inlet profile, the pressure ratio for the compressor is calculated for three uniform flow cases: the low inlet, high inlet, and clean inlet total pressures. Then, the pressure ratio of the distorted inlet is predicted by connecting the operating points for the low and high inlet total pressures with a line and then finding the point on that line with the same corrected mass flow as the clean inlet operating point. This method has shown to be fairly accurate at predicting performance of fans and compressors with relatively simple inlet distortion profiles.

In 1969, Reid showed a limitation of the parallel compressor theory in that certain profile types gave inaccurate results (particularly those with small extents of distortion) [9]. In 2011, Cousins and Davis performed two studies to evaluate the ability of a modified parallel compressor theory to handle complex inlet distortion profiles [10, 11]. They concluded that radial distortion effects are difficult for the parallel compressor theory to calculate with enough accuracy to be effective. They found that this was particularly true if hub radial distortion effects were of interest in a system that stalls near the tip.

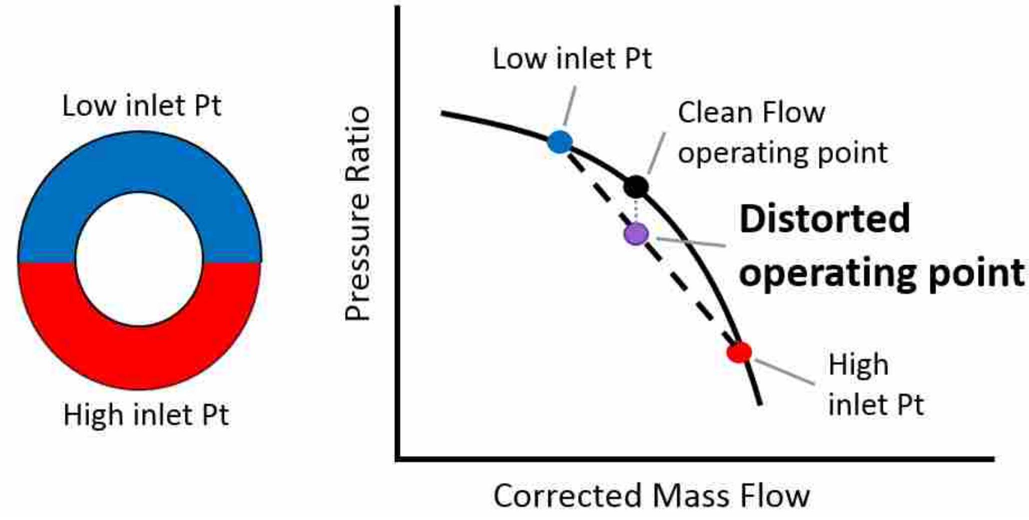

Figure 2.5: Example of an application of the parallel compressor theory. Pt stands for total pressure.

Many experimental methods have also been used since the 1960s to help predict the effects of inlet distortion. For these studies, distorted inlet conditions are usually created by placing screens or swirl generators at the fan inlet or by connecting a curved inlet duct to the fan. In 1971, Calogeras, Mehalic, and Burstadt performed a study in which they found correlations between the performance of a particular compressor and a circumferential distortion index. They found that hub radial distortion affected the pressure ratio and the corrected mass flow of the compressor but not the stall margin, whereas tip radial distortion affected the stall margin but not the pressure ratio nor the corrected mass flow [12].

Rademakers, Bindl, and Niehaus performed a similar experimental study investigating effects of swirl and total pressure distortion on performance and stability [13] of a jet engine. They found that swirl distortion affected the compressor's efficiency, but that the specific fuel consumption (SFC) of the entire engine was mainly affected by inlet total pressure distortion. They also found that swirl distortion tended to have a positive influence on a compressor's stability at low rotational speeds. Finally, they concluded that both the pressure ratio for the compressor and the SFC were linearly related to the amount of applied total pressure distortion.

These experimental studies have added valuable insight, but they can be relatively expensive to perform. It takes significant time and money to set up an experimental facility to get useful results. Also, the amount of data that can be acquired is limited by the number of transducers that can be placed in the facility, and if too many transducers are added, then they begin to affect the flow field thus impacting the results.

2.4 CFD Methods for Predicting Effects of Distortion

Computational methods have become increasingly useful for analyzing turbomachinery in recent decades, but only certain types of CFD solvers can account for inlet distortion. Steady-state mixing plane solvers for example can be very computationally efficient, but they cannot account for inlet distortion because inlet distortion is inherently an unsteady phenomenon.

In 2010, Yao, Gorrell, and Wadia demonstrated that unsteady solvers such as full-annulus URANS solvers can accurately capture distortion [2, 3]. They simulated flow through two multi-stage fans and analyzed total pressure distortion transfer and total temperature distortion generation through the blade rows. The applied inlet distortion profile was a 1-per-rev sinusoidal distribution of total pressure. For both fans, the amplitude, phase, magnitude, and shape results of total pressure and total temperature agreed well with experimental data. They also found that total pressure distortion was amplified through the first stages of the fan rather than being mixed out. At the leading edge of the final stator blade, however, they found that the distortion was attenuated. They attributed this to the constant pressure boundary condition imposed at the outlet. This study concluded that full-annulus URANS solvers could serve as a valid and valuable resource for capturing distortion transfer and generation as well as performance for a fan or compressor subject to inlet distortion.

Full-annulus URANS solvers have helped immensely in distortion analysis because they can handle complex inlet profiles, and they can provide data at all locations within a compressor or fan. They have helped in understanding the spatial phase differences between total pressure and total temperature profiles and some of the radial variations of properties in distorted flow. A limitation with these URANS solvers is that they often require tremendous computing resources and can take several weeks to deliver accurate solutions.

2.4.1 CFD Research of Pressure-Induced Swirl and Radial Migration

As high-fidelity URANS solvers have been employed for inlet distortion scenarios, they have provided valuable insight into the interactions between inlet distortion and fans as well as the mechanisms that drive these interactions. Two significant findings include the development of pressure-induced swirl and radial migration.

Pressure-induced swirl occurs because a distorted total pressure field with a region of low total pressure creates a static pressure gradient. This static pressure gradient creates a force imbalance that needs to be resolved. For the length of the inlet duct to the hub and the fan, this force imbalance causes a mass redistribution in the circumferential direction. Tangential components of velocity are induced causing swirl in the direction from high to low pressure on either side of the distorted region. These local variations of swirl affect the blade incidence angles of the flow causing non-uniform work to be performed by the fan blades. The swirl variations have been shown to be more severe near the hub than near the tip for multiple fan geometries [14, 15].

Figure 2.6 shows swirl and static pressure contours at 50% span for a fan with inlet distortion from a study by Yao, Gorrell, and Wadia [1, 16] in 2007-08. Near 280 degrees there is a transition region from high pressure on the right side to low pressure on the left side, which causes swirl from right to left in this view. Because the swirl is in the direction of blade rotation, it is labeled as positive swirl. Near 80 degrees, there is a transition from high pressure on the left side to low pressure on the right side which causes swirl in the direction opposite the blade rotation. This region is labeled as negative swirl in the figure.

Another effect of the distorted pressure field at the inlet is that the stagnation point becomes slightly offset from the point of the nose cone. This was observed by Fidalgo, Hall, and Colin [15] in 2012. They found that the stagnation point is offset in the direction opposite the distorted sector. This causes a radial force imbalance which induces radial mass redistribution (aka radial

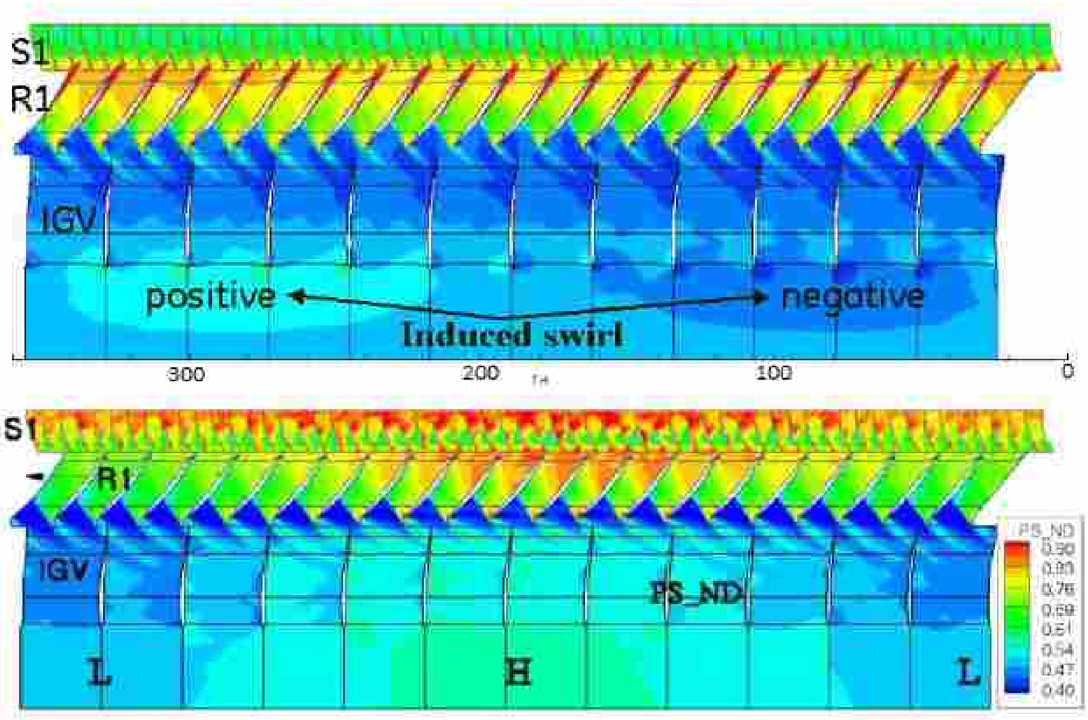

Figure 2.6: Top: Swirl contours at 50% span for a multistage fan with inlet distortion. Flow is in the upward direction in this unwrapped view. Bottom: Static pressure contours at the same location. Note that from this view, the blades travel from right to left. [1]

migration) near the hub. The flow travels from the clean region over the center of the nose cone into the distorted region. This phenomenon is shown in the plots from Fidalgo, Hall, and Colin's study in Figure 2.7.

2.4.2 Harmonic Balance CFD

In the early 2000s, Harmonic Balance was applied to turbomachinery CFD [17–21]. The HB method uses Fourier techniques to transform the Navier-Stokes equations from the time domain to the frequency domain. This is done by taking the flow variables for conservation of mass, axial and circumferential momentum, and energy, and re-expressing them each as a Fourier series in time with spatially varying coefficients. Equation 2.1 shows these representations for the 2D mass, momentum, and energy terms of the Navier-Stokes equations. In theory, the summations of these terms would be over all integer values of n, but in practice only a few terms are kept in

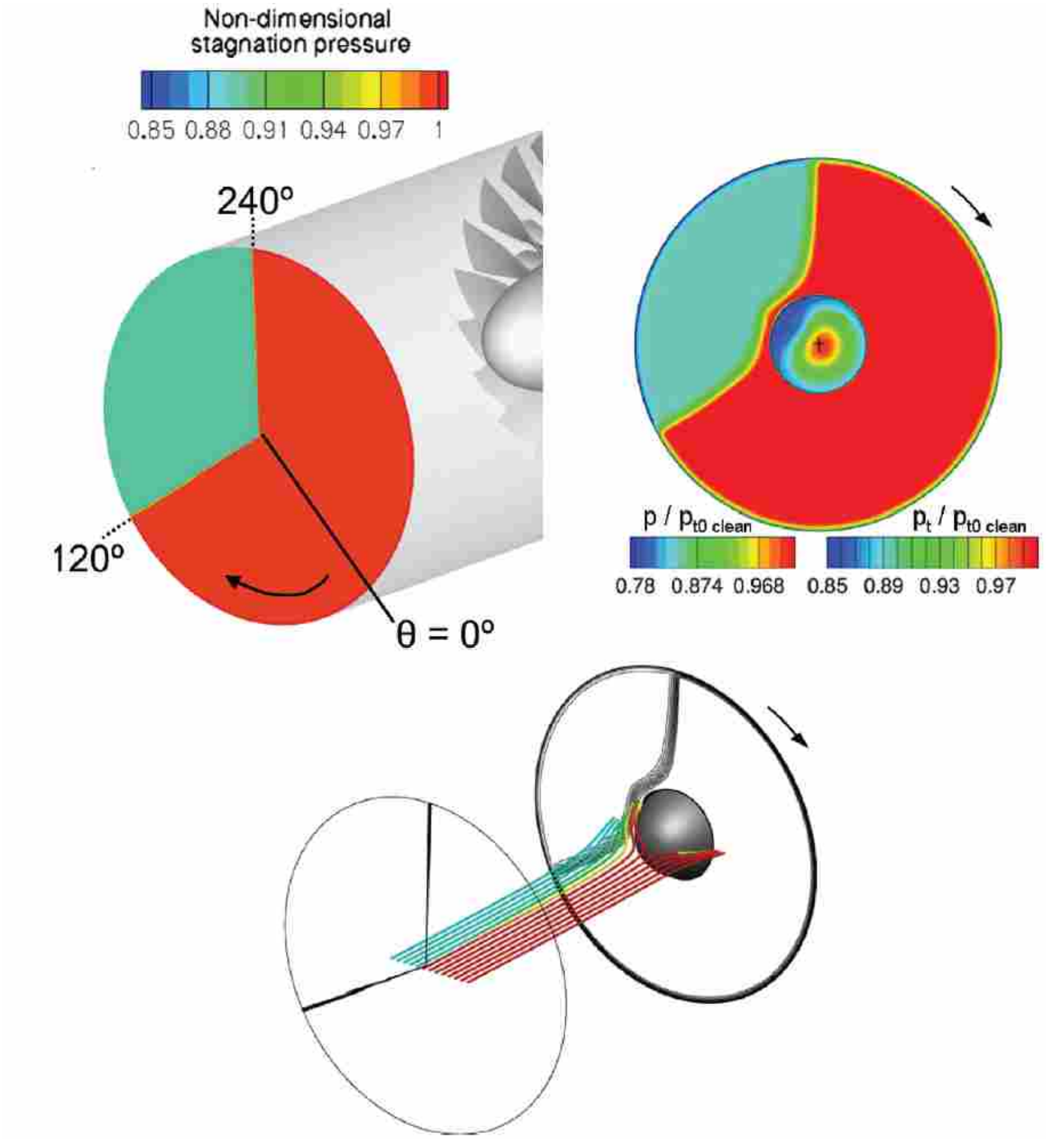

Figure 2.7: Top Left: Applied total pressure distortion profile at entrance of a fan inlet duct. Top Right: Total pressure contours at a location slightly upstream of the fan blade leading edge. The center circle shows the static pressure contours for the hub/spinner up to that location. The stagnation point is offset from the center of the nose cone. Bottom: Streamlines illustrating that flow from the clean region migrates across the center of the nose cone into the location of the distorted region. Color of streamlines corresponds to total pressure magnitude. [15]

order to achieve the necessary accuracy for a given application. With the mass, momentum, and energy terms represented as Fourier series in time, the Navier-Stokes equations are re-written in the frequency domain.

$$\rho(x,y,t) = \sum_{n=1}^{N} R_n(x,y)e^{j\omega nt} \tag{2.1}$$

$$\rho u(x,y,t) = \sum_{n=1}^{N} U_n(x,y)e^{j\omega nt} \tag{2.2}$$

$$\rho v(x,y,t) = \sum_{n=1}^{N} V_n(x,y)e^{j\omega nt} \tag{2.3}$$

$$\rho e_1(x,y,t) = \sum_{n=1}^{N} E_n(x,y)e^{j\omega nt} \tag{2.4}$$

Within the frequency domain, the Navier-Stokes equations are solved using steady techniques which often accelerate convergence compared to conventional time-marching methods. The results can then be transformed back to the time domain for post-processing. In short, the HB method uses faster techniques than conventional URANS methods to account for nonlinearities in both space and time making it ideal for periodic unsteady flows such as those found in turbomachinery. The accuracy of the HB method is determined by how many terms (modes) of the Fourier series are included in the calculations in each part of the domain. Including more modes generally results in greater accuracy but longer solve times. For more explanation about how the HB method works, and particularly the concept of mode combinations, see Figure 1.2 and its accompanying discussion.

Another benefit provided by the HB method is that unsteady results can be calculated for the full-annulus while only meshing one blade passage in each blade row. This is made possible by the fact that the solution within a given blade passage only differs from the solution of the adjacent passages in the same blade row by a quantity described by Hall et al. called the interblade phase angle [17]. The HB method accounts for this quantity by the use of Fourier modes. Minimizing mesh size decreases the time to convergence making the HB method even more attractive for turbomachinery simulations.

Marshall Peterson performed extensive research on the HB solver's ability to capture distortion transfer and generation in the simulation software STAR-CCM+ [4, 5] in 2016. He showed that the HB solver can accurately capture both distortion transfer and generation through a transonic fan for a fraction of the computational cost that a URANS simulation would require. He also showed that the HB solver could predict fan performance with distorted inlet conditions very well. In order to best capture distortion transfer and generation through a fan, he found that it was most important to adequately capture the inlet profile by specifying several modes at the inlet boundary. (He recommended three modes at the inlet for the sector-shaped profile he simulated.) He found that the number of modes in the blade rows had negligible effect on the accuracy of his distortion transfer and generation predictions suggesting that the blades did not impart appreciable amounts of distortion into the flow in comparison with the amount of distortion applied at the inlet. In his research, he introduced and used a set of distortion descriptors based on Fourier analysis to quantitatively capture distortion magnitude, shape, and phase change across blade rows [22]. These descriptors are explained in further detail in the following section.

2.5 Describing Distortion

Methods to quantify and describe inlet distortion in turbomachinery were originally created by engine manufacturers, aircraft manufacturers, and customers. In 1978, however a set of distortion descriptors was created under the name of ARP-1420 and efforts were made to standardize this method [6, 23]. The ARP-1420 descriptors were shown to be a good, consistent index for describing inlet distortion patterns. When describing distortion transfer and generation on a blade-row to blade-row basis, however, the ARP-1420 descriptors have been found to be inadequate at describing the complex patterns that can result [22]. Peterson's motivation for introducing a new set of distortion descriptors was to provide a method whereby distortion transfer and generation could be accurately described blade-row to blade-row.

The first two distortion descriptors from Peterson's study are modal amplitude and modal phase shift [22]. A modal amplitude A_n is the coefficient of the nth term in the Fourier Series approximation of the solution at a specific radial location on a boundary. (Radial averages may also be considered.) An example of modal amplitude results from Peterson's research is included in Figure 2.8. A modal phase shift $\Delta\phi_n$ is the difference between the modal phase at one boundary $\phi_{n,1}$ and the modal phase at another boundary $\phi_{n,2}$. The Fourier series equation used is Equation 2.5.

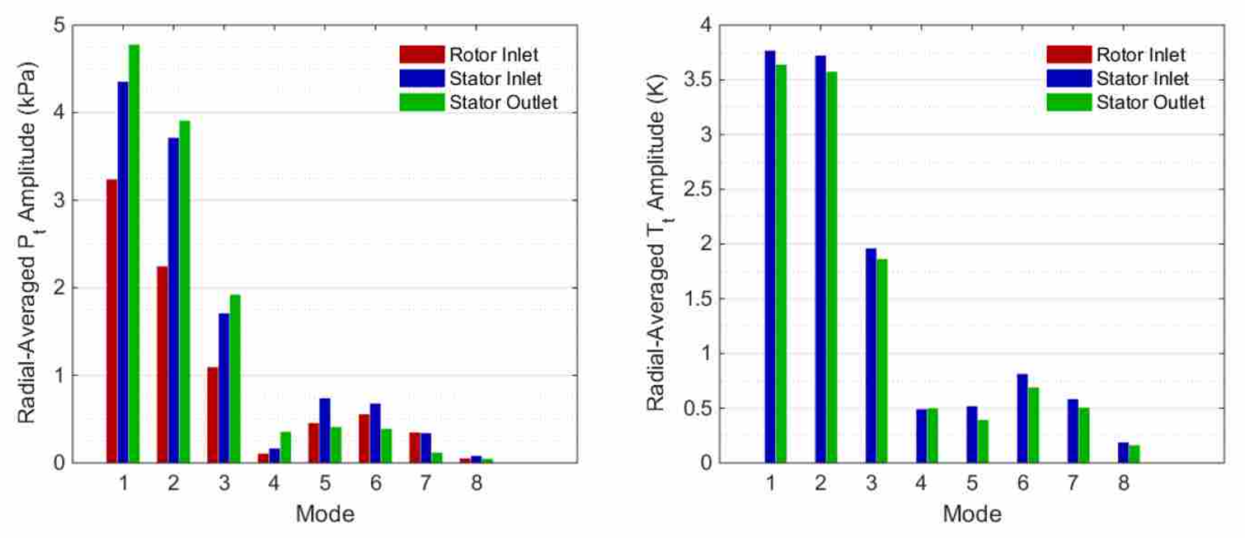

(a) Distortion transfer.

(b) Distortion generation.

Figure 2.8: Example of Fourier modal amplitude distortion descriptors from Peterson's research.

$$s_N(x) = \frac{A_0}{2} + \sum_{n=1}^{N} A_n \cdot \sin\left(\frac{2\pi nx}{p} + \phi_n\right) \tag{2.5}$$

The significance of the modal amplitude is that it gives information about the magnitude of the circumferential distortion present on a mode-to-mode basis. For example, the mode 1 amplitude quantifies the magnitude of the circumferential 1-per-rev component of distortion present in the profile. This allows for detailed analysis of the distortion.

Phase shift is a measure of the rotation of a given distortion profile around the axis of the compressor. This parameter is valuable for understanding the circumferential motion of the distortion profile as it passes through each blade row of the compressor. This is important to quantify since often there is a phase lag between the total pressure and total temperature distortion.

The third and final distortion descriptor from Peterson's study is the total amplitude. This is the sum of the coefficients of all the terms that make up the Fourier series approximation of the solution (defined in Equation 2.6). This descriptor is useful because it can give an overall value for the amount of distortion present at a location with just one number.

$$\Sigma A = \sum_{n=1}^{N} A_n \tag{2.6}$$

CHAPTER 3. METHODOLOGY

This chapter presents the methodology of this research. Section 3.1 provides details on the geometry, mesh, boundary conditions, models, and solve parameters used in the URANS study with PBS Rotor 4. Two methods for calculating local power variations are also outlined. Section 3.2 provides details on the geometry, mesh, boundary conditions, models, and solve parameters used in the Harmonic Balance study with NASA Rotor 37.

3.1 PBS Rotor 4 URANS Study

In this section, details are provided for the study involving PBS Rotor 4. The objectives of this study were to present and analyze distortion results for a distorted Full-Annulus URANS simulation at multiple radial locations and multiple operating points to offer insight into how distortion flow physics vary radially and with operating point. The properties of interest are swirl, power, total pressure, and total temperature.

3.1.1 Geometry

PBS Rotor 4 [24] (hereafter called rotor 4) was designed to be a state-of-the-art fan with high mass flow and high aerodynamic loading. It has a low hub/tip ratio, and the change in hub radius is very large between the leading and trailing edges of the rotor. At design conditions, more than half of the blade height experiences supersonic relative Mach numbers making it ideal for studies involving shock strength and interactions between shocks and blade rows. The design of rotor 4 is similar to that of many modern high-performance turbofans making it relevant for experimental and CFD research. Performance measures for rotor 4, including corrected mass flow, pressure ratio, and efficiency were quantified and discussed by Law and Puterbaugh [24].

Table 3.1: Rotor 4 design parameters.

Design Parameter	Value
Number of Blades (Rotor)	20
Number of Blades (Stator)	31
Outer Diameter (Tip)	0.4318 m
Running Tip Clearance	0.508–0.635 mm
Flow Rate	27.56 kg/s
Pressure Ratio	2.057
Rotor Efficiency	94.60%
Rotation Speed	20,200 RPM

Figure 3.1 shows the geometry of rotor 4, and Table 3.1 gives some details about its design parameters. Figure 3.2 shows the axial locations in the domain where data was evaluated for this study.

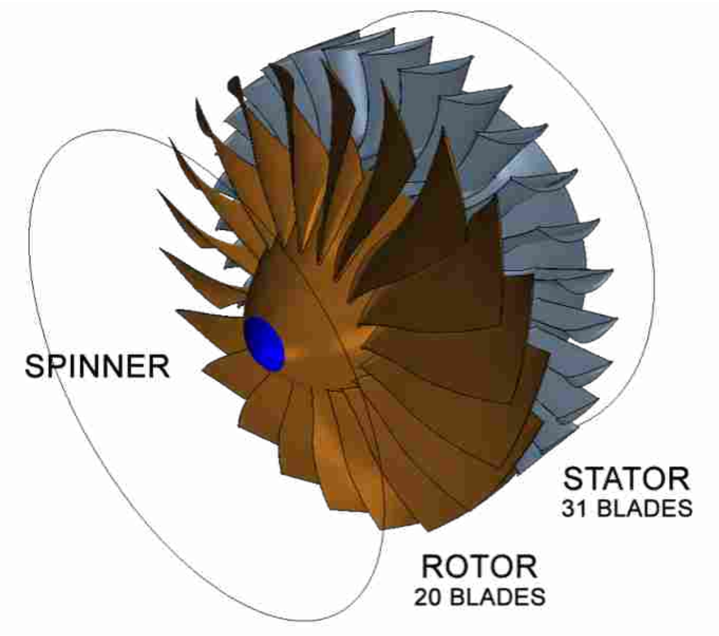

Figure 3.1: PBS Rotor 4 geometry

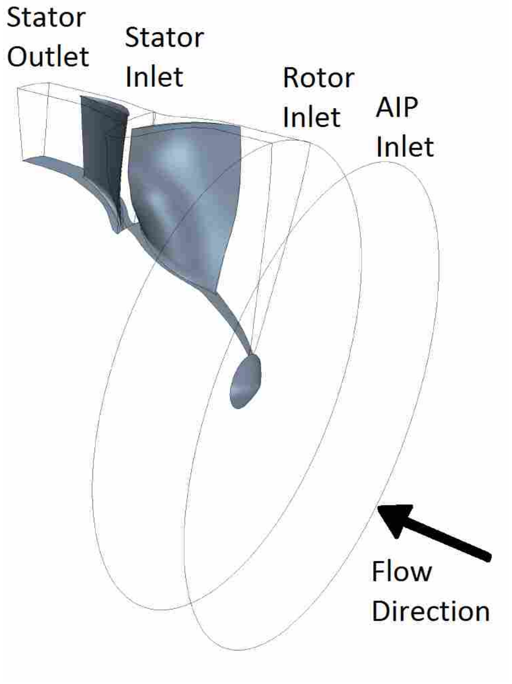

Figure 3.2: Single-passage geometry of rotor 4 showing axial locations (boundaries) where data was evaluated in this study.

3.1.2 Mesh

A mesh was generated using the built-in meshing capabilities of STAR-CCM+. The computational domain of the full-annulus simulation included three regions: spinner, rotor, and stator (see Figure 3.1). A mesh for a single passage in the computational domain without the spinner is shown in Figure 3.3. An unstructured polyhedral grid was generated away from the walls, while structured prism layers were used near the walls in order to have sufficient refinement in the boundary layer. The numbers of prism layers varies from 8 to 12 for the different wall boundaries in the domain. The mesh has an average y+ of 10. This mesh resolution was chosen to balance best practice recommendations with computational cost requirements. The cell counts in the spinner, rotor and stator regions are 14.9M, 92.3M and 185.9M respectively. The total cell count of the full-annulus computational domain is 293.1M. The stator grid is almost twice as large as the rotor grid because the stator domain extends downstream to the exit while the rotor domain only extends slightly upstream of the rotor leading edge and is preceded by the spinner mesh region.

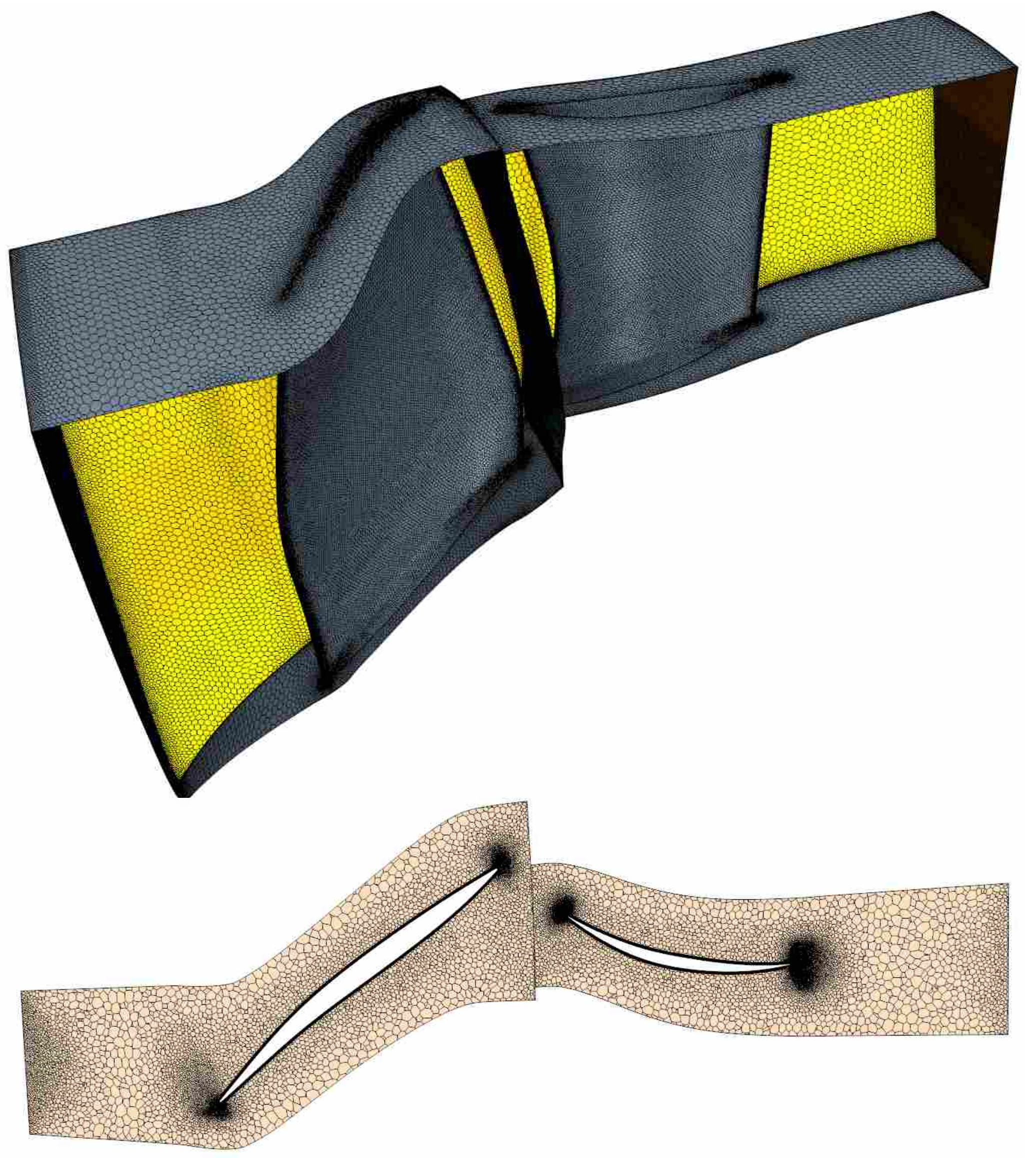

Figure 3.3: Top: Single passage of the mesh generated for rotor 4 without spinner mesh. Bottom: 2D slice of the mesh at approximately 50% span.

Previous simulations of PBS rotor 4 [22, 25] with this grid demonstrate that the grid was sufficiently refined for these types of simulations. An extensive discussion of the mesh generation process is documented in [4]; some of the significant features of the mesh are repeated in this section.

Visualizations of the leading edge of the rotor are shown in Figure 3.4. The portions near the tip gap and near the hub are shown in order to demonstrate that the curvature of the blade was sufficiently modeled in the locations where some of the most extreme pressure and velocity gradients were expected. The edges are round with no corners or jagged edges visible.

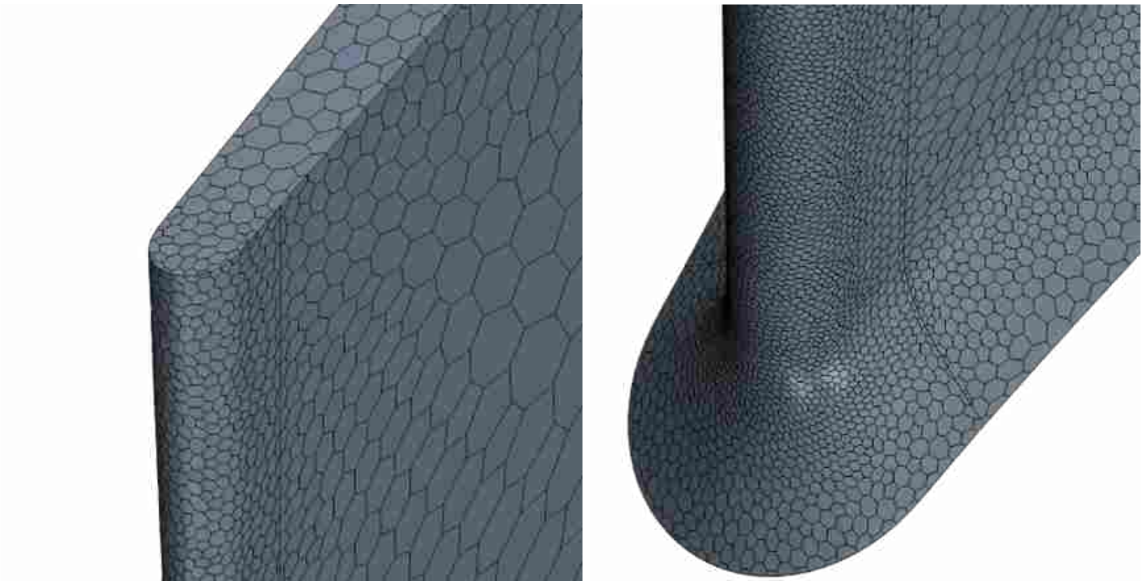

Figure 3.4: Detail views of the leading edge of the rotor mesh. Left: near the tip; Right: near the hub.

Figure 3.5 shows a detail of the mesh at the hub. As with all the other wall boundaries in the domain, prism layers were used at the hub. These structured layers are long in the streamwise direction (where velocity gradients are relatively small) and thin in the perpendicular direction (where the velocity gradients are very large). Using these prism layers allows for better refinement in the direction perpendicular to the flow in order to better capture the viscous effects of the boundary layer. The prism layers grow from the hub until they are approximately the size of the first layer of polyhedral cells. In accordance with recommendations for turbomachinery simulations, this mesh has 8 prism layers at the hub, and the growth rate does not exceed 1.3.

A cross-section of the tip gap mesh is shown in Figure 3.6. This is a critical part of the mesh because significant leakage, turbulence, and viscous shearing occur in the tip gap. The small size of the gap can cause it to be a problem area in mesh generation if cell sizes and the prism layers leading into the gap are not adjusted appropriately. Figure 3.6 shows that the prism layer

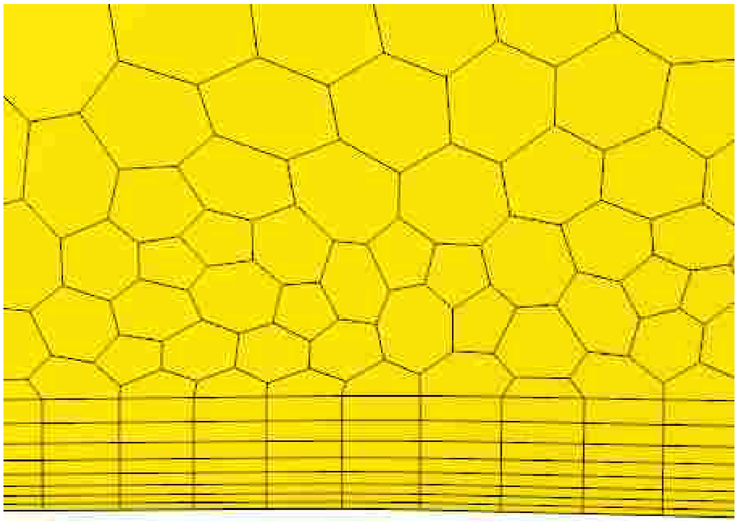

Figure 3.5: Detail of the rotor 4 mesh at the hub to show prism layer growth and first layers of polyhedral cells.

height appropriately decreases near the gap, and the polyhedral cells outside the prism layers meet the minimum recommended value of two polyhedral layers between prism layers.

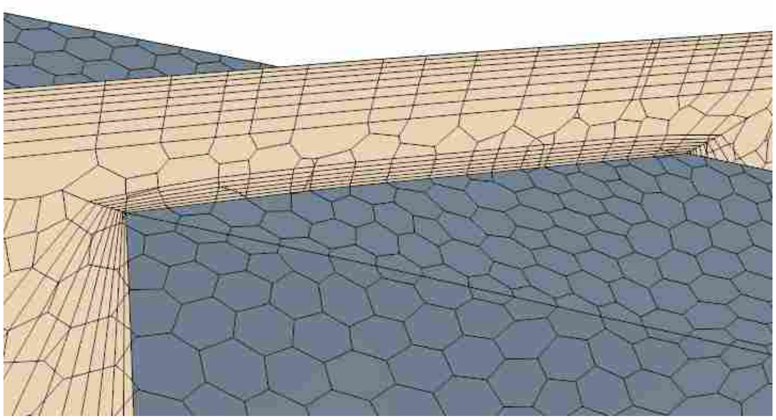

Figure 3.6: Detail of tip gap mesh for rotor 4.

For additional details on the creation of this mesh, and for best practice recommendations of turbomachinery meshing in general, the reader is referred to [4].

3.1.3 Boundary Conditions

The inlet total pressure profile used for this study was a 90° distorted sector (Figure 3.7). The profile has 15% distortion as defined in Equation 3.1 where PD is percent distortion, $P_{t,max}$ is the maximum total pressure, and $P_{t,min}$ is the minimum total pressure. A parabolic boundary layer profile and a distortion transition region were included to better match what is seen in experimental studies. The clean region transitions to the distorted region sinusoidally so that the derivative of the profile exists at all positions. The 90° sector was chosen through evaluation of canonical patterns in the literature [23] and the circumferential extent of patterns such as that shown in [12, 13]. Profile shapes similar to this 90° sector have been observed at the exit of aggressive S-duct diffusers. As the flow passes through the S-duct, counter rotating swirl regions, known as twin swirl, form along the symmetric axis of the diffuser. The twin swirl generates counter rotating vortices (vortex swirl) that form at top dead center (TDC). This swirl causes a velocity driven 90° low total pressure distortion region to form at TDC. Further details are provided in [22].

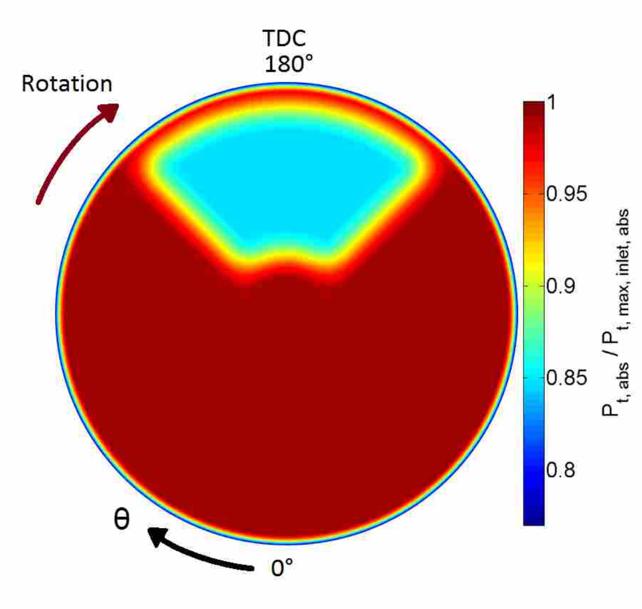

Figure 3.7: 15% total pressure inlet distortion profile applied at aerodynamic interface plane (AIP). Values are shown as % of peak at inlet.

$$PD = \frac{P_{t,max} - P_{t,min}}{P_{t,max}} \cdot 100\% \tag{3.1}$$

A constant inlet total temperature was specified and no swirl was explicitly set at the inlet boundary. The location of the inlet plane (also known as aerodynamic interface plane or AIP) was 1.3 rotor tip chords upstream of the rotor leading edge. This location was selected based on future availability of experimental data (total pressure and flow angles) at the axial location. At the time of the simulations no experimental data was available.

Static pressure exit boundary conditions were chosen that resulted in three separate operating points: near-stall, design, and choke. The exit boundary condition was applied at approximately 0.85 stator chord downstream of the stator trailing edge. The exit boundary location was selected based on the location of facility adaptive hardware in the experimental setup. While the interaction of the boundary condition does negatively influence the back pressuring of the stator row, the simulation provides a meaningful demonstration of total temperature distortion generation in the rotor. For simplicity the facility adaptive hardware and other downstream components were not incorporated in the simulation.

3.1.4 Models and Solve Parameters

The unsteady simulations for the rotor 4 study were begun from a converged steady-state simulation file for which a uniform total pressure field had been applied at the the inlet boundary (clean inlet). This is recommended practice for unsteady simulations such as those involving inlet distortion because it increases the stability of the solver and expedites convergence. The coupled implicit unsteady solver in STAR-CCM+ was selected to conduct the full-annulus URANS simulations of rotor 4 with the applied distortion pattern. Initially, a coarse time step that resulted in 2 degrees rotor rotation was used with 40 inner iterations at each time step to resolve the larger flow features. Then, to resolve the finer features and achieve convergence, a time step was chosen that resulted in 1/4 degree rotor rotation. With the finer time steps, 10 inner iterations were run (72 time steps per rotor pitch, 1440 time steps per rotor rotation). The Spalart-Allmaras turbulence model was used. The STAR-CCM+ documentation recommends SST K-omega as the best turbulence model for unsteady simulations of axial fans in general; however, Spalart-Allmaras is the standard turbulence model for Harmonic Balance simulations in STAR-CCM+, and it was used by Marshall Peterson for both his HB and URANS simulations [4]. For the sake of consistency the Spalart-Allmaras model was used for all simulations in this thesis. Future simulations may result in slightly greater accuracy by using the SST K-omega model.

3.1.5 Simplified Phase Shift

For the URANS study with rotor 4, a new, simplified phase shift is introduced. In contrast with the phase shifts found by Marshall Peterson [22] that were discussed in section 2.5, these simplified phase shifts are found in the manner illustrated in Figure 3.8. In this example, a traverse of total pressure is used. The phase shift is the difference between the centers of the distorted regions at two axial locations. At the rotor inlet, the center of the distorted region is at TDC or 180 degrees. After passing through the rotor, however, the distortion pattern changes, and so the center of the distorted region is found by calculating the average of the locations of the minimum and maximum values of total pressure. Defining the center of the distorted region in this manner relies on the assumption that the pattern has a distinct minimum near the location of the leading edge of the applied sector and a distinct maximum near the location of the trailing edge of the applied sector. If the distortion shape differs significantly from this expected pattern, then the phase shift calculated by this simplified method becomes less representative of the true flow field. For this thesis, when multiple local maximums or minimums exist, the extrema closest to the leading and trailing edges of the distorted sector are used in the calculations.

One of the main differences between these simplified phase shifts and Peterson's is that the simplified phase shifts describe the shift with just one number at each location, whereas Peterson's include a separate phase shift for each mode that is calculated in the Fourier reconstruction. This makes the simplified phase shifts more physically intuitive for direct comparison to what is seen in contour plots.

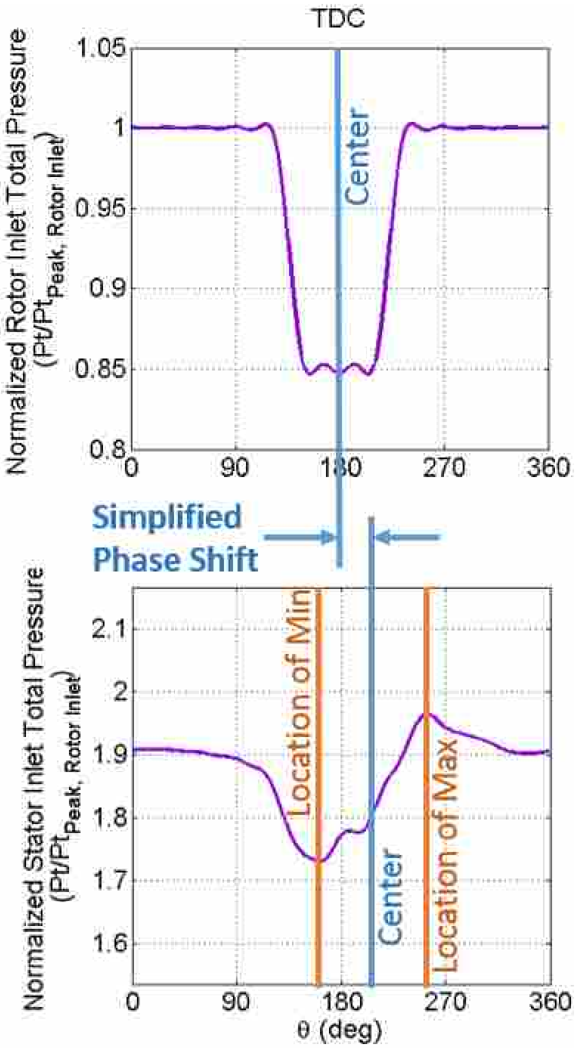

Figure 3.8: Visualization of the Simplified Phase Shift introduced in this thesis.

3.1.6 Swirl Calculations

Swirl is a measure of flow angularity and is defined as the angle between the velocity vector at a given point and the axial direction. Flow may have both circumferential and radial components of velocity, however, swirl generally refers to the circumferential (tangential) flow angularity only. This is calculated by equation 3.2 where V_{tang} is the tangential component of velocity, and V_{axial} is the axial component of velocity. See Figure 2.3 for a graphic that shows how circumferential swirl is calculated.

$$Circumferential Swirl Angle = \arctan\left[\frac{V_{tang}}{V_{axial}}\right] \tag{3.2}$$

3.1.7 Streamtube Method for Power Analysis

One goal of this study is to analyze radial and circumferential variations in work performed by a fan or compressor because non-uniform work is the driving mechanism behind total temperature distortion generation. In this thesis, discussions of work will be based on power calculations. Work variations are directly related to power variations because power is defined as work per time. One method for determining the amount of power at a location within a fan or compressor is to calculate the total temperature change and the mass flow rate along a streamline. To calculate the average power for a given portion of the fan, a control volume can be defined that encompasses and follows many streamlines. This volume of streamlines is known as a streamtube. The amount of power performed in a streamtube can be calculated by using equation 3.3. For compressible turbomachinery flow, this equation is valid and commonly used to predict power.

$$\dot{W} = \dot{m} \cdot c_p \cdot (T_{t2} - T_{t1}). \tag{3.3}$$

In equation 3.3, $\dot{W}$ is power, $\dot{m}$ is the mass flow rate, c_p is the specific heat, T_{t1} is the total temperature at the inlet of the streamtube, and T_{t2} is the total temperature at the exit of the streamtube. These total temperatures were mass-flow-averaged in order to account for variations in density within the streamtube.

To achieve accurate results with equation 3.3, the streamtubes should follow the actual streamlines of the flow as closely as possible. Adamczyk and Fidalgo described and used a method that accurately predicted the exact time-averaged streamtubes through a blade row [15, 26]. Although their method provides extremely accurate streamtubes, it is a very complicated process that is not suitable for quick analyses. One of the goals of the present thesis was to introduce a simplified streamtube method to qualitatively analyze radial and circumferential variations in power. It was therefore assumed that useful results could be achieved even if all streamtubes were approximated as having the same circumferential shift. That shift was estimated based on the circumferential locations of the center of the region of distorted total pressure before and after the rotor. This simplified analysis determined that the shift ranged from 2 degrees to 28 degrees at the five radial locations, but the average shift was 17 degrees, and so a constant shift of 17 degrees in the clockwise direction was applied for all streamtubes. A more accurate streamtube analysis might be conducted by varying the amount of shift with span and circumferential location, but this would significantly increase the complexity of the method, thus defeating its purpose of simplifying power calculations.

Twenty circumferential locations and five radial locations were examined with the streamtube method. The number of circumferential locations was chosen based on the number of rotor blades. The radial locations were defined by breaking the annulus into five annuli between the hub and the tip. This was done at the rotor inlet and at the rotor outlet (stator inlet).

Two approaches were used to define the locations of the five annuli. In the first approach, the annuli were defined to be evenly spaced so that the average radii in the areas were at 10%, 30%, 50%, 70%, and 90% spans (see Figure 3.9). In the second approach, the annuli were defined such that areas of each of the annuli were equal (See Figure 3.10). It was expected that the equal-area approach would better capture the paths of the streamlines. Figure 3.9 and Figure 3.10 also show the 17-degree clockwise shift across the rotor.

3.1.8 Blade Loading Method for Power Analysis

In addition to the streamtube analysis, a blade loading analysis was also performed to determine the radial and circumferential variations in power. This second method to measure power was of interest in addition to the streamtube method because the two methods rely on different assumptions and carry different limitations and advantages. They are therefore expected to capture different results, but the results of both methods are expected to have similar trends. Both methods are instructive in helping understand the actual variations in work.

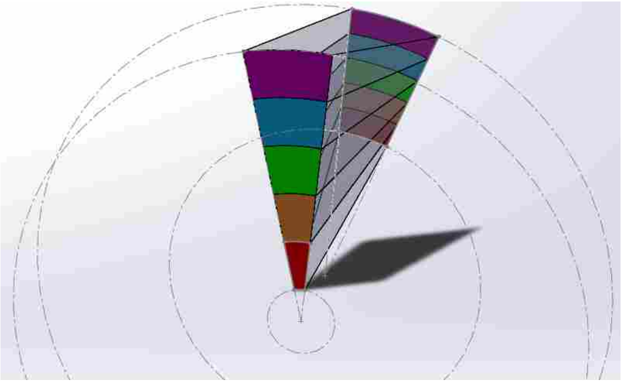

Figure 3.9: Visualization of the areas involved in the streamtube method using evenly-spaced radii. Note that the average radii within the five areas occur at 10%, 30%, 50%, 70%, and 90% span.

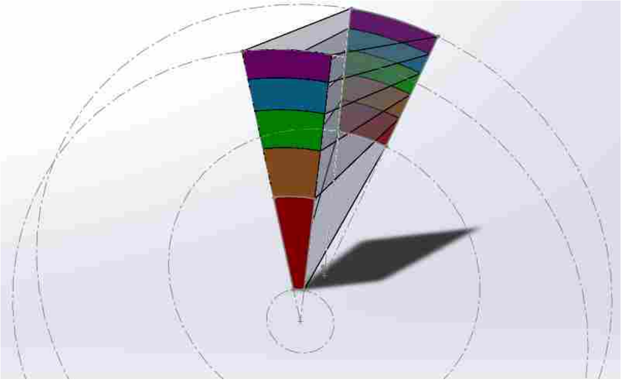

Figure 3.10: Visualization of the areas involved in the streamtube method using equal areas. The area of the red annular sector is equal to the area of the orange annular sector, which is equal to the area of the green annular sector, and so on.

The blade loading analysis was performed by extracting static pressure data at an instant in time on each blade at 10%, 30%, 50%, 70%, and 90% span. An example of the static pressure blade loading at a cross-section of a blade is shown in Figure 3.11. The static pressures on the suction side and the pressure side were then integrated from leading edge to trailing edge to determine the power performed at each of the five radial locations on each blade. Equations 3.4 and 3.5 were used for this integration:

$$\dot{W}_{pressure} = \int P_{pressure} \cdot U(r) \cdot dA \tag{3.4}$$

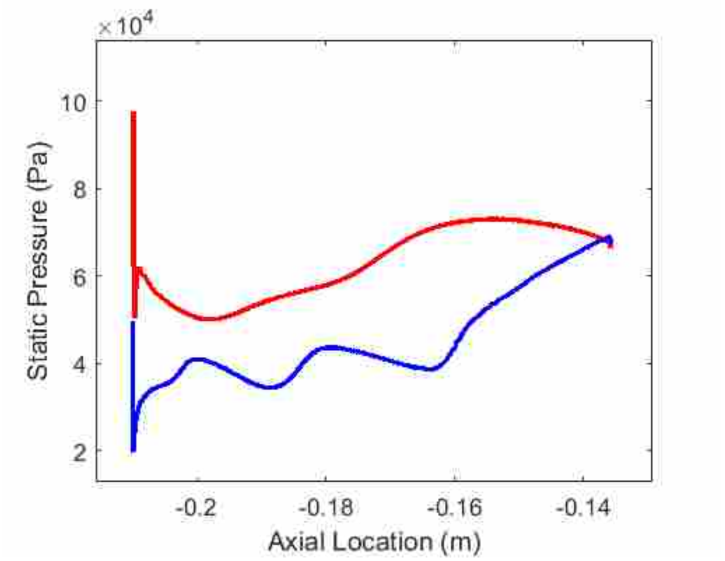

Figure 3.11: Example of a static profile at a cross-section of a fan blade. The red curve is the pressure surface, and the blue curve is the suction surface.

$$\dot{W}_{suction} = \int P_{suction} \cdot U(r) \cdot dA. \tag{3.5}$$

In equations 3.4 and 3.5, $P_{pressure}$ is the static pressure on the pressure surface, and $P_{suction}$ is the static pressure on the suction surface of the blade. $U(r)$ is the blade speed as calculated by $U(r) = N_1 \cdot r$ where N_1 is the rotational speed in radians per second, and r is the radial location on the blade. The last terms in the integrals are defined by $dA = h \cdot dz$, where dz is a differential length element in the axial direction, and h is the approximate height of the differential region for which power is being calculated. This height term for each area was calculated as 1/5 the distance from hub to tip because five uniformly-spaced spans were used. These terms are portrayed in Figure 3.12.

Once the integrals were taken, the net power at each radial location on each blade was calculated with equation 3.6:

$$\dot{W} = \dot{W}_{pressure} - \dot{W}_{suction}. \tag{3.6}$$

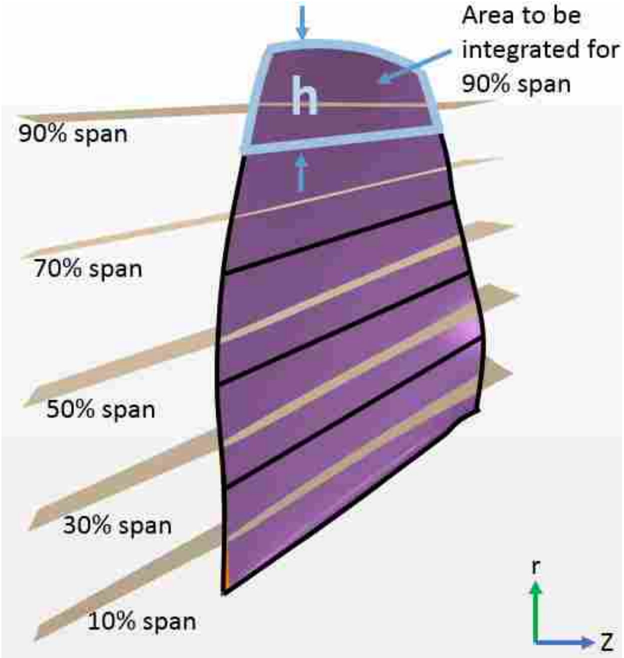

Figure 3.12: Visualization of the terms and areas involved in the blade loading integration.

3.1.9 Averaging Results

In order for the data from the rotor 4 simulations to be analyzed, two types of averaging were necessary. All of the results were time-averaged (except where noted in the following chapter) in order to get the average effect of the rotating blades over time. Additionally, overall performance measure reports (efficiency and pressure ratio) were also mass-flow-averaged in order to account for the compressibility of the flow. A mass flow average is calculated with equation 3.7.

$$MassFlowAverage = \frac{\sum_f \rho_f \phi_f \left| v_f \cdot a_f \right|}{\sum_f \rho_f \left| v_f \cdot a_f \right|} \tag{3.7}$$

In equation 3.7, ϕ_f is the face value of the selected scalar (efficiency or pressure ratio), ρ_f is the face density, v_f is the face velocity vector, and a_f is the face area vector. Appropriate monitor reports were generated in STAR-CCM+ so that these calculations could be handled internally by STAR-CCM+.

3.2 NASA Rotor 37 Harmonic Balance Study

In this section, details are provided for the study involving NASA Rotor 37. The objectives of this study were to perform Harmonic Balance and Full-annulus URANS simulations with varying inlet distortion profiles, analyze trends in distortion and performance measures, and compare the findings to the conclusions of Peterson's rotor 4 Harmonic Balance study [4]. The specified Harmonic Balance mode combinations will be compared in their abilities to match the URANS results.

3.2.1 Geometry

The configuration chosen for the Harmonic Balance study was a single-stage compressor that consists of an inlet guide vane (IGV) followed by a rotor. The IGV blade geometry is an airfoil generated by CD-adapco for testing and tutorial purposes. [27] This IGV has 48 blades. The geometry of the rotor row is that of the NASA Stage 37 axial compressor. [28, 29] It has 36 blades rotating at design speed of 17,200 rpm. Design parameters for rotor 37 are presented in Table 3.2. The geometry is shown in Figure 3.13 and Figure 3.14. Figure 3.15 shows the axial locations in the domain where data was evaluated for this study.

NASA Rotor 37 (hereafter called rotor 37) is a transonic compressor that was designed to be a simple test geometry for three-dimensional turbomachinery flow solvers. At its design conditions, it has strong shock wave-boundary layer interactions, and significant viscous effects. [30] Because these interactions and viscous effects can be very difficult to resolve, they make the rotor an ideal case for testing a solver's accuracy.

3.2.2 Mesh

The mesh for this study is an HOH type generated by the elliptical gridder in STAR-CCM+. The elliptical gridder generates a structured mesh by creating nested loops around the blade profile, and by creating layers of cells from the hub to the tip. It ensures that cells close to walls have greater refinement to better capture the flow in the boundary layer.

Table 3.2: Rotor 37 design parameters.

Design Parameter	Value
Number of Blades (Rotor)	36
Outer Diameter (Tip)	0.5074 m
Design Tip Clearance	0.356 mm
Flow Rate	20.19 kg/s
Pressure Ratio	2.106
Rotor Efficiency	87.7%
Rotation Speed	17,188.7 RPM

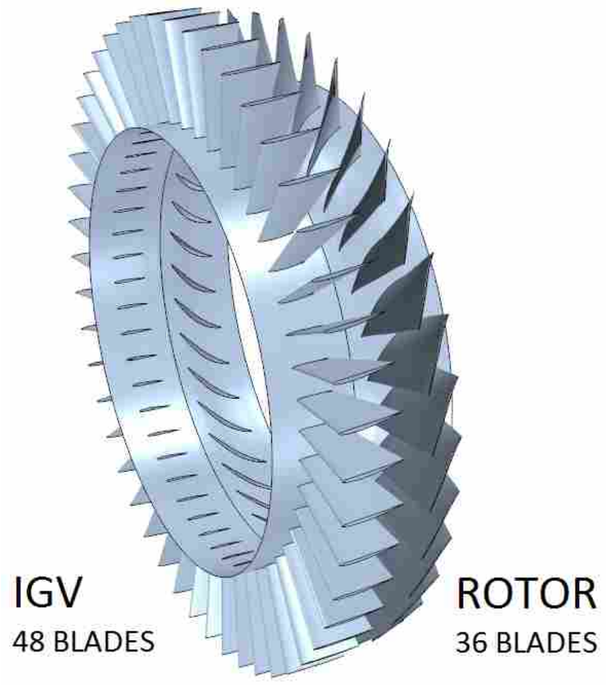

Figure 3.13: NASA rotor 37 full-annulus geometry.

An initial grid was provided by a technical specialist from CD-adapco. The initial grid was refined until grid convergence was ascertained. The resulting mesh is shown in Figure 3.16. A single passage of this mesh contains approximately 680,000 cells, and so the full-annulus mesh contains approximately 28 million cells. The convergence study (see Figure 3.17) showed that efficiency results with this mesh are accurate to approximately ±0.0013 and total pressure ratio results are accurate to approximately ±0.0025. That amount of accuracy was deemed sufficient for this thesis.

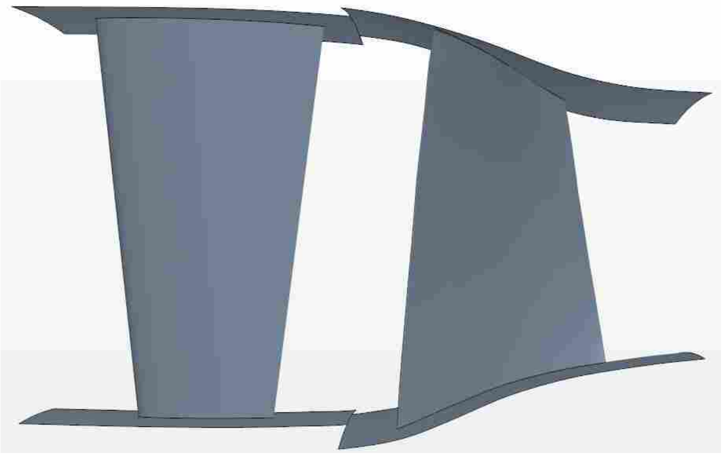

Figure 3.14: Single-passage geometry: IGV (left) and NASA rotor 37 (right).

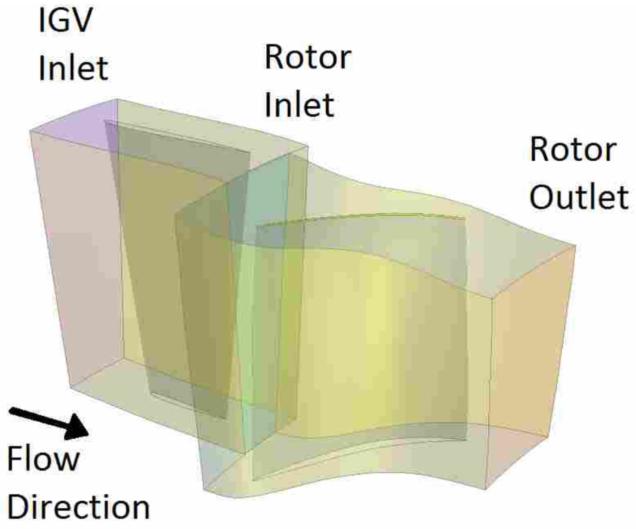

Figure 3.15: Single-passage geometry of rotor 37 showing axial locations (boundaries) where data was evaluated in this study.

3.2.3 Boundary Conditions

The inlet profiles used in this study are distributions of total pressure with either one or two low-pressure regions. These are commonly referred to as 1-per-rev and 2-per-rev distortion profiles, respectively. The maximum total pressure is fixed at standard atmospheric pressure (101,325 Pa), and the minimum total pressure varies according to the percent distortion (PD) as defined previously in Eq. 3.1. Percent distortions of 10%, 15%, and 20% are used in this study. Boundary

Figure 3.16: Top view of mesh for IGV (left) and NASA rotor 37 (right).

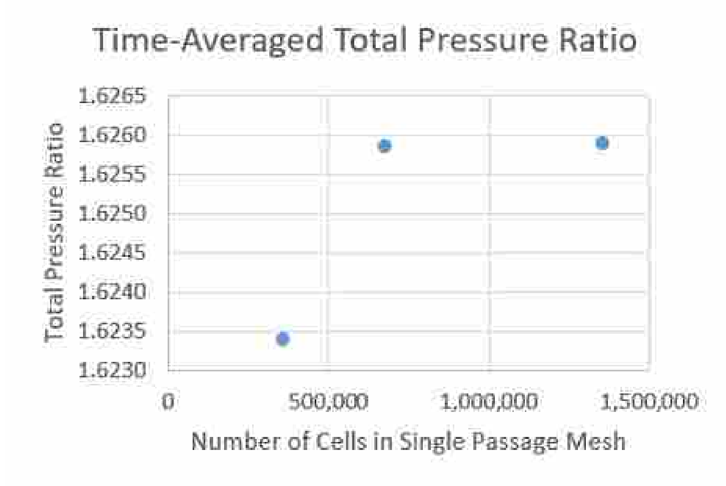

Figure 3.17: Grid convergence study for rotor 37.

layers of equal thickness and magnitude were generated at the hub and tip for each of the inlet profiles.

Sinusoidal distributions were chosen as the inlet profile shape in this study because they are a standard profile used to evaluate fan and compressor response to inlet distortion. Figure 3.18 shows the circumferential variations of the applied total pressure fields at the inlet boundary for the 15% distortion simulations.

The outlet boundary condition was set to be a pressure outlet with a constant static pressure that resulted in a near-design operating point.

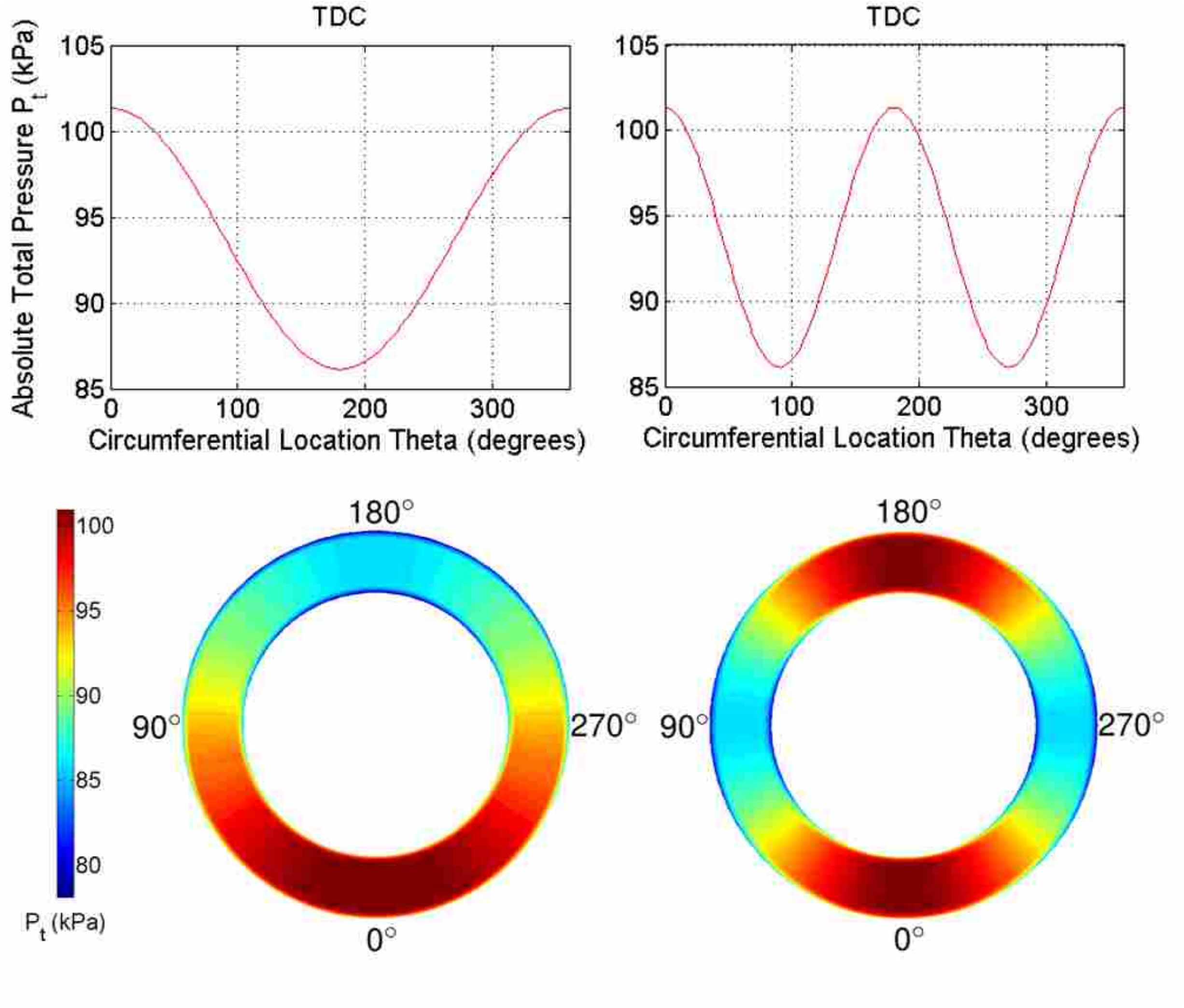

Figure 3.18: Plots of 15% 1-per-rev (left) and 2-per-rev (right) inlet distortion profiles. The top row shows total pressure at 50% span. The bottom row shows total pressure at all locations of inlet boundary. Top dead center (TDC) is at 180°. A clockwise rotation in the plots on the bottom corresponds to a shift in the righthand direction for the plots on the top.

3.2.4 Models and Solve Parameters: URANS Simulations

The unsteady simulations for the rotor 37 study were begun from a converged steady-state simulation file that had used a uniform total pressure field at the the inlet boundary (clean inlet).

The coupled implicit unsteady solver in STAR-CCM+ was selected to conduct the full-annulus URANS simulations of rotor 37 with the applied distortion patterns. Initially, a coarse time step that resulted in 2 degrees rotor rotation was used with 40 inner iterations at each time step to resolve the larger flow features. Two full revolutions were simulated with this coarse time-step. Then, to resolve the finer features and achieve convergence, a time step was chosen that resulted in 1/4 degree rotor rotation. With the finer time steps, 10 inner iterations were run (72 time steps per rotor pitch, 1440 time steps per rotor rotation). Four additional revolutions were simulated with this fine time-step. The Spalart-Allmaras turbulence model was used.

3.2.5 Models and Solve Parameters: Harmonic Balance Simulations

The Harmonic Balance simulations were also begun from a converged steady-state simulation file in order to expedite overall convergence. The Harmonic Balance flow and energy model in STAR-CCM+ was selected to conduct these simulations. The HB Standard Spalart-Allmaras turbulence model was used. Approximately 10,000 iterations were required for each Harmonic Balance simulation.

When using the Harmonic Balance solver in STAR-CCM+, the recommended way to specify a distortion profile at a boundary is to use the wake specification method with a stagnation inlet boundary type. Of the several options for wake specification, the option chosen for this study was Spatial Annular Data, which required that static pressure, static temperature, and velocity data be defined at radial and tangential locations throughout the boundary.

A script was written to generate tables with the required static temperatures and velocities that corresponded to the desired total pressure profile for a specified constant static pressure. For each inlet profile, a static pressure was chosen that corresponded to a spatial average inlet Mach number of approximately 0.58. These tables with the necessary static pressure, static temperatures, and velocities were set as the inlet condition for the harmonic balance simulations.

3.2.6 Mode Combinations Simulated

The primary mode combinations of interest for this study are defined in table 3.3. (Refer back to Figure 1.2 as well as [4] for an explanation of mode combinations.) The number of modes at the inlet boundary varies from one to five in order to reveal the effect of increasing the amount of distortion content captured at the inlet. The numbers of modes in the blade rows are either zero in each blade row or one in each blade row in order to see the significance of the 1-per-rev components of distortion introduced by the blade rows. Simulations were also run with multiple modes in each blade row to see if that significantly impacted results. For a complete listing of the combinations simulated including whether each simulation converged or diverged, see appendix B.

Recall that the rotor 37 configuration in this study is an IGV followed by a rotor, and so the second number in the combination refers to the IGV blade row, and the third number refers to the rotor blade row. Peterson's study involving rotor 4 [4] consisted of a rotor followed by a stator, and so in his study the second number in the combination referred to the rotor blade row, and the third number referred to the stator blade row.

Table 3.3: Primary mode combinations
to be compared.

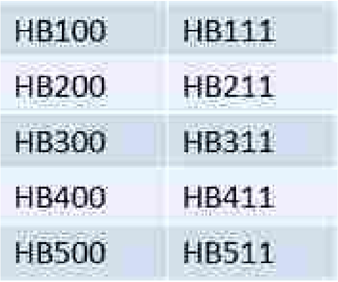

HB100	HB111
HB200	HB211
HB300	HB311
HB400	HB411
HB500	HB511

3.2.7 Averaging Results

In order for the results of the rotor 37 simulations to be analyzed, three types of averaging were necessary. First, all of the results were time-averaged (except where noted) in order to get the average effect of the rotating blades over time. The overall performance measure reports were also mass-flow-averaged (see equation 3.7) in order to account for the compressibility of the flow. Finally, the data at each of the inlet and outlet boundaries was radially-averaged. This was necessary because the distortion descriptors for the HB data did not show discernible trends at individual radial locations, but radial averaging gave HB results that better matched the URANS results and could be reasonably compared for each simulation.

CHAPTER 4. RESULTS OF URANS STUDY WITH PBS ROTOR 4

In this chapter, results are provided for the study involving PBS Rotor 4. The objectives of this study were to present and analyze distortion results for a distorted Full-Annulus URANS simulation at multiple radial locations and multiple operating points to offer insight into how distortion flow physics vary radially and with operating point. The properties of interest are swirl, power, total pressure, and total temperature.

4.1 Overall Performance Measures

Some overall performance measures (fan/compressor maps) of rotor 4 subject to the applied inlet distortion profile are presented in Figures 4.1 and 4.2. Figure 4.1 shows the total pressure ratio versus corrected mass flow rate, and Figure 4.2 shows the efficiency versus corrected mass flow rate. In both plots, the distorted simulation results are depicted with blue circles. To give a reference curve, experimental data from clean (undistorted) inlet testing is shown with orange triangles. Caution must be taken when making comparisons because it is unclear how much of the discrepancy is due to the distortion, and how much is due to the fact that one set of data is from experimental testing and the other is from computer simulations.

Total pressure ratio was calculated between the rotor inlet (RI) and the stator outlet (SO) using Eq. 4.1:

$$PR = P_{t,SO}/P_{t,RI}. \tag{4.1}$$

Adiabatic efficiency for the fan was calculated using Eq. 4.2:

$$\eta_f = \frac{\frac{p_{t,SO}}{p_{t,RI}}^{\frac{\gamma-1}{\gamma}} - 1}{\frac{T_{t,SO}}{T_{t,RI}} - 1} \tag{4.2}$$

with γ calculated at the average temperature across the rotor. $P_{t,RI}$, $P_{t,SO}$, $T_{t,RI}$, and $T_{t,SO}$ were calculated as mass flow averages at the given stations and operating points.

Simulation results of total pressure ratio are shown in Figure 4.1 for five mass flow rates. As expected for a fan, lowering the back pressure caused the flow rate to reach a maximum value. This maximum mass flow rate (choked flow) is approximately 28.1 kg/s. Lowering the back pressure even more caused a significant drop in total pressure ratio while the mass flow rate remained the same. The simulation that resulted in the lowest total pressure ratio (approximately 1.72) was termed the “choke” operating point for this study. In contrast, higher back pressures resulted in lower mass flow rates and higher pressure ratios. The lowest mass flow rate that achieved convergence was approximately 27 kg/s. This was termed the “near-stall” operating point for this study. It is difficult to know exactly how close this point truly is to stall because a simulation of a fan will often reach numerical stall before an experimental fan would actually stall. Refer to section 2.2 for discussion on various operating points for a fan.

Efficiency values for the same five mass flow rates are plotted in Figure 4.2. The efficiency has a maximum value at a mass flow rate of approximately 28.05 kg/s. In general turbomachinery practice, the design operating point is usually at a slightly higher mass flow rate than the point of peak efficiency, however, due to the fact that these simulations have a distorted inlet, it is difficult to know exactly what operating point corresponds to the “design” operating point for a clean inlet. For this reason, the peak efficiency point was termed the “design” operating point for this study. As the mass flow rate is increased from 28.05 kg/s (approaching choke), the efficiency drops. As the mass flow rate decreases from 28.05 kg/s (approaching stall), the efficiency also drops.

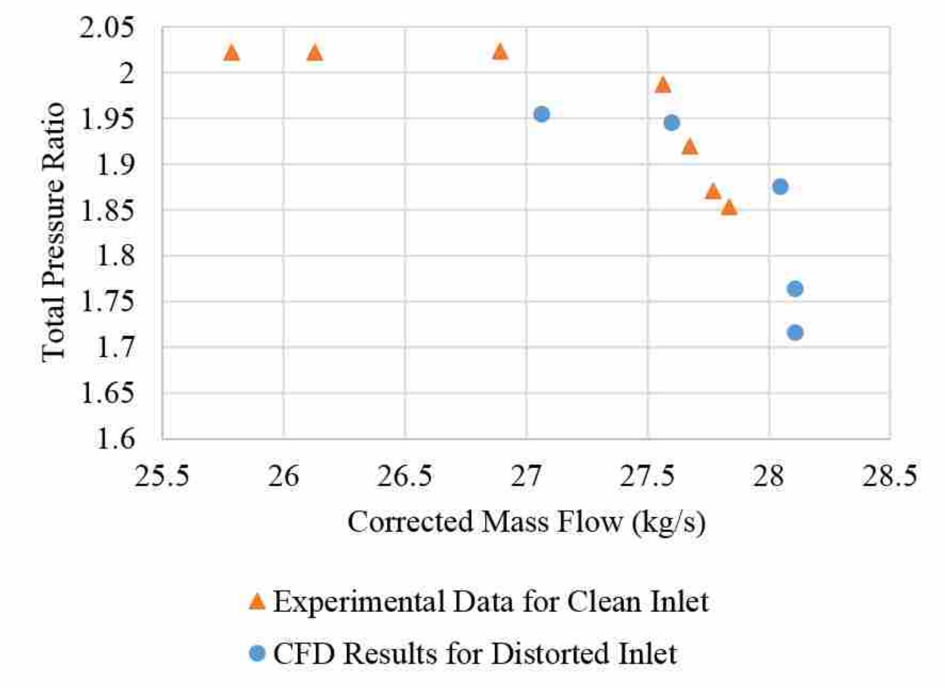

Figure 4.1: Pressure ratio plot at various operating points.

4.2 Total Pressure and Total Temperature Contours

A comparison of total pressure and total temperature contour plots for the near-stall, design, and choke operating points is provided in this section to enable qualitative analysis of distortion transfer and generation. Each of the contour plots in this section are presented as a ratio of the time-averaged value divided by the maximum value at the rotor inlet. Therefore, total pressure is normalized by 71,596 Pa, and total temperature is normalized by 288.13 K. Note that from the view in these plots, the rotor was rotating in the clockwise direction.

The total pressure and total temperature contours at the rotor inlet for the three operating points were nearly identical to the applied boundary conditions at the AIP. (Details of the applied distortion profile at the AIP are given in section 3.1.3.) These contours are shown in Figure 4.3. The distorted sector can be seen in the total pressure plot, and the constant total temperature field can be seen in the total temperature plot.

Figure 4.4 shows the total pressure and total temperature contours for each operating point at the stator inlet. At the stator inlet, effects from the rotor blade row can be seen, and some

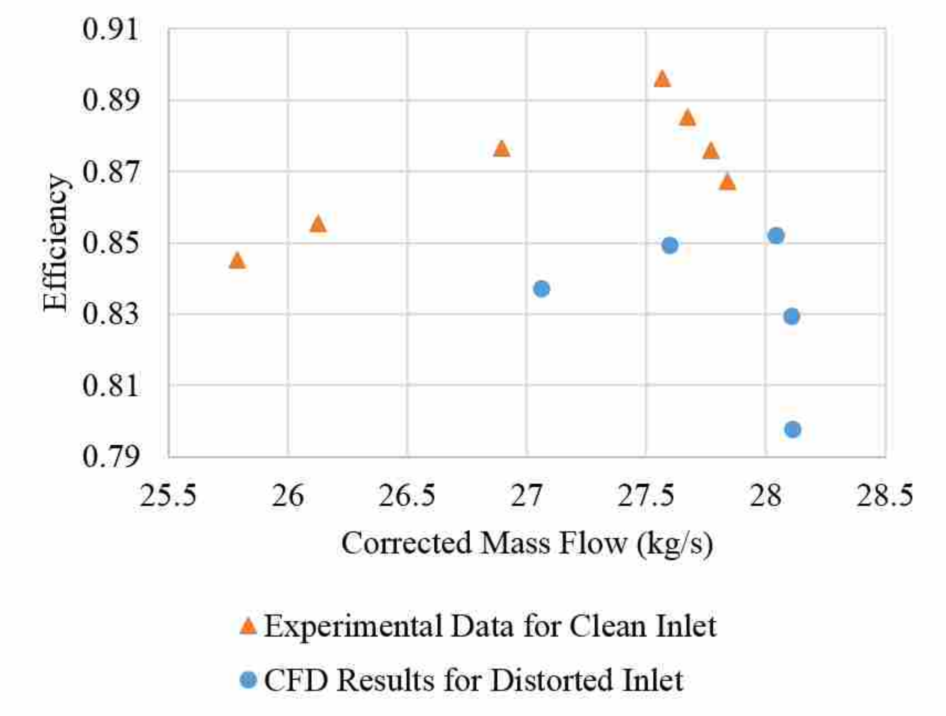

Figure 4.2: Efficiency plot for distorted inlet and experimental clean inlet.

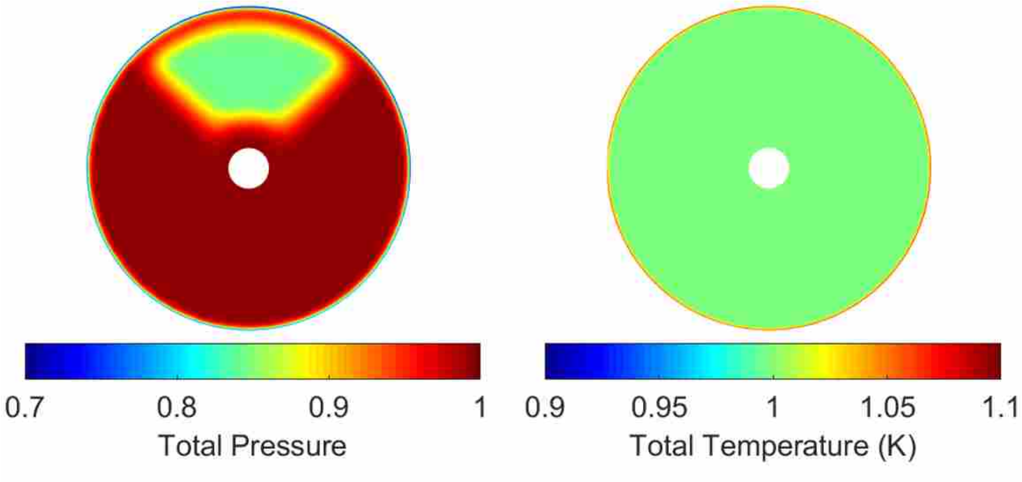

Figure 4.3: Left: total pressure at the rotor inlet. Right: total temperature at the rotor inlet.

of these effects vary based on operating point. For all three operating points, the sharp edges of the sector have been lost, and a low-pressure region and a high pressure region have formed near the hub. The new low-pressure region is located around 170 degrees (the approximate location of the leading edge of the distorted sector), and the high-pressure region is located around 225 degrees (the approximate location of the trailing edge of the distorted sector). Low and high total temperature regions have formed in the same locations for all three operating points. These correlate with locations of pressure-induced swirl as will be discussed in the next section.

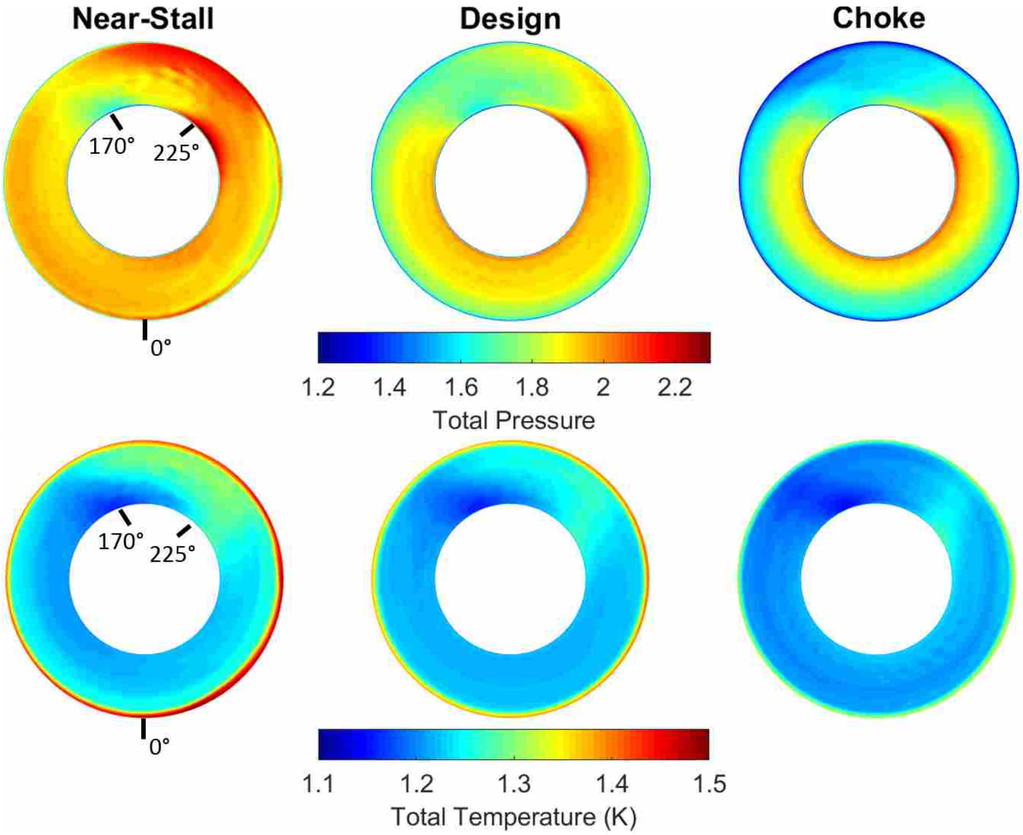

Figure 4.4: Top: total pressure at the stator inlet. Bottom: total temperature at the stator inlet.

At choke there is a low total pressure region above 70% span. At design this low total pressure is visible above 85% span and at the near-stall operating condition the low total pressure region is not present. At choke a low total pressure sector is seen at the top and closely mirrors the inlet distortion profile. At design the low total pressure sector is still visible but smaller in magnitude and circumferential extent. Near-stall, the sector is confined to the lower 40% span and only extends circumferentially 20 degrees. For the near-stall case, a significant high pressure region forms at the casing, spanning from 180 to 225 degrees. The general distribution of the distorted region is similar from choke to stall but the magnitude of total pressure increases. This is a result of the rotor pressure ratio increasing as shown in Fig. 4.1. The rotor pressure ratio increases from 1.72 to 1.88 from choke to design to 1.95 near stall.

The total temperature distortion generated in response to the total pressure distortion is shown in the bottom of Figure 4.4. A high Tt distortion region is generated at approximately 225 degrees, and a low Tt region is generated at approximately 170 degrees. The magnitude of total temperature distortion increases from choke to design to the near-stall operating condition. An annular ring of higher temperature flow was also shown for the near-stall condition near the fan blade tips. This increase of total temperature is likely due to the rotor tip gap. This flow, along with the viscous shearing against the shroud causes viscous heating, increasing the total temperature. The affected area is about 10 times thicker than the running tip clearance.

4.3 Pressure-induced Swirl

Research has shown that inlet total pressure distortion can induce swirl, which influences the power generated by a rotor blade as it rotates around the fan [1, 14, 15, 31]. One objective of this thesis is to understand how operating condition and distortion change the rotor power around the fan circumference.

As described in section 3.1.6, swirl is a measure of flow angularity and is defined as the angle between the velocity vector at a given point and the axial direction. The distribution of swirl distortion at the rotor inlet for all three operating points is provided in Figure 4.5. Recall that no swirl was applied at the inlet plane, and so the swirl shown in these plots is a response to the total pressure distortion applied at the inlet plane. This is known as pressure-induced swirl, and has been the subject of various investigations [1, 14, 15, 31]. The swirl is greatest at the locations of the edges of the applied inlet distortion. This is because the distorted total pressure field at the inlet creates a static pressure gradient, which in turn creates a force imbalance that needs to be resolved. Over the length of the inlet duct from the AIP to the rotor inlet, this force imbalance causes a mass redistribution in the circumferential direction. Tangential components of velocity are induced causing swirl in the direction from high to low pressure on either side of the distorted sector. At the location where a blade enters the distorted sector the swirl is in the same direction as the blade rotation (co-swirl). At the location where a blade exits the distorted sector the swirl is opposite the blade rotation (counter-swirl).

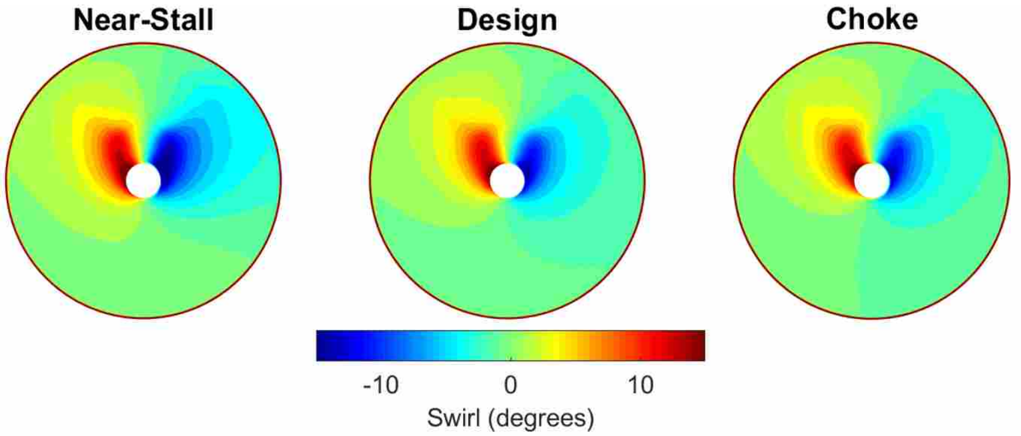

Figure 4.5: Swirl (degrees) at rotor inlet (approximately 0.45 rotor tip chords or 45mm upstream from rotor leading edge).

As Fidalgo et al. noted [15], another effect of the distorted pressure field at the inlet is that the stagnation point on the spinner becomes slightly offset from the point of the nose cone. It is offset in the direction opposite the distorted sector. This induces radial mass redistribution near the hub into the distorted region. The swirl plots in Figure 4.5 reveal that the maximum magnitudes of co- and counter-swirl occur near the hub suggesting that redistribution of flow across the spinner increases the effects of the pressure-induced co- and counter-swirl near the hub. Fidalgo and Weston also found swirl to have the greatest magnitude near hub [14, 15]. The fact that the magnitude of swirl is highest near the hub may also be due to the fact that this geometry has a relatively sharp change in hub radius but a constant tip radius (see Figure 3.1). The majority of the swirl is very concentrated near 135 deg and 225 deg due to the sharpness of the transitions between high and low total pressure applied at those circumferential locations (see Figure 4.4).

The regions of dark red and dark blue in the near-stall contour plot are slightly larger than those in the design and choke plots. A given blue contour in the near-stall plot appears to be about two times the size of the corresponding blue contour in the design or choke case. A similar statement can be made of the red contours but with a factor of 1.5 instead of two. This suggests that there is greater swirl and mass redistribution at the near-stall case than at the design and choke cases. This is expected because the reduced mass flow rate at near-stall operating conditions correlates to reduced axial velocity. The tangential velocity, however, does not significantly change. Therefore, according to Equation 3.2, the near-stall case is expected to result in more pressure-induced swirl than the design and choke operating conditions. (See Figure 2.3 for a velocity triangle diagram that illustrates the relationship between axial velocity, tangential velocity, and swirl.)

Differences in swirl between near-stall and design and choke are more clearly shown in Figure 4.6, which plots the circumferential variations of pressure-induced swirl at the five radial locations of the rotor inlet. For all three operating points, the maximum swirl occurs at 10% span and the magnitude decreases as span is increased to 90%. The location of the maximum and minimum swirl magnitudes correspond with the 90 degree total pressure inlet distortion sector. Peak positive or negative swirl takes place where the distorted flow transitions into and out of distortion. The swirl profiles are the same for both the choke and design operating conditions. However, at the near-stall operating condition the swirl magnitude has increased. The co-swirl region of Figure 4.6 increases in magnitude by one to two degrees below 50% span. In the counter-swirl region the magnitude increases by one to three degrees at all spans. Co-swirl decreases the rotor incidence angle causing a deficit in power at that location. Counter-swirl increases the rotor incidence angle causing an increase in power. The relationship between inlet distortion, swirl, and power variation will be discussed at the end of this chapter.

4.4 Total Pressure Distortion Results

Analysis of the circumferential total pressure profiles and distortion amplitude at the five different radial spans and three operating conditions identifies the flow physics of total pressure distortion transfer through a rotor blade row. In general the total pressure results for the near-stall operating point differed significantly from the results for design and choke, and the greatest

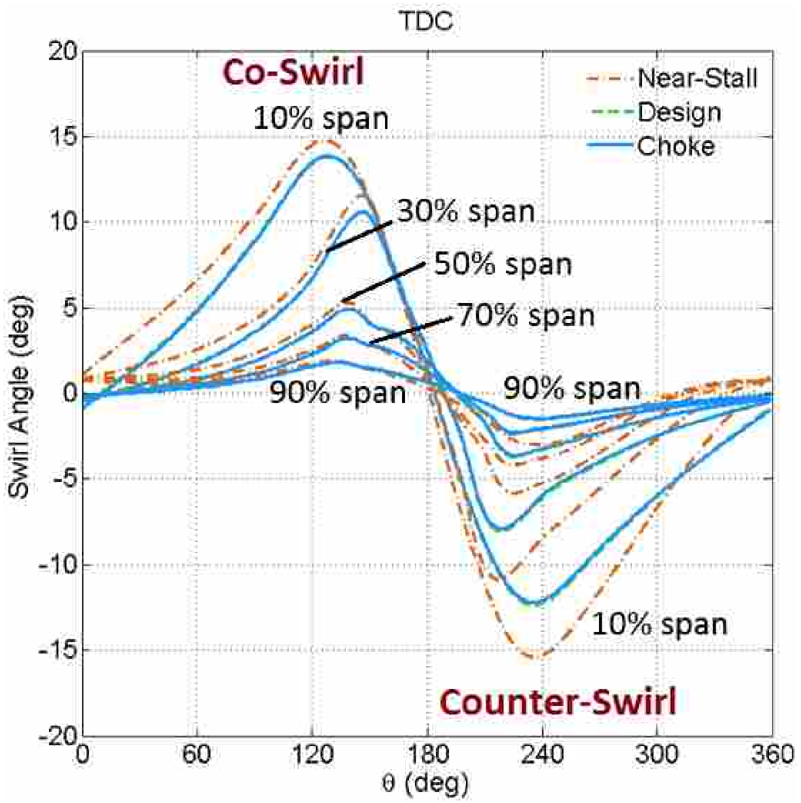

Figure 4.6: Circumferential variations of time-averaged swirl at the five radial locations.

differences occurred near the tip rather than the hub. These trends are shown and discussed in the total pressure traverses and total amplitudes sections.

4.4.1 Total Pressure Traverses

Circumferential traverses of time-averaged total pressure at the five radial locations are included in Figure 4.7 for the rotor inlet. These traverses were reconstructed from the first 12 modes of a Fourier series reconstruction (see Equation 2.5) of the original data in order to filter out the high-frequency perturbations from the blades. Figure 4.7 shows the results at the rotor inlet. As per the imposed total pressure distortion boundary condition the choke, design, and near-stall operating points all had the same traverses at the rotor inlet. Note that the small oscillations are due to the fact that this is a 12-mode Fourier reconstruction of square-wave-like data at the inlet. Including more of the Fourier modes in this representation would have smoothed away these oscillating patterns. The number 12 was chosen to filter the higher-frequency stator blade wakes out of the traverses at other axial locations, and so for consistency, 12 modes were used at the rotor inlet too.

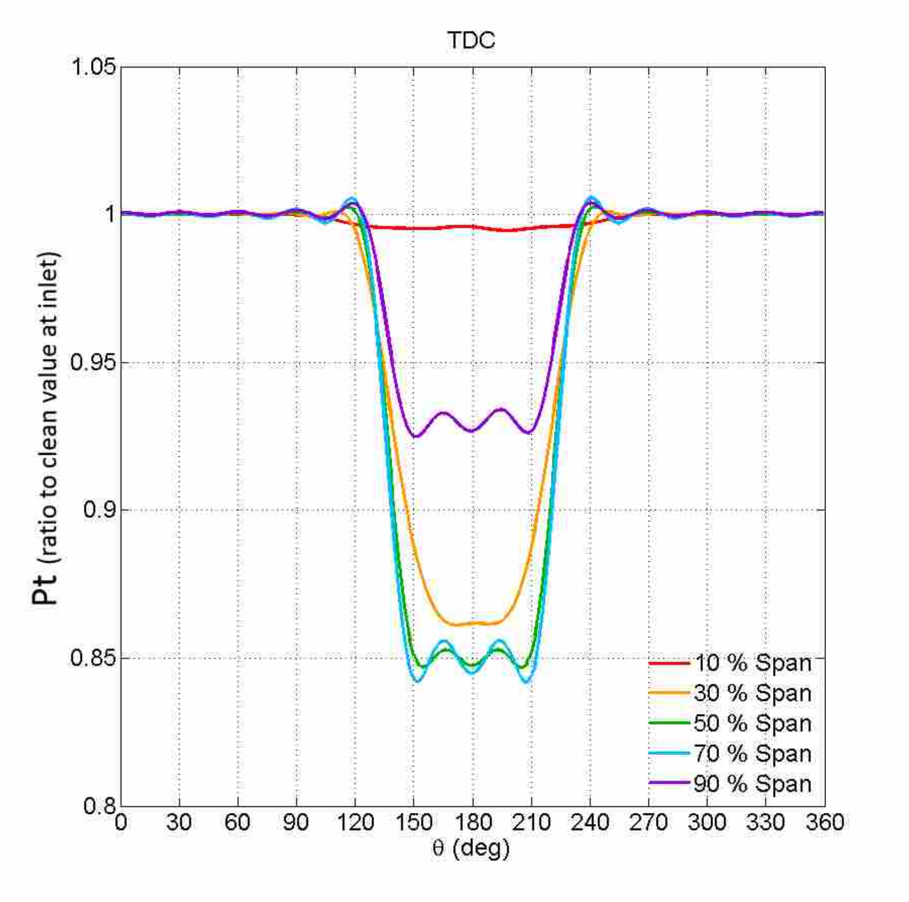

Figure 4.7: Fourier-reconstructed traverses of total pressure at rotor inlet.

Examples of time-averaged and time-accurate total pressure results are presented in Figure 4.8 and Figure 4.9 to give a reference for the amount of time-variation in this data. Both of these figures show total pressure traverses at the 10% span of the stator inlet for the near-stall operating point. Figure 4.8 shows a snapshot in time of the total pressure traverse compared to the time-averaged traverse. The snapshot follows the general pattern of the time-average with the exception that the snapshot shows peaks and valleys that represent rotor wakes. In the time-average, the rotor wakes are lost.

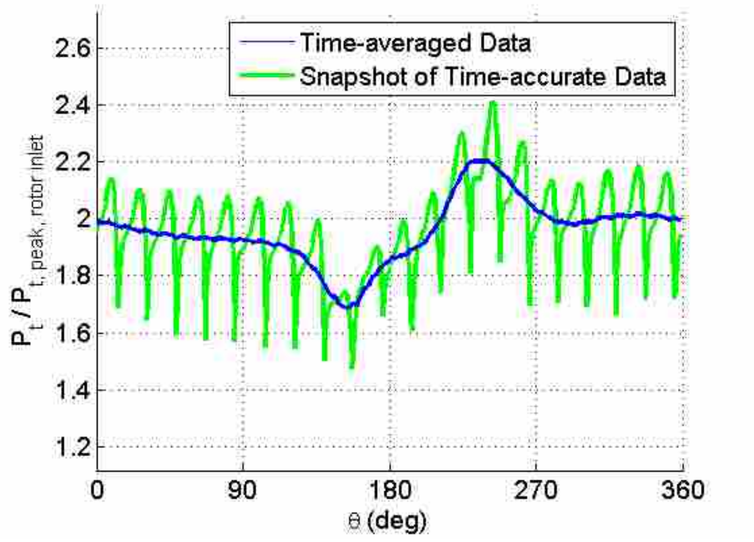

Figure 4.8: Comparing time-accurate snapshot to time-average. Total pressure traverses at 10% span of stator inlet for the near-stall simulation.

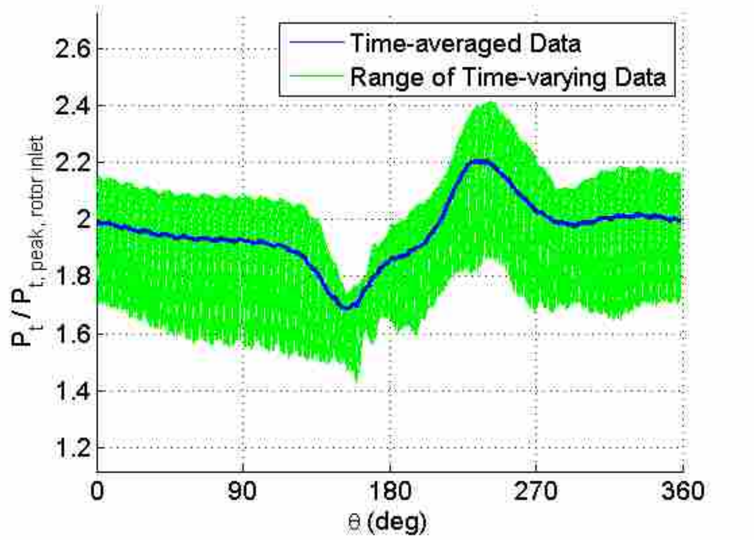

Figure 4.9: Comparing time-variation to time-average. Total pressure traverses at 10% span of stator inlet for the near-stall simulation.

Figure 4.9 shows the range of total pressure traverses that occur over time compared to the time-average. In this figure, 18 time-accurate snapshots are plotted together (one snapshot per degree of rotation for a blade-passing period). These 18 snapshots blend together in the figure to form an overall range of the time-varying data at each circumferential location. The peak-to-valley amplitude of the time-varying data is approximately twice the peak-to-valley amplitude of the time-averaged data. In this case, the time-averaged traverse is not directly in the middle of the maximum and minimum values of the range of time-varying data. The reason for this is illustrated in Figure 4.8 where at a snapshot in time, the wakes of the rotor blades have pointy valleys but wide peaks. This causes the average to be closer to the peaks.

Additional time-varying total pressure traverses are included in Appendix B to give more perspective on the relative magnitudes of the time variation compared to differences between operating point and radial location. The time-varying total pressure data is given for near-stall, design, and choke operating points at 10%, 50%, and 90% span. In general, at greater radial locations (nearer to the tip) the range of the time-varying data decreased. Also, from near-stall to design to choke the range of the time-varying data generally increased. For almost all the cases, the peak-to-valley amplitude of the time-varying data was approximately twice that of the time-averaged data.

Figure 4.10 presents the time-averaged results at the stator inlet for the three operating points. The plots in Figure 4.10 reveal that at progressively higher blade spans, the differences between the total pressure profile and magnitude at the three operating points increases. The plot of 10% span shows that all three operating points have almost identical total pressure profiles near the hub. The near-stall results are only slightly higher than the design and choke results. From 10% to 90% span the magnitude difference from choke to design to near-stall operating condition increases. By 90% span the near-stall results are significantly greater than the design results (the peak magnitudes differ by 0.24 of the clean value at the inlet). The design results are in turn significantly greater than the choke results (the peaks differ by 0.25). Although the greatest swirl was seen near the hub (see Figures 4.5 and 4.6), the greatest difference in total pressure between the three operating points occurs at the tip. This is because the tip generates more power (greater blade speed at greater radius), and so more of the total pressure increase associated with each operating point shows up nearer to the tip rather than the hub.

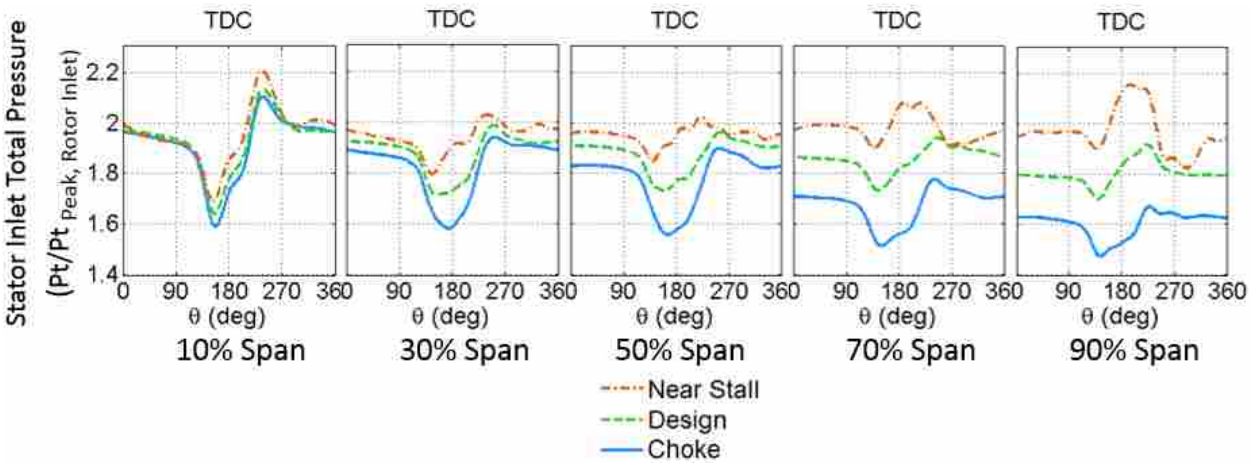

Figure 4.10: Fourier-reconstructed traverses of total pressure at stator inlet.

Figure 4.10 also shows that from 10% to 70% span, moving from near-stall to design to choke causes the amplitudes of the main peaks (those near 225 deg) to decrease, and the amplitudes of the main valleys (those near 135 deg) to increase. These amplitudes were calculated as the difference between the peak or valley and the average of the region outside of the distorted sector. At near-stall, the amplitudes of the valleys are 2% greater on average than the amplitudes of the peaks. At design, this difference is 9%, and at choke this difference is 19%. Therefore, the distorted portion has more positive net values near-stall compared to design and for design compared to choke. This was determined by calculating the maximum and minimum of each traverse as well as the average value of the portion of the traverse that is outside of the distorted sector.

As presented in Figure 4.10, a different total pressure profile exists near the tip for the near-stall operating point compared to the design and choke operating conditions. This is most evident in the plot at 90% span which shows that the choke and design cases each have a clear minimum near 135 degrees and a clear maximum near 215 degrees with a fairly constant value outside of the location of the distorted sector. The near-stall results, however, have a maximum near 190 degrees and two clear minimums, the lower of which being near 300 degrees.

4.4.2 Total Pressure Fourier Total Amplitudes

A plot of the total pressure total amplitudes at the stator inlet is shown in Figure 4.11. The amplitude is plotted as a fraction of clean values at the inlet. (See section 2.5 for a detailed description of the Fourier distortion descriptors.) Recall that the total amplitude is a measure of the total amount of distortion present at each percent span.

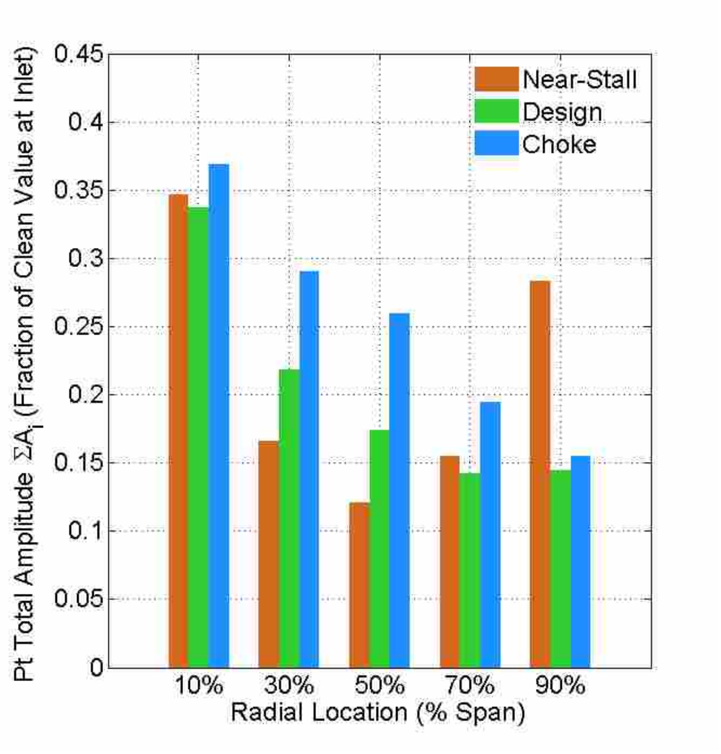

Figure 4.11: Total pressure total amplitudes at stator inlet.

Figure 4.11 shows that for the same inlet distortion profile, the amount of distortion transferred through the rotor is related to the percent span and the operating condition. At 10% span the highest amount of distortion is present, and it is independent of operating condition. At 30% and 50% span the distortion amplitude decreases from choke to design by 0.07 and from design to near-stall by 0.05. At 70% span the distortion amplitude decreases by 0.05 from choke to both design and near-stall operating conditions. At 90% span the choke and design operating conditions have a similar distortion magnitude but the near-stall distortion magnitude increases by 0.14. This correlates with the drastic change in shape seen in the 90% traverse of the near-stall simulation in Figure 4.10 where the peak at 190 degrees has significantly increased, and a large valley is seen near 300 degrees.

Another observation from Figure 4.11 is that for the near-stall operating point, the amplitude decreases by 0.23 from 10% to 50%, and then it increases by 0.16 from 50% to 90%. In contrast, for both the design and choke operating points, the amplitudes of distortion decrease by an average of 0.2 as radial location increases from 10% to 90% span. Altogether, this suggests that as a fan moves off design toward stall, increases of distortion transfer will occur near the tip. As a transonic rotor approaches the near-stall operating condition the increased distortion can lead to a part-span rotating stall cell that first forms near the tip. At mid-span there is less distortion and a stall cell would not begin forming.

4.4.3 Total Pressure Phase Shifts Across Rotor

The total pressure phase shifts across the rotor are shown in Figure 4.12, and they represent the circumferential rotation of the distorted region as it passes through the rotor. Changes in the shape of the distortion pattern from rotor inlet to rotor exit can also be inferred. These phase shifts are the simplified type defined in Figure 3.8, rather than those introduced by Peterson [22].

As shown in Figure 4.12, the near-stall operating point has the smallest (most negative, i.e. most counter-clockwise) values. The phase shift is about 15 degrees from 10% to 30% span, near zero degrees from 50% to 70% span, and -14 degrees at 90% span. The design and choke simulations have very similar phase shift values to each other, with the choke simulation having a slightly more positive shift (35 deg vs 23 deg) at 30% span. The shifts for these two operating points become more positive from hub (about 18 deg) to the midspans (about 30 deg), and then they become more negative from midspan (about 30 deg) to tip (about 4 deg). The fact that design and choke phase shifts matched well but that the near-stall phase shifts differed suggests that there is similar distortion transfer behavior between design and choke, but that distortion transfer has markedly different behavior near stall.

It may seem counter-intuitive that the near-stall case in Figure 4.12 was calculated to have a negative phase shift at 90% span because that would suggest the flow shifted against the direction of blade rotation. This may be a result of limitations of the method used for quantifying phase shift. Phase shift was calculated based on the locations of minimum and maximum values of total pressure. It was expected that as long as the shape didn't change too much, then this method would give reasonable results from which qualitative trends could be seen. At the 90% span for the near-stall case, the shape changed significantly which may have decreased the accuracy of the calculated phase shift in that case. It is worth noting however, that another study involving a fan with inlet distortion (see [14]) resulted in a negative phase shift near stall and positive phase shifts at design and choke operating points. Future work would be beneficial to analyze these findings and the mechanisms that may be driving them.

By comparing the phase shifts to Figure 3.7 where the center for all spans was 180 degrees, the change in distortion profile shape presented in Figure 4.4 has been quantitatively described.

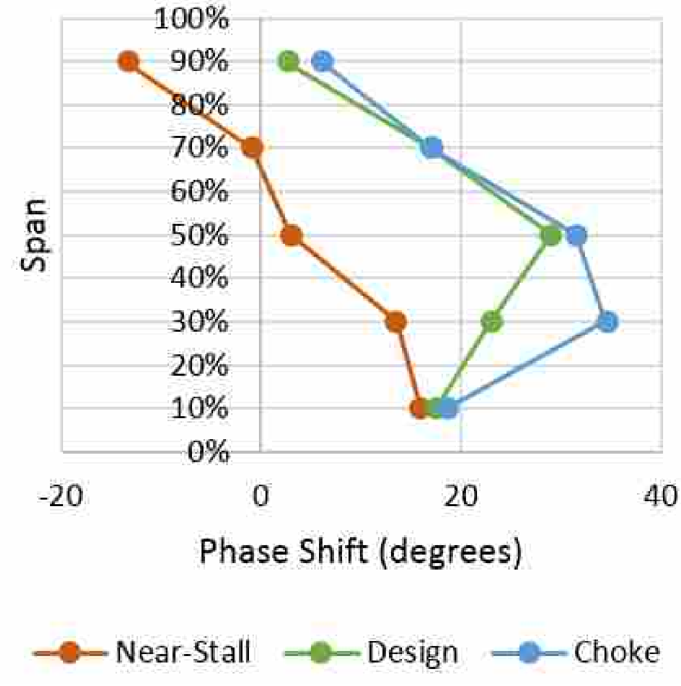

Figure 4.12: Phase shift of total pressure across rotor 4.

4.5 Total Temperature Distortion Results

Total temperature distortion is generated as total pressure distortion is transferred through a rotor. Analysis of total temperature circumferential profiles and distortion amplitude at five spans and three operating conditions will show evidence of circumferential power variation.

4.5.1 Total Temperature Traverses

Circumferential traverses of time-averaged total temperature at the five radial locations are included in Figure 4.13. These traverses of total temperature were reconstructed from the first 12 modes of the Fourier series of the original data in order to filter out the high-frequency perturbations from the blades.

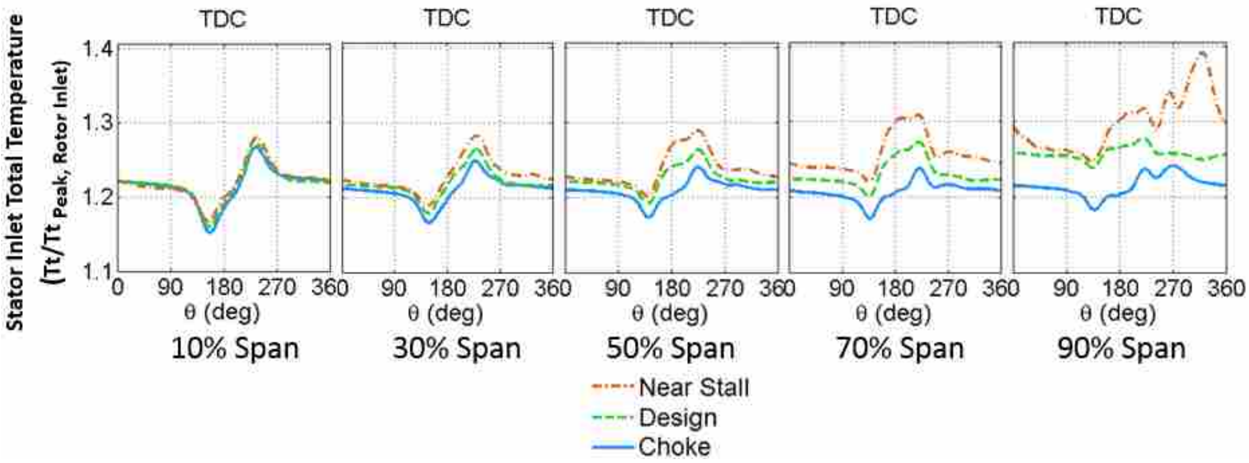

Figure 4.13: Fourier-reconstructed traverses of total temperature at stator inlet.

The total temperature results follow the same trends as the total pressure results of Figure 4.10. The data shown in Figure 4.13 reveals that at successively greater span, the difference in magnitude between the total temperature profiles of the three operating points increased. The profile shape is similar for all spans except 90%. Peaks and valleys corresponding to the borders of the inlet total pressure distortion sector are visible at all circumferential locations except 90% span near-stall operating condition.

The plot of 10% span shows that all three operating points have almost identical total temperature profiles near the hub. At 90% span, however, the near-stall results are significantly greater than the design results (the peaks differ by 0.11 of the clean value at the inlet). The design results are in turn significantly greater than the choke results (the peaks differ by .04). Thus the total temperature distortion generation near the hub is independent of operating point, but distortion generation near the tip greatly varies with operating point.

Figure 4.13 also shows that the total temperature distortion at the near-stall operating point had significant profile shape change near the tip. The total temperature traverse at 90% span had an extremely high peak at about 315 degrees that extended over twice as high as the expected local peak at about 225 degrees. This traverse has changed shape so much that there is very little "clean" portion remaining. This shows that the greatest amount of distortion generation occurs near the tip when operating at near-stall conditions, and its behavior is significantly different from that at the design and choke operating points.

Similar to the total pressure profiles, Figure 4.13 shows that between 10% and 70% span, moving from near-stall to design to choke operating condition caused the amplitudes of the main peaks (distortion boundary near 225 degrees where counter-swirl is present) to decrease, and the amplitudes of the main valleys (distortion boundary near 135 degrees where co-swirl is present) to increase. At near-stall operating conditions, the amplitudes of the peaks are 2% greater on average than the amplitudes of the valleys. At design, this difference is 1%, and at choke this difference is -1%. In other words, the distortion generation has more positive net values for near-stall than for design and for design than for choke.

Relating observations from Figure 4.13 to what was discovered about induced swirl and total pressure distortion transfer, some insights on total temperature distortion generation can be made. The location of total temperature distortion generation shows it is a result of distortion transfer with induced swirl as the cause. Considering the fan to be adiabatic, the mechanism that changed the total temperature profile and magnitude is circumferential power variation. At 10% span the total pressure profile in Figure 4.10 is nearly the same for all three operating conditions.

Similarly at 10% span the total temperature profile in Figure 4.13 similar for all three operating conditions. As the percent span increases and the difference in total pressure profiles of Figure 4.10 increases from choke to near-stall operating condition the corresponding total temperature profiles of Figure 4.10 also showed greater difference.

4.5.2 Total Temperature Fourier Total Amplitudes

The total temperature total amplitudes at the stator inlet are shown in Figure 4.14. As was done for total pressure, the amplitude is presented as a fraction of corresponding clean values at the inlet and represents a measure of the total temperature distortion generated and present at the stator inlet. Figure 4.14 shows that from near-stall to design, the total amplitude decreases at all spans. The amount of decrease increases with radial location. The most dramatic change is at the 90% span where the total amplitude of total temperature for the near-stall operating point is more than three times the value of the design operating point. This correlates with the drastic change in shape seen in the 90% traverse of the near-stall simulation in Figure 4.13 where peaks and valleys cover most of the circumference including an extremely high peak at about 315 degrees. From design to choke the total amplitude decreases at 30%, 50%, and 70% spans (with an average of 0.007), but increases slightly by 0.01 at 90% span. This contrasts with the total pressure results which were shown in Figure 4.11 to increase from design to choke at all spans. Changes in total temperature are a result of changes in rotor power which is addressed in the next section.

At near-stall operating condition the amplitude of total temperature distortion in Figure 4.14 decreases (by 0.01) from 10% to 30%, and then increases (by 0.05) from 30% to 90%. For design and choke operating conditions the amount of temperature distortion decreases from 10% span to 90% span with the exception of the design operating condition at 70% span which was slightly higher than the 50% magnitude.

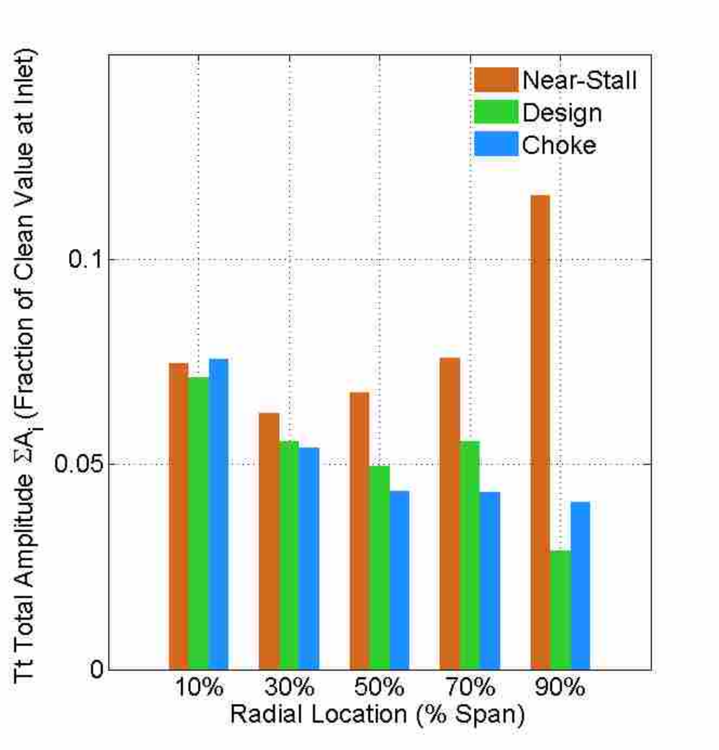

Figure 4.14: Total temperature total amplitudes at stator inlet.

4.5.3 Total Temperature Phase Shifts Across Rotor

The total temperature phase shifts across the rotor are shown in Figure 4.15. These are the simplified phase shifts that were defined previously in Figure 3.8. All three operating points have almost identical values of phase shift at the 10% through 70% spans, with variations of only three or four degrees at the 90% span. Phase shift is more positive (clockwise) near the hub (about 16 deg) than near the tip (about 0 deg).

These phase shift values help quantify the shape of the total temperature distortion region that is generated across the rotor. They show that all three operating points shift clockwise near the hub, but do not shift very much at all at the tip. This is evident in Figure 4.4 where the distorted portion of the total temperature contours is clockwise of TDC near the hub, but closer to TDC near the tip.

Comparing Figure 4.15 to Figure 4.12 reveals the phase lag between the total pressure distortion and the total temperature distortion. The design and choke operating points show that

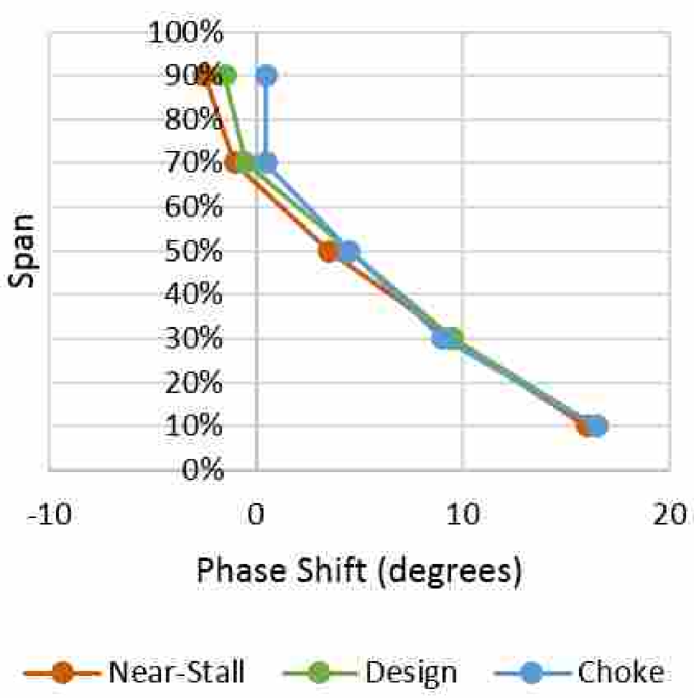

Figure 4.15: Phase shift of total temperature across rotor 4.

the total temperature distortion lags behind the total pressure distortion. The radial average of the lag is 12 degrees for design and 15 degrees for choke. The near-stall operating point, however, has almost no lag. Its total pressure phase shifts are much different from those of design and choke. This further highlights the unique distortion transfer behavior of this fan stage's operation at near-stall compared to that of design and choke.

Other studies have shown that total temperature phase lags behind total pressure phase [2, 3, 14], but by a much greater amount (closer to 90 degrees). The greater lag in the previous studies is likely due to the fact that those studies used sinusoidal profiles instead of a sector with sharp transitions. Examining the effect of inlet distortion shape (particularly the abruptness of transition) on the phase lag between total pressure and total temperature would be an interesting topic for future research.

4.6 Power Variations at Design Operating Point: A Comparison of Simplified Streamtube Method and Blade Loading Method

Distributions of power ($\dot{W}$) for the rotor were calculated to further anlalyze the distortion transfer and generation that occur across the rotor. The results for the design operating point are used to compare multiple methods for quantifying power variations. The optimal method is then chosen and used in the following section to compare results at all three operating points.

The power results of the simplified streamtube method and the blade loading method are shown in Figure 4.16 for the design operating point. (See sections 3.1.7 and 3.1.8 for descriptions of these two methods.) For the data in this plot, the streamtube method was executed using evenly-spaced radii so that the average radii in the annuli were at the same locations evaluated with the blade loading method, (10%, 30%, 50%, 70%, and 90% span). The results from the streamtube method are depicted with solid lines, and the results from the blade loading method are depicted with dotted lines and markers.

Both methods calculated that the most power is generated in the areas near the tip (in Figure 4.16, see streamtube annuli 4 and 5, and blade loading 70% and 90% span), and the least power is generated in the areas near the hub (see streamtube annuli 1 and 2, and blade loading 10% and 30% span). In general, the farther from the hub, the greater the power.

Figure 4.16 also shows that both methods predict that each radial location has a distinct circumferential maximum and minimum. For a given radial location, the minimum power occurs between 120 degrees and 150 degrees. This is the approximate location where the blades enter the distorted region (135 degrees), which is also the location of co-swirl at the rotor inlet. The maximum power at each span occurs between 210 degrees and 240 degrees. This is the approximate location where the rotor blades exit the distorted region (225 degrees), or the location of counter-swirl. These findings agree with the previously-mentioned studies where it has been shown that co-swirl at a rotor inlet correlates to less power and counter-swirl correlates to more power because of the lower and higher incidence angles, respectively [1, 14, 15, 31].

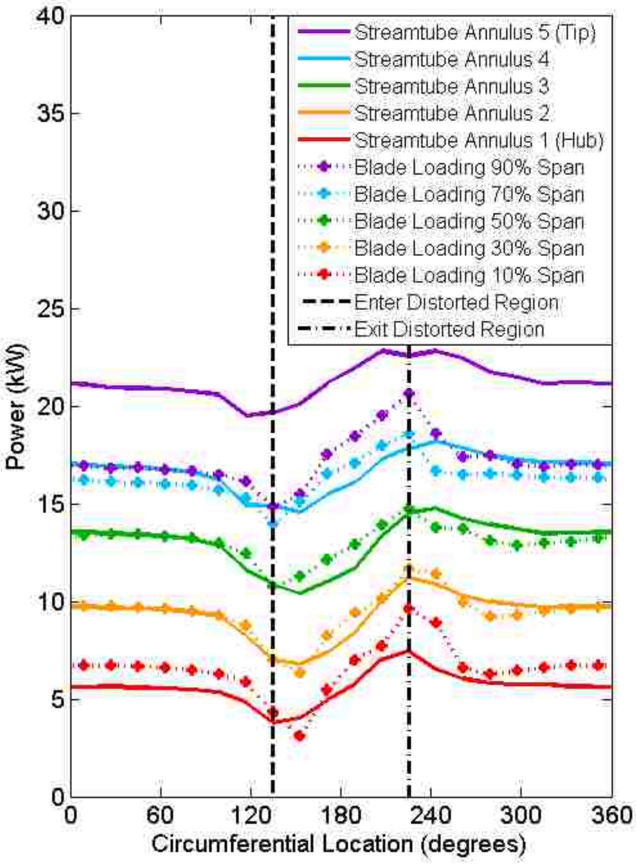

Figure 4.16: Local variations in power achieved by the rotor at 10%, 30%, 50%, 70%, and 90% span using the streamtube method and the blade loading method. The streamtube method was used with evenly-spaced radii in this case so that the average radii in the annuli occur at the same locations evaluated with the blade loading method.

The streamtube results in Figure 4.16 match very well with the blade loading results at 30%, 50%, and 70% span, and they match fairly well at 10% span. The blade loading results at 90% span, however are different from the streamtube results in Annulus 5, but this may be explained by the effects of the tip gap. Viscous effects and tip clearance vortices cause higher total temperatures to be generated in the tip than at other radial locations. Because power is directly proportional to the change in total temperature (see equation 3.3), this causes the streamtube method to predict slightly higher amounts of power there than it otherwise would without a tip gap. This may indicate that the streamtube method is inappropriate in locations such as the tip gap where there are significant vortices and viscous effects. The blade loading method, however, makes calculations based on static pressure at cross-sections on the blade rather than total temperature averages in each annulus sector. Because of this, the results of the blade loading method may be more valid near the tip than the results of the streamtube method.

Other differences between the results of each method are likely due to limitations or poor assumptions made for the streamtube method. Perhaps the poorest assumption for the streamtube analysis is that through the rotor each streamtube shifts exactly 17 degrees clockwise. This value is the approximate average shift of the distorted sector for all radial locations, but a more elaborate analysis could be done in which the shift varies radially. Additionally, significantly more analysis could be performed to account for circumferential variations in shift, but these efforts would greatly increase the complexity of the method. The purpose was to introduce a simple method that could reveal general qualitative trends of radial and circumferential variations in power. This purpose is achieved even with the constant shift assumption.

Although the results shown in Figure 4.16 match very well between the two methods, the validity of using evenly-spaced radial locations to analyze power must be considered. The streamtube method is based on the assumption that the streamtubes closely approximate the streamlines through the blade row. A common approach to approximate the radial paths of streamlines is to define the annuli at the inlet boundary in a way such that the area of each annulus is equal to the others, and then to do the same at the outlet boundary. For this reason, the streamtube method was executed again but with equal-area annuli. The results are shown in Figure 4.17.

Figure 4.17 reveals that many of the qualitative trends that were noted for the evenly-spaced radii results are also seen in the equal-area results. In general, the power increases with radial location. Also, the results at each radial location have a minimum near 135 degrees and a maximum near 225 degrees, which are the locations of co- and counter-swirl, respectively.

Three additional insights are gained from the equal-area results presented in Figure 4.17. First, using the equal-area approach results in a much smaller range of values. The equal-area power results (Figure 4.17) range from 7 kW to 16 kW, whereas the evenly-spaced radii results (Figure 4.16) range from 3 kW to 23 kW.

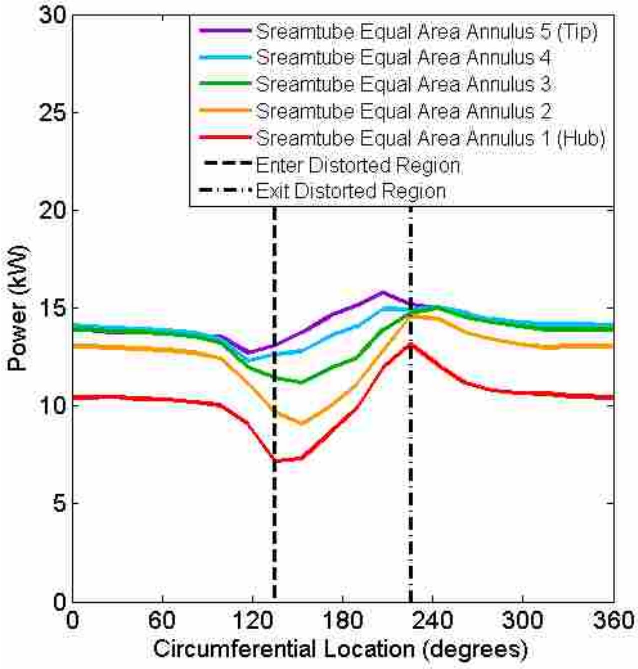

Figure 4.17: Local variations in the power achieved by the rotor as calculated with the simplified streamtube method using equal-area annuli.

A second insight is that the equal-areas results (Figure 4.17) appear to vary nonlinearly with radial location. Outside the distorted sector, annuli 3, 4, and 5 have almost identical power values (14 kW) with annulus 2 having only slightly lower power (13 kW). In contrast, the evenly-spaced radii results (Figure 4.16) appear to vary linearly with radial location.

Finally, even though the power increases with radial location, Figure 4.17 shows that the annuli closer to the hub have the greatest magnitude of distortion (difference between min and max power). This is directly correlated with the distribution of swirl present at the rotor leading edge that is shown in Figure 4.5 and Figure 4.6. The greatest magnitudes of swirl are concentrated near the hub. This causes the angles of incidence nearest the hub to be lower and higher in the co- and counter-swirl regions, respectively, which leads to greater variations in power near the hub.

The simplified streamtube method and the blade loading method each have limitations, but both methods were shown to provide valuable insights into local variations of power in a fan or compressor. For the study of power variation at three different operating points, the blade loading method was chosen over the streamtube method. This is because the assumptions made for the streamtube method were deemed less valid than those for the blade loading method. (The assumption that the streamtubes all have the same amount of shift was considered most invalid.) The blade loading method is also desirable because it enables direct comparison to the total pressure and total temperature results at the same radial locations (10%, 30%, 50%, 70%, and 90% span). For these reasons, the blade loading method was determined to be more appropriate than the streamtube method for comparing local power variations at all three operating points.

4.7 Local Power Variation at Three Operating Points

The blade loading method was used to compare the local power variations from choke to design to near-stall. Distributions of power at the 10%, 30%, 50%, 70%, and 90% span are shown in Figure 4.18 for the three operating points. The profile shape and magnitude differences follow the trends observed in total pressure (Figure 4.10) and total temperature (Figure 4.13). For most of the traverses, there is a drop in power near 135 degrees and a peak in power near 215 degrees. These correspond to the locations of co- and counter-swirl associated with the 90 degree inlet total pressure distortion profile. Two exceptions to this trend are at 70% and 90% spans for the near-stall operating point, which have very subtle drops and very large peaks. That is the same general shape that was noticed in Figure 4.10.

All three operating points have similar power results near the hub but the results differ greatly near the tip. The results at 10% span are almost identical for each operating condition, but as percent span increases, so does the difference between the power profiles of the choke, design, and near-stall operating conditions, ultimately differing from near-stall to choke by an average of 5kW. At 50% span and above, rotor operation at the near-stall operating point has greater power (more work performed) than at the design operating condition. Further, there is more power at design than choke operating condition. These trends were seen in the Fourier total pressure and total temperature plots in Figure 4.10 and Figure 4.13.

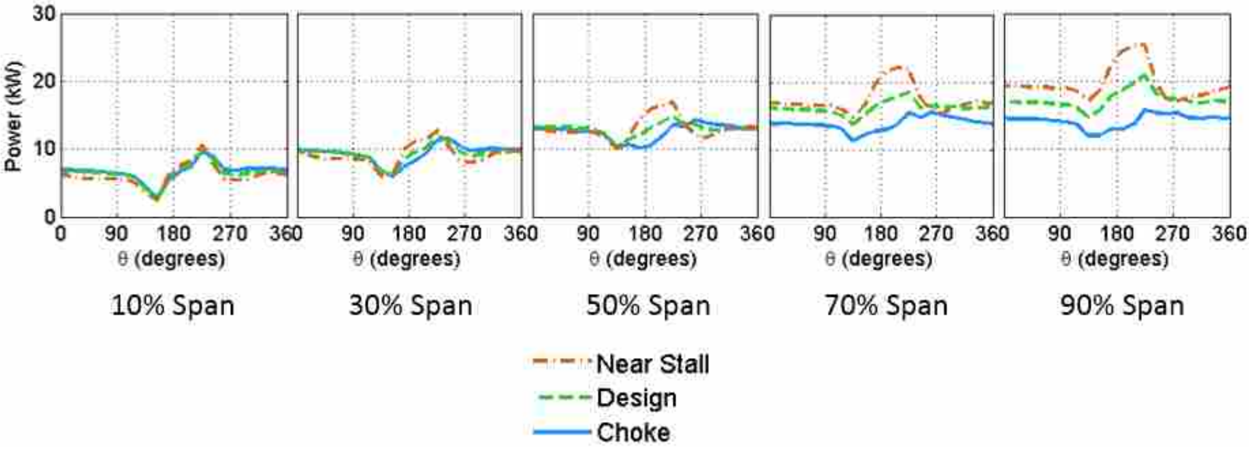

Figure 4.18: Traverses of local power achieved by rotor 4. Calculated using the blade loading method.

4.7.1 Discussion: Relationships between Inlet Distortion, Induced Swirl, Total Pressure Distortion Transfer, Total Temperature Distortion Generation, and Power Variation

A clear picture of the flow physics and mechanisms associated with distortion transfer and generation can be obtained by considering how total pressure, swirl, power, and total temperature in this flow are related. An inlet total pressure distortion induces swirl at the inlet of the fan rotor. The applied total pressure distortion profile shown in Figure 3.7 generated pressure-induced swirl shown in Figure 4.5 and Figure 4.6. For the inlet distortion profile used in this study, positive swirl peaked near 135 degrees (distortion boundary where co-swirl was present) and negative swirl was greatest near 225 degrees (distortion boundary where counter-swirl was present). Counter-swirl increases the incidence angle of the flow on the rotor blade. This increases the overall blade turning angle causing those blades in the counter-swirl zone to generate more power than they would without the increased incidence. This additional power increases the total pressure magnitude as shown in Figure 4.10 near 225 degrees. Co-swirl decreases the rotor incidence angle, causing the overall blade turning to be less, and therefore the blade generates less power than without decreased incidence. This is manifest as a minimum total pressure magnitude near 135 degrees. Therefore the peak total pressure is observed where counter-swirl is greatest and the minimum total pressure magnitude is observed where co-swirl is greatest. Distinct regions of lower power near 135 degrees and greater power near 225 degrees are shown in Figure 4.18 confirming the relationship between induced swirl and power variation. The regions of less power result in lower total temperature and the regions of greater power result in higher total temperature. This is confirmed in Figure 4.13 by the low level of total temperature near 135 degrees and the high level of total temperature near 225 degrees.

The gradients of induced swirl are greatest at the boundaries of the inlet distortion sector. The peaks and valleys related to the edges of the inlet distortion are observed in the swirl (Figure 4.6), total pressure (Figure 4.10), total temperature (Figure 4.13), and power (Figure 4.18) profiles. It can therefore be concluded that the abruptness or smoothness of the transition from undistorted to distorted flow at the inlet to a rotor is important and will affect the amount of induced swirl, the distribution of power, and the total temperature distortion generation. The exact relationships between the transition abruptness and the swirl and power variations are a topic recommended for future research.

CHAPTER 5. RESULTS OF HARMONIC BALANCE STUDY WITH NASA ROTOR 37

In this chapter, results are provided for the study involving NASA Rotor 37. The objectives of this study were to perform Harmonic Balance and Full-annulus URANS simulations with varying inlet distortion profiles, and to analyze trends in distortion and performance measures. The specified HB mode combinations are compared in their abilities to match the URANS results. The findings of this HB study are compared to the findings of Peterson's HB study [4]. Recommendations of the optimal mode combinations are made based on two potential design priorities: 1) the most computationally efficient mode combination that accurately predicts distortion transfer and generation; 2) the most computationally efficient mode combination that accurately predicts performance.

5.1 Mode Combinations and Blade Rows

The meaning of mode combinations and the conventions used for this thesis were defined in Figure 1.2 and the Harmonic Balance discussion in chapter 1. A complete list of the mode combinations simulated including whether each simulation converged or diverged is given in appendix B. The mode combinations of primary interest to investigate were HB100, HB111, HB200, HB211, HB300, HB311, HB400, HB411, HB500, and HB511 because these combinations most clearly reveal the effects of the number of modes at the inlet boundary as well as the effects of including modes in the blade rows.

The configuration for this study is an IGV followed by a rotor, and so the first number in an HB mode combination corresponds to the inlet boundary, the second number corresponds to the IGV blade row, and the third number corresponds to the rotor blade row. This is different from Peterson's configuration which consisted of a rotor blade row followed by a stator blade row.

Recall that the number of modes specified in a blade row determines the amount of information from that particular blade row that is passed on and allowed to interact with the flow in the other blade row(s). This means that the number of modes in a blade row will not directly change the accuracy in that blade row. It will, however, affect how much information is passed upstream and downstream, affecting the results in the other blade row(s).

5.2 Inconsistencies in the Harmonic Balance Results

No one mode combination proved to consistently be the best match of the URANS simulations in every metric. Some of the simulations converged with lower and more regular residuals than others. Some of the simulations diverged for no apparent reason (HB131, HB221, HB222, and HB411). A technical specialist who helped implement Harmonic Balance in STAR-CCM+ was consulted about these findings. He did not have definite answers for why some mode combinations converged and others did not, but he suggested that one possible cause for the observed inconsistency was the relationship between mesh and mode combination. The HB solver operates differently based on how many modes are specified. In general, higher combinations require a more refined mesh in order to give reasonable results in every metric. Some evidence of this trend was found in this study: many of the higher combinations of modes either diverged or had poorer convergence than others. The level of refinement that was chosen was limited by the computing resources available. A grid convergence study showed the mesh was sufficiently refined for achieving accurate performance measures, but it appears that an even finer grid may have been optimal in order to minimize inconsistency associated with some of the distortion descriptors. This may be related to the number of cells required in order to avoid aliasing (defined in equation 5.1), but this mesh had 37 cells in the circumferential direction, which should have been sufficient to avoid aliasing for computations with up to 18 modes.

$$Cells = 2 * Modes + 1 \tag{5.1}$$

Another possible cause for the observed inconsistency is that there may have been flaws in the mesh that hindered the ability of the HB solver to successfully converge. Flaws in the mesh can be independent of the level of refinement; examples are negative-volume cells and highly-skewed cells. Peterson suggested flaws in the mesh as a possible explanation for similar problems he encountered. His 7.5% distortion HB simulations successfully converged, but all of his attempted 15% distortion HB simulations diverged. He hypothesized that if he were able to find the problem areas in his mesh and repair them then his 15% simulations may have converged just as his 7.5% simulations did.

Although there was inconsistency in the Harmonic Balance results, some useful trends were noticed and are discussed at length in this chapter.

5.3 Total Pressure and Total Temperature

Contour plots were generated to show time-averaged total pressure and total temperature at the rotor outlet boundary for each simulation. Figure 5.1 shows these profiles for the HB111, HB311, and full-annulus URANS simulations with the 15% 1-per-rev inlet profile.

The contour plots in Figure 5.1 offer insight into the way that the HB solver operates in comparison to the URANS solver. The URANS plots have no visible perturbations around the annulus, but the HB plots have 48 distinct perturbations which is the number of IGV blades. No rotor blade perturbations are visible because the profiles are time-averaged from the perspective of a stationary reference frame. The magnitudes of the perturbations in the HB311 plots are significantly less than the magnitudes of the perturbations in the HB111 plots suggesting that including more modes allows the HB simulations to better match the URANS simulation. The fact that blade perturbations are visible at the rotor outlet only for the HB simulations is likely due in part to the different boundary condition treatment used by each of the solvers. The URANS solver in STAR-CCM+ uses reflecting boundary conditions (RBC) whereas the HB solver uses non-reflecting boundary conditions (NRBC).

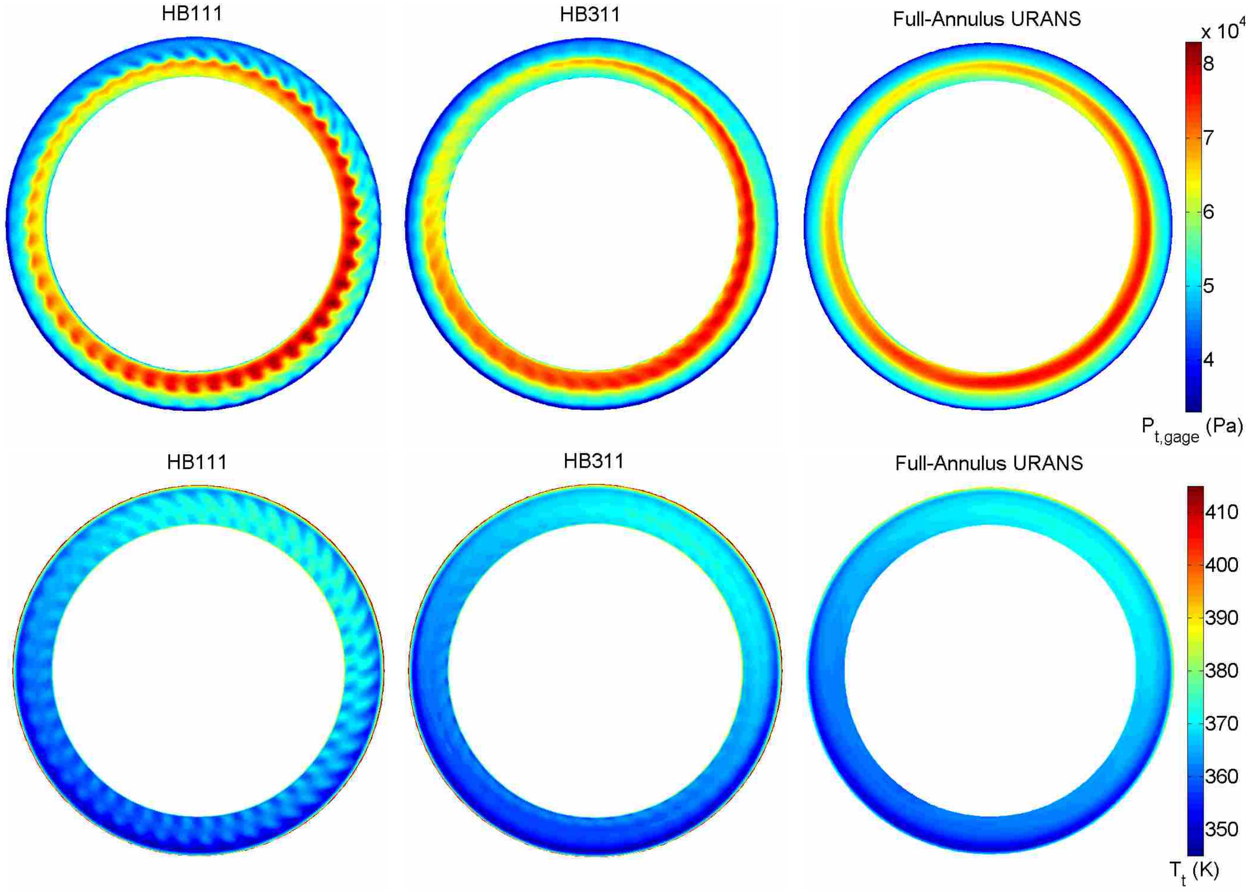

Figure 5.1: Time-averaged total pressure (top row) and total temperature (bottom row) at the rotor outlet for the 15% 1-per-rev simulations. Note that the values for total pressure are gage rather than absolute.

In a recent study with a turbine developed by the University of Aachen, it was shown that having an RBC corrupted the static pressure field [19]. Static pressure disturbances were not allowed to exit the domain because the boundary was kept at a constant value. The same observation is made of the boundary treatment for the present study as shown in Figure 5.2, which shows the time-averaged static pressure at the exit of the rotor 37 domain for a Full-Annulus URANS simulation and for an HB111 simulation. The RBCs with the URANS solver keep the outlet static pressure at its applied constant value whereas the NRBCs with the HB solver allow properties to vary spatially to account for disturbances from the blades. It is impossible to know exactly how much of a factor the RBCs are in the total pressure results at the outlet, but the corruption of the static pressure field near the rotor outlet boundary for the URANS simulation likely affects the total pressure and total temperature fields at that location causing the disturbances to not be apparent for the URANS plots in Figure 5.1. One way to minimize the effects of this difference in boundary condition treatment would be to extend the domain for both the HB and URANS simulations far from the blades so that disturbances could be more fully resolved before they reach the boundaries. Another solution may be to apply a radially-varying static pressure profile at the exit that better matches the expected outlet profile as done by Yao et al. in [2, 3].

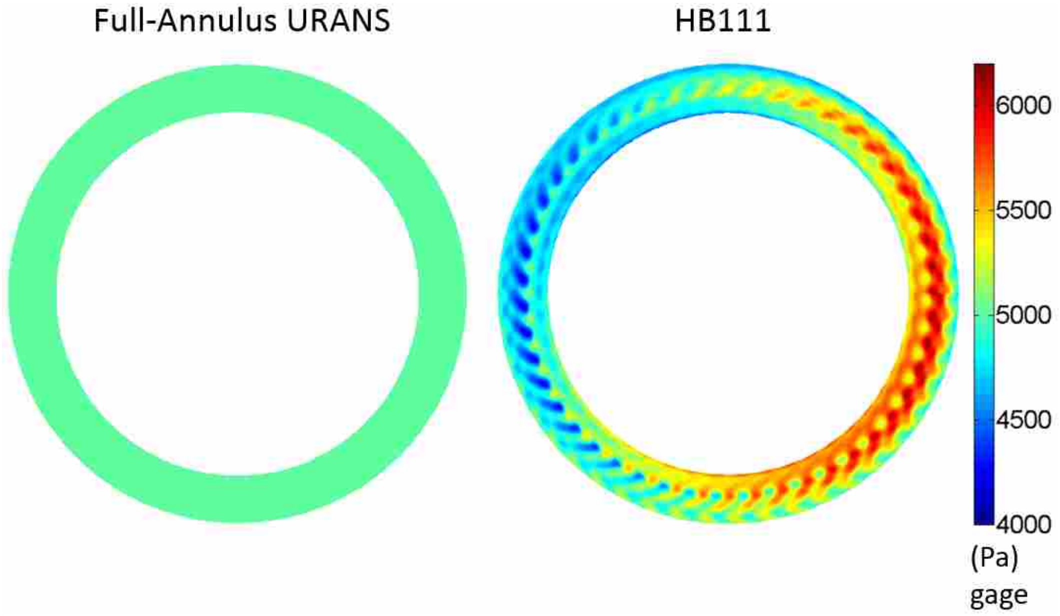

Figure 5.2: Time-averaged static pressure profiles at the rotor exit boundary for 15% 1-per-rev simulations. Left: URANS. Right: HB111.

Although the RBCs with the URANS solver in STAR-CCM+ prevent pressure disturbances from properly resolving at the outlet boundary, the RBCs at the inlet boundary cause the distortion profile to be more accurately applied for URANS simulations than for HB simulations. For the URANS solver, total pressure and total temperature were strictly held at their specified values. With the HB solver, however, the specified inlet properties were not strictly applied by the solver. For the 15% distortion profile, the HB simulations indicated that the inlet had about 15.6% distortion. For the 20% profile, the HB simulations indicated that the inlet boundary actually had about

21.6% distortion. These discrepancies illustrate that it can be a challenge to apply the exact same boundary conditions for a URANS simulation and for an HB simulation. One way to improve results in the future may be to run some of the HB simulations with the applied amount of distortion and the maximum total pressure each offset slightly to account for the differences introduced by the HB solver.

5.4 Distortion Results

In addition to contour plots of total pressure and total temperature, Fourier techniques were used to quantify the differences between the amounts of distortion captured in each simulation. The three Fourier distortion descriptors (described in section 2.5) are presented in this chapter: total amplitude, modal amplitude, and modal phase shift. Note that the modal phase shift in this chapter is that introduced by Peterson in [4] rather than the simplified phase shift defined in Figure 3.8. This was done to be consistent with Peterson's methods and therefore allow a better comparison with his results at the end of this chapter.

The values of the distortion descriptors for the HB simulations are then compared to the values for the URANS simulations. It should be noted that both the URANS and HB solvers have limitations, but the URANS type of solver is traditionally accepted as the most high-fidelity computational method that is practical for 3D turbomachinery, and so it is assumed to have less limitations than the HB solver. Particularly, in considering the pros and cons of the URANS solver, it was decided that the greater accuracy at the inlet boundary condition given by the URANS solver made the URANS solver a good option for a standard of comparison. For this reason, the URANS simulations are used as a baseline against which the results of the HB simulations can be compared. Differences are reported as percentages. The results for the 15% 1-per-rev simulations are presented in greatest detail, and then general trends are discussed for the other distortion profiles. As described in section 3.2.5 and figure 3.18, the inlet profiles that were studied were 1-per-rev and 2-per-rev sinusoidal shapes with 10%, 15%, and 20% total pressure distortion.

5.4.1 Total Amplitude Results

Total amplitude was compared for the various HB simulations to see how close each one was to the URANS results. Recall that total amplitude is a measure of the distortion present at a location in the compressor, and it can be useful for describing the amount of distortion transfer and generation at a location with one number. The total amplitude results and the % difference from the URANS results are shown in tables 5.1 and 5.2 for several of the 15% 1-per-rev simulations to compare the abilities of the different HB combinations at predicting distortion transfer and generation.

Table 5.1: Total pressure total amplitude (radially averaged).

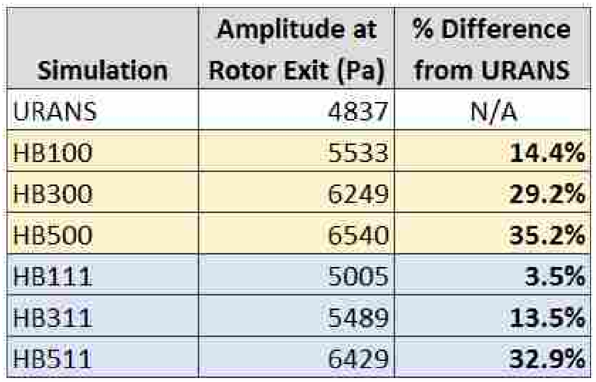

Simulation	Amplitude at Rotor Exit (Pa)	% Difference from URANS
URANS	4837	N/A
HB100	5533	**14.4%**
HB300	6249	**29.2%**
HB500	6540	**35.2%**
HB111	5005	**3.5%**
HB311	5489	**13.5%**
HB511	6429	**32.9%**

Table 5.2: Total temperature total amplitude (radially averaged).

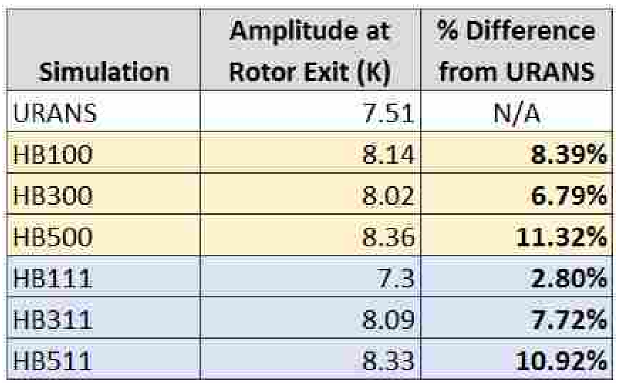

Simulation	Amplitude at Rotor Exit (K)	% Difference from URANS
URANS	7.51	N/A
HB100	8.14	**8.39%**
HB300	8.02	**6.79%**
HB500	8.36	**11.32%**
HB111	7.3	**2.80%**
HB311	8.09	**7.72%**
HB511	8.33	**10.92%**

Tables 5.1 and 5.2 reveal that the total amplitude results of the HB simulations become farther and farther off from the URANS simulations as more modes are included. Typically the opposite is expected: including more modes usually results in greater accuracy. This phenomenon can be explained by considering the shape of the inlet distortion profile and by examining the modal amplitude results (shown in Figure 5.3).

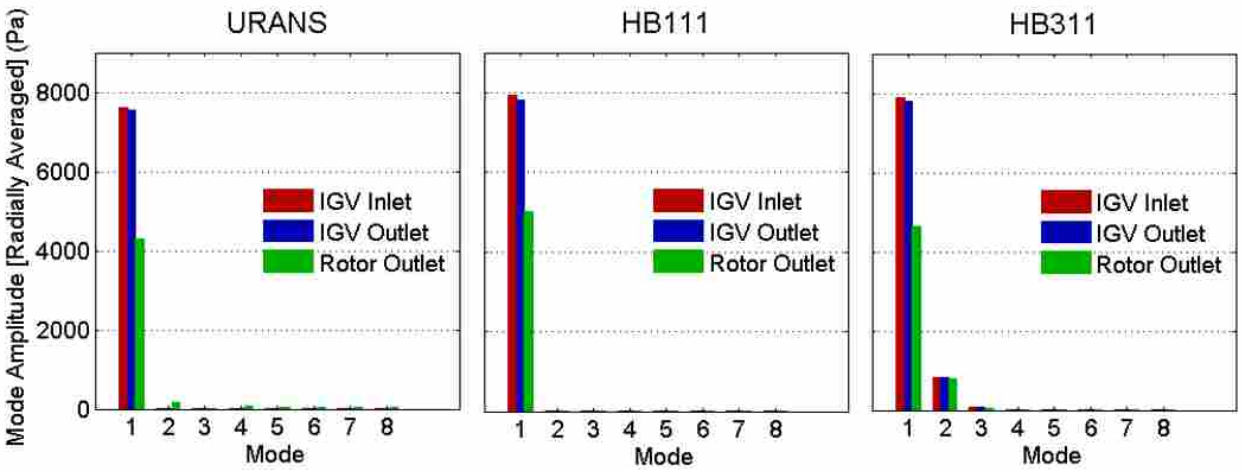

Figure 5.3: Modal amplitude results for three of the 15% 1-per-rev simulations. Left: URANS. Center: HB111. Right: HB311.

Figure 5.3 shows that the URANS simulations (left) have negligible to no content at the modes higher than 1. This is expected because this study used a 1-per-rev sinusoidal profile, and so most if not all of the distortion content was expected to be found in the mode 1 amplitude. For a case such as Peterson's [4] in which a more complex shape is used, the higher modes are necessary to capture the more complex profile, and so summing the modal content from more and more modes usually makes the HB results more closely match the URANS results. In the present study, however, noise was found in the higher harmonics when they were included (HB311 in Figure 5.3, right). This noise may be due to aliasing associated with the sinusoidal inlet profile or other sources discussed in section 5.2. The noise is absent when higher modes are not included (HB111 in Figure 5.3, center). When the modal amplitudes are summed for greater numbers of modes, more of the unexpected (noisy) content is included which causes the sum of the amplitudes (total amplitude) for HB511 to be less accurate than HB311, and the total amplitude of HB311 to be less accurate than HB111 as shown in tables 5.1 and 5.2.

The HB111 plot in Figure 5.3 (center) shows that when only one mode is specified at the inlet, then the amplitudes for mode 2 and higher are zero. This was also observed by Peterson (see Peterson's thesis: Figure 5.15 [4]) where an HB500 simulation calculated that the amplitudes for mode 6 and higher were zero. Although mode 2 results cannot be calculated if only one mode is included at the inlet, this does not necessarily mean that the mode 1 amplitude will be unaffected by specifying two or more modes in a blade row. In other words, an HB121 simulation may give more accurate results of mode 1 amplitude than an HB111 simulation. This is because higher order content introduced by a given blade row may shift to lower modes after interacting with another blade row.

In summary, HB simulations with multiple modes specified at the inlet resulted in modal content at higher harmonics that was absent for the URANS simulations. It is believed that this is due to sources of inconsistency such as the relationship between mesh and mode combination as well as possible flaws in the mesh that affect the abilities of the HB solver, and so in order to have a more consistent distortion metric for comparing HB to URANS, it was determined that the mode 1 amplitude should be used rather than the total amplitude. The mode 1 amplitude contains the majority of the distortion content for each of the 1-per-rev simulations, and so it is a representative metric for comparing distortion magnitude. For this reason, the mode 1 amplitude will be presented and discussed rather than the total amplitude.

5.4.2 HB Fourier Results: 15% 1-per-rev

Tables 5.3 through 5.6 show some of the modal amplitude and phase shift results for the 15% 1-per-rev simulations. Amplitudes and phase shifts are only included for the mode 1 amplitude in these tables because the URANS solver calculated that the second and higher modal amplitudes are all very small compared to the mode 1 amplitude. (See Figure 5.3, Left. The mode 2 amplitude was approximately 5% of the mode 1 amplitude, and all other modal amplitudes were no greater than 2% of the mode 1 amplitude.) Also, the differences between the distortion descriptor values of the HB simulations and the URANS simulations are relatively insignificant at the IGV inlet and outlet. All of these simulations gave mode 1 amplitude results with less than 5% difference from the URANS results at the IGV inlet and outlet, so only the values for the rotor outlet are included in these tables.

Table 5.3: Total pressure mode 1 amplitude (radially averaged).

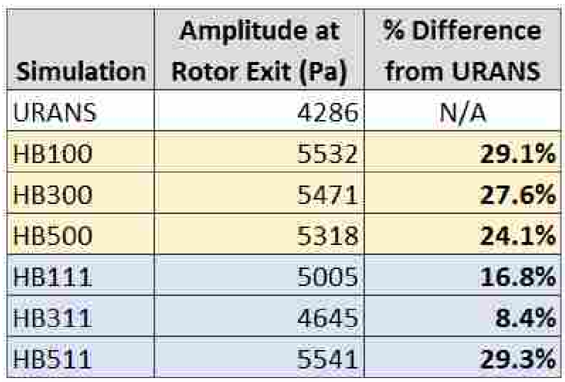

Simulation	Amplitude at Rotor Exit (Pa)	% Difference from URANS
URANS	4286	N/A
HB100	5532	**29.1%**
HB300	5471	**27.6%**
HB500	5318	**24.1%**
HB111	5005	**16.8%**
HB311	4645	**8.4%**
HB511	5541	**29.3%**

Table 5.4: Total temperature mode 1 amplitude (radially averaged).

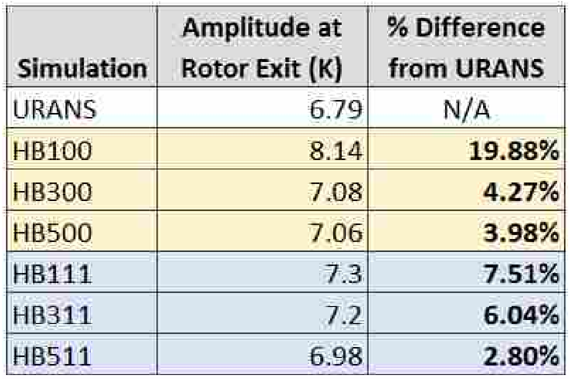

Simulation	Amplitude at Rotor Exit (K)	% Difference from URANS
URANS	6.79	N/A
HB100	8.14	**19.88%**
HB300	7.08	**4.27%**
HB500	7.06	**3.98%**
HB111	7.3	**7.51%**
HB311	7.2	**6.04%**
HB511	6.98	**2.80%**

The first trend apparent in the distortion descriptors in tables 5.3 through 5.5 is that in general, increasing the number of modes at the inlet boundary (the first number in the mode combination) increases the accuracy of the mode 1 amplitudes and phase shifts. Table 5.3 shows that the

Table 5.5: Total pressure mode 1
phase shift (radially averaged).

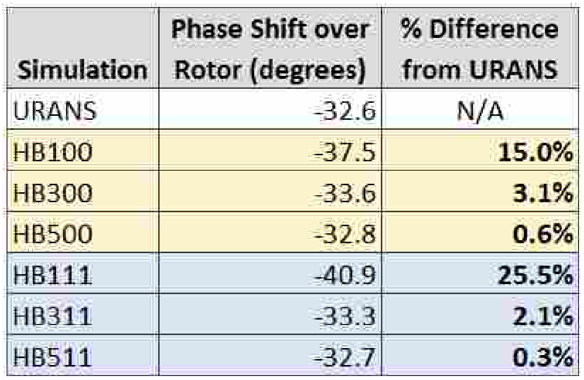

Simulation	Phase Shift over Rotor (degrees)	% Difference from URANS
URANS	-32.6	N/A
HB100	-37.5	**15.0%**
HB300	-33.6	**3.1%**
HB500	-32.8	**0.6%**
HB111	-40.9	**25.5%**
HB311	-33.3	**2.1%**
HB511	-32.7	**0.3%**

Table 5.6: Total temperature mode 1
phase shift (radially averaged).

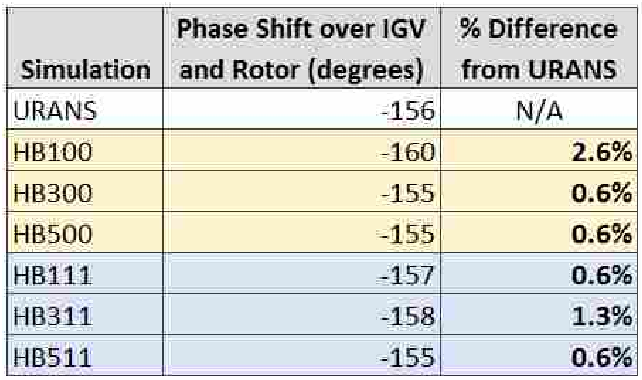

Simulation	Phase Shift over IGV and Rotor (degrees)	% Difference from URANS
URANS	-156	N/A
HB100	-160	**2.6%**
HB300	-155	**0.6%**
HB500	-155	**0.6%**
HB111	-157	**0.6%**
HB311	-158	**1.3%**
HB511	-155	**0.6%**

differences from the URANS results of the total pressure mode 1 amplitudes for HB100, HB300, and HB500 are 29.1%, 27.6%, and 24.1%, respectively (decreasing error). Table 5.4 shows that the total temperature mode 1 amplitude differences for the same three combinations are 19.9%, 4.27%, and 3.98%, respectively (decreasing error). Table 5.5 shows that for the mode 1 total pressure phase shifts, HB100 results in 15% difference from the URANS result, HB300 results in 3.1%, and HB500 results in 0.6% (decreasing error). In the each of the same three tables a similar decrease in error can be seen as HB combination is changed from HB111 to HB311 to HB511. (An exception to this trend is the HB511 mode 1 amplitude of total pressure in table 5.3 which shows an increase in error, but this is likely due to relatively poor convergence that was noticed for the

HB511 simulation.) The trend of increasing accuracy as the number of modes at the inlet boundary is increased suggests that although the inlet profile has a 1-per-rev sinusoidal shape, there are noticeable effects of higher order modes as the inlet profile interacts with the blade rows. These effects are more accurately captured by including more modes in the analysis at the inlet boundary.

Another trend that is noticed in the distortion descriptors in tables 5.3 through 5.5 is the significance of including one mode in each of the blade rows (i.e. HB#11) versus including no modes in the blade rows (i.e. HB#00). In the total pressure mode 1 amplitudes in table 5.3, the HB100 simulation gives 29.1% difference from the URANS results while the HB111 simulation gives 16.8%, and the HB300 simulation gives 27.6% while the HB311 simulation gives 8.4%. Both of these comparisons illustrate a significant increase in accuracy by including one mode rather than zero modes in each blade row. This trend is seen in other distortion descriptors by comparing the results for HB100 to HB111, HB300 to HB311, and HB500 to HB511 in tables 5.3 through 5.5. There are a few cases in which adding modes in the blade rows increases the difference from the URANS results, such as total pressure mode 1 amplitude for the HB511 simulation and total pressure phase shift for HB111, but more often than not, the results for each distortion descriptor become more accurate as modes are included in the blade rows. This suggests that the blade rows have an appreciable amount of 1-per-rev effects on the flow.

Table 5.6 does not show either of the above trends discussed for tables 5.3 through 5.5. The total temperature phase shift values for each of the HB simulations shown do not tend to increase in accuracy as more modes are included, but they are all very close to the value obtained with the URANS simulation. This can be seen in table 5.6 where the URANS simulation has a phase shift of -156°, and all of the HB simulations give values between -155° and -160°. This corresponds to a maximum difference below 3% which is considered very accurate in this study. This suggests that the total temperature phase shift is not significantly affected by mode combination for a simulation with a 15% 1-per-rev sinusoidal inlet profile. The fact that all simulated mode combinations predicted total temperature phase shift with great accuracy is encouraging because this allows designers to include less modes allowing for more efficient computations if their sole goal is to accurately predict total temperature phase shift.

HB Fourier Results: 15% 1-per-rev: Multiple Modes in a Blade Row

Simulations were also performed with multiple modes in one or both of the blade rows (for example HB121 and HB122). The results of mode 1 amplitude of total pressure for these simulations are shown in table 5.7. In table 5.7, the cells containing the % difference values are colored according to their magnitude in order to show the relative amount of difference for each case. The greatest difference is shown in red, and the lowest difference is shown in green.

Table 5.7: Total pressure mode 1 amplitude
(radially averaged). 15% 1-per-rev.

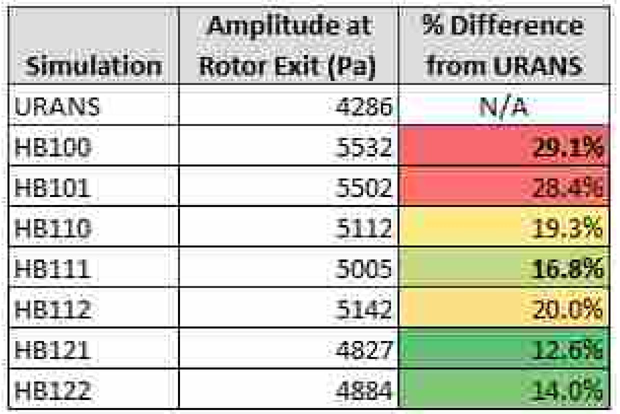

Simulation	Amplitude at Rotor Exit (Pa)	% Difference from URANS
URANS	4286	N/A
HB100	5532	29.1%
HB101	5502	28.4%
HB110	5112	19.3%
HB111	5005	16.8%
HB112	5142	20.0%
HB121	4827	12.6%
HB122	4884	14.0%

The first trend observed in table 5.7 is that the HB100 and HB101 simulations have about the same red color (corresponding to approximately 29%). The HB110, HB111, and HB112 simulations by contrast all have a yellow to yellow green color (about 17 to 20%). Finally, the HB121 and HB122 simulations both have a saturated green (about 13 to 14%). This highlights the minimal effects of the number of modes specified in the rotor row (3rd number in HB mode combination). Recall from the introduction that the number of modes specified in a row determines the amount of solution information to pass on to other blade rows. The number of modes specified in any one blade row won't directly affect the amount of distortion in that blade row, and so in this case, including zero or one or two modes in the rotor blade row has minimal effect on the amplitude at the rotor exit. The differences that do exist are likely due to normal variability or noise in the simulations.

In contrast with the rotor blade row (3rd number in HB mode combination), the effect of increasing the number of modes in the IGV blade row (2nd number in HB mode combination) can be seen in table 5.7. Having one mode in the IGV row instead of zero modes brings the error down from about 29% to as low as 16.8%. Including two modes in the IGV row instead of one brings the error even further down (as low as 12.6%). Although this is an improvement, this increase in accuracy comes with an increase in the computational expense associated with including an extra mode. (For a given number of processors, the addition of one mode in a blade row can slow down iteration speed by a factor of up to two or three. A more thorough computational cost comparison is included in section 5.6.) For this reason, it is recommended that only one mode be included in the IGV row for simulations involving sinusoidal inlet total pressure distortion if the priority is accurately predicting distortion transfer and generation. It is also recommended that one mode be included in the rotor blade row because this seems to improve convergence, and it gives more consistent results than simulations with zero modes in the rotor blade row.

From this analysis of distortion results for a 15% 1-per-rev inlet profile, HB311 gives the most consistently accurate distortion descriptor results. It sufficiently captures the inlet profile by using three modes at the inlet boundary, and then it captures interactions of the IGV blade row with the 1-per-rev component of the applied distortion. Including one mode in the rotor row (location 3) improves the likelihood of convergence and captures any 1-per-rev unsteady effects of the rotor on the IGV. Therefore if the goal is to quantify distortion transfer and generation for an IGV-rotor configuration, then HB311 is the recommended mode combination for a 15% sinusoidal 1-per-rev simulation.

5.4.3 HB Fourier Results: Comparing 10%, 15%, and 20% 1-per-rev

The 10% 1-per-rev simulations and the 20% simulations have some trends that are similar to the 15% simulations as well as some trends that are different. To help illustrate some of the trends, Figure 5.4 and Figure 5.5 show how the HB111, HB311, and HB312 simulations compare in their ability to match the URANS simulations for the three different magnitudes of distortion. The metrics that are compared are the mode 1 amplitude of total pressure (Figure 5.4) and total temperature (Figure 5.5).

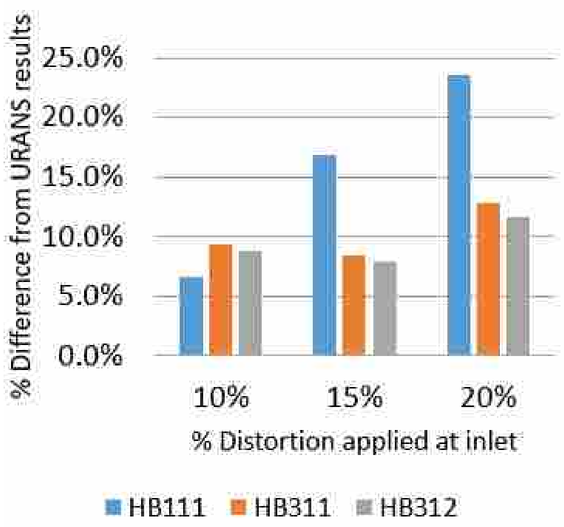

Figure 5.4: Total pressure mode 1 amplitudes for 1-per-rev simulations. % Difference from URANS results.

One observation from Figure 5.4 and Figure 5.5 is that keeping the mode combination the same while increasing the amount of distortion at the inlet from 15% to 20% tends to increase the difference between the HB and URANS results (decreasing accuracy). This is shown in Figure 5.4 where for the HB111 simulations, the difference in the total pressure mode 1 amplitude increases from 16.8% for the 15% distortion simulation to 23.5% for the 20% simulation. For the HB311 simulations, the difference increases from 8.4% to 12.8%. A similar decreases in accuracy can be seen in Figure 5.5 where the difference for the HB111 simulations increases from 7.5% to 17.4% and the the difference for the HB311 simulations increases from 6.0% to 10.0%. The decrease

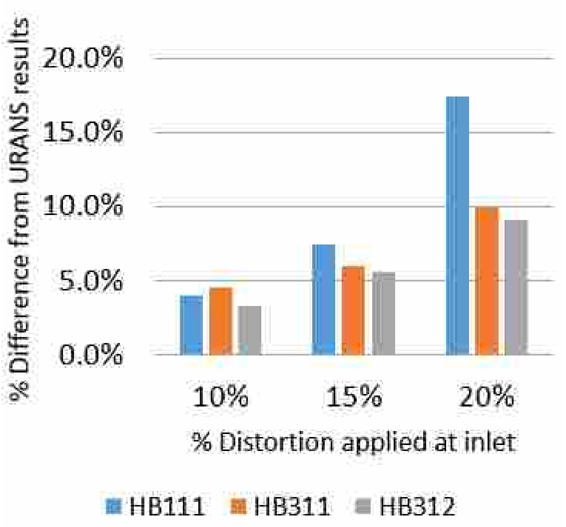

Figure 5.5: Total temperature mode 1 amplitudes for 1-per-rev simulations. % Difference from URANS results.

in accuracy for the 20% distortion simulations confirms that more non-linear interactions occur at greater distortion levels, and the effects of these non-linear interactions are difficult for the solver to predict to the same level of accuracy as the 15% simulations.

For both the 15% simulations and the 20% simulations, it is observed that the number of modes at the inlet has the greatest impact on the accuracy of the distortion descriptors. This is evident in Figure 5.4 and Figure 5.5. Changing the number of modes at the inlet from one (blue bar) to three (orange bar) increases the accuracy substantially for the 15% and 20% simulations. Then, adding another mode in the rotor region (gray bar) increases the accuracy even more, but by a relatively small amount. As hypothesized in section 5.4.2, the trend of increasing accuracy as the number of modes at the inlet boundary is increased suggests that although the inlet profile has a 1-per-rev sinusoidal shape, there are noticeable effects of higher order modes as the inlet profile interacts with the blade rows. These effects are more accurately captured by including more modes in the analysis at the inlet boundary and therefore passing more information from the inlet profile on to the blade rows. Based on these findings, similar to the 15% simulations, HB311 is recommended as the mode combination for a 20% sinusoidal 1-per-rev profile if the goal is to accurately predict distortion transfer and generation.

Distortion results for the 10% 1-per-rev simulations are different from the results of the 15% and 20% simulations. For the 10% profile, all of the simulated combinations resulted in phase shifts and amplitudes that had close to 10% difference from the URANS results or less. Many of the distortion descriptor values result in less than 5% difference (see the 10% bars in Figure 5.5). No mode combination proved to give significantly better or worse results than another. This suggests that a 10% inlet distortion profile results in relatively small amounts of distortion transfer and generation that can be accurately predicted even if very little modal content is included in the calculations. For this reason, if the goal is to accurately predict distortion transfer and generation, HB111 is recommended for a simulation with a 10% sinusoidal 1-per-rev profile rather than HB311 because HB111 solves significantly faster than HB311 while still giving accurate distortion amplitude and phase shift results.

The general observation that including more modes improves accuracy only for simulations with greater magnitudes of distortion confirms that the greater magnitudes of distortion cause more non-linear interaction. An HB111 simulation essentially allows the inlet distortion profile, the IGV, and the rotor to interact, but then it only keeps the first mode response. It results in the higher modes being zero. This is sufficient for small amounts of sinusoidal inlet distortion such as 10% or less because the corresponding effect on distortion transfer and generation is very small. For the 15% and 20% profiles, however, the effects on distortion transfer and generation are significant. For these higher amounts of applied inlet distortion, non-linear interactions shift more energy to higher modes, and so HB311 is necessary to achieve acceptable accuracy. In general, simulations with greater distortion require more modal content to achieve accurate results.

5.4.4 HB Fourier Results: 2-per-rev Simulations

In addition to the 1-per-rev sinusoidal distortion profiles, simulations were performed for 2-per-rev profiles with 10%, 15%, and 20% distortion. The URANS solver calculated that the majority of the modal content is in the mode 2 amplitude for these simulations, which is expected for a sinusoidal 2-per-rev profile. The odd modal amplitudes were each approximately zero, and the even modal amplitudes other than 2 were negligible compared to the mode 2 amplitude, so only the mode 2 amplitude and phase shift results were examined for the 2-per-rev simulations. Moreover, it was necessary to specify at least two modes at the inlet in order to capture the 2-per-rev profiles of distortion. A selection of mode 2 amplitude results for 2-per-rev simulations is shown in Figures 5.6 and 5.7. HB211, HB311, and HB400 are presented because these combinations are representative of general trends observed in the 2-per-rev results. The HB411 simulation was expected to provide favorable results for 2-per-rev simulations, but it was unable to converge, and so it is not included in Figure 5.6.

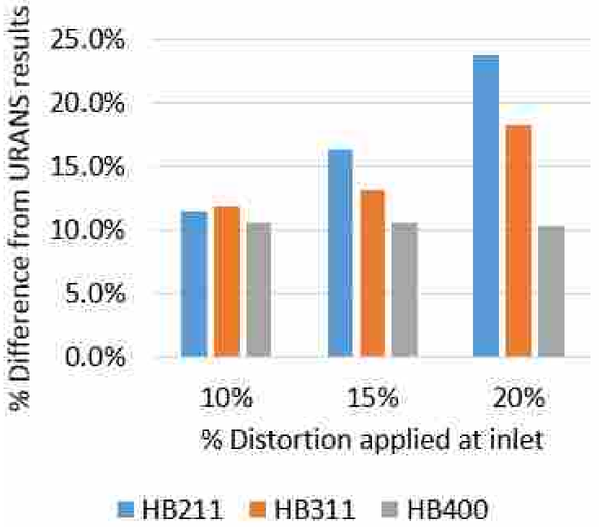

Figure 5.6: Total pressure mode 2 amplitudes for 2-per-rev simulations. % Difference from URANS results.

The results of the 2-per-rev simulations had a few similarities to the results of the 1-per-rev simulations. In many cases, keeping the mode combination the same while increasing the amount of distortion at the inlet tended to increase the difference between the HB and URANS distortion results. This is shown for HB211 and HB311 in Figure 5.6. For the 10% profile, the total pressure mode 2 amplitude for HB211 had 11.5% difference at the rotor outlet, whereas for the 15% profile it had 16.4% difference, and for the 20% profile it had 23.8% difference. The HB311 simulation had a similar increase in error as the magnitude of inlet distortion increased. (12% to 13.5%

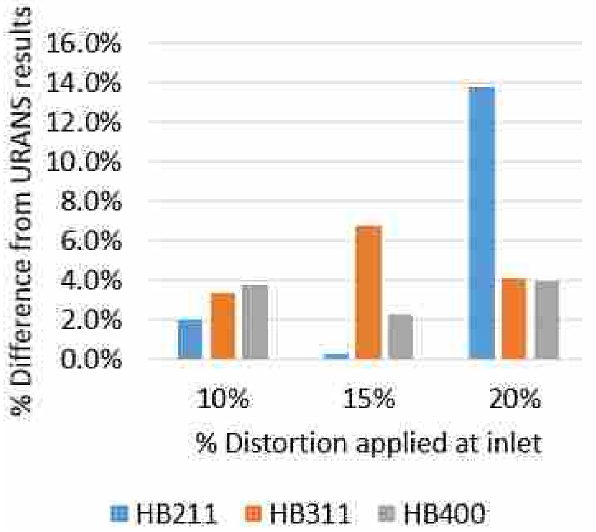

Figure 5.7: Total temperature mode 2 amplitudes for 2-per-rev simulations. % Difference from URANS results.

to 18%.) As was suggested in section 5.4.3, this is likely due to greater non-linear interactions occurring for greater levels of distortion. The increased non-linear interactions are more difficult for the solver to predict, resulting in decreased accuracy if more modes are not included in the simulation.

There were several cases of 2-per-rev simulations in which increasing the amount of inlet distortion did not increase the error. The total pressure results for HB400 (gray bars in Figure 5.6) showed no increase but rather remained near 10% difference for all three profiles. This suggests that for the given setup with these 2-per-rev simulations, the HB400 mode combination was sufficient to accurately capture the total pressure distortion transfer for all three levels of inlet distortion.

For the total temperature mode 2 amplitudes, increasing the amount of inlet distortion did not always increase the error. This is shown in Figure 5.7. These mode 2 amplitudes were predicted to within 4% of the URANS results in all cases except for the HB311 with the 15% inlet profile (7% error) and the HB211 with the 20% inlet profile (14% difference). These results suggest that total temperature distortion generation for a 2-per-rev applied inlet distortion profile is more complex to predict than for a 1-per-rev inlet profile. (See the stronger correlation for the 1-per-rev results in Figure 5.5.) The reason behind this observation may also be the relationship between mesh and mode combination mentioned in section 5.2. It may also be due to the difference in boundary condition treatment (RBCs vs NRBCs) discussed in section 5.3. It is important to note, however, that although the trend in Figure 5.7 does not follow the trend in Figure 5.5, almost all of the results in Figure 5.7 are within 7% of the URANS results which is considered fairly accurate.

Almost all the simulated combinations gave close to 10% difference or less from the URANS results for each distortion descriptor for the 2-per-rev 10% simulations, and so HB211 is recommended for a 2-per-rev 10% profile if the priority is to accurately predict distortion transfer and generation. HB211 gave fair distortion results for the 2-per-rev 15% and 20% simulations, but the best results for 15% and 20% were achieved with HB400 (Presented in Figure 5.6). The HB411 simulations did not converge for this study (due to unknown causes discussed in section 5.2), but if HB411 could be brought to converge, it would likely be the ideal mode combination for 2-per-rev sinusoidal profiles with distortion of 15% or 20%. The fact that simulations with greater distortion required more modal content to achieve accurate results is further evidence that greater distortion correlates with more non-linear interaction.

5.5 Overall Performance Measures

Another metric used for evaluation of the HB simulations was the overall performance of the compressor. In some cases, the priority in the design of a fan or compressor may be to more accurately predict performance measures than to accurately predict distortion transfer and generation. Recommendations of mode combinations for this design priority may differ from previous recommendations based on how many modes are deemed necessary to efficiently and accurately predict performance. To this end, three overall performance measures are presented in this section for each simulation. These measures are efficiency, total pressure ratio, and corrected mass flow rate. Differences are presented for the HB simulations with respect to the URANS simulations. The values and percent differences of efficiency, total pressure ratio, and mass flow rate for the 20% distortion simulations are shown in table 5.8. The overall performance data is shown for the 20% distortion simulations because the 15% simulations and the 10% simulations each showed almost no variation in performance. Effects on performance were only noticed for the 20% simulations.

In table 5.8, all of the simulations give less than 1% difference from the URANS results for efficiency, pressure ratio, and mass flow rate. Efficiency shows no trend, but pressure ratio is shown to be slightly more accurately predicted when HB311 or HB312 is used rather than the HB1## combinations (less than 0.1% vs approximately 0.6%). Mass flow was also more accurately predicted by HB311 and HB312 than the HB1## combinations (0.36% and 0.24% vs 0.43% to 0.79%). The fact that all of these performance measures were calculated to have very low differences suggests that although mode combination is very important for capturing distortion transfer and generation, the effects of that distortion on the overall performance of a compressor stage can be captured very accurately with even the simplest of HB simulations. For this reason, if the goal is only to predict performance accurately, then it is recommended to use HB111 or HB110 because these are the most computationally inexpensive but they still predict performance to within 1% error.

Table 5.8: Overall performance measures for the mode combinations used in the 20% simulations

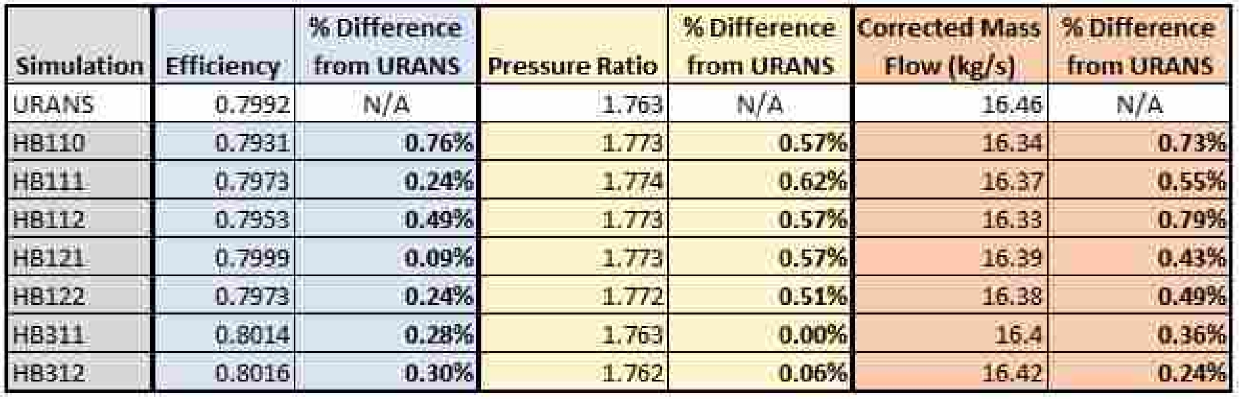

Simulation	Efficiency	% Difference from URANS	Pressure Ratio	% Difference from URANS	Corrected Mass Flow (kg/s)	% Difference from URANS
URANS	0.7992	N/A	1.763	N/A	16.46	N/A
HB110	0.7931	**0.76%**	1.773	**0.57%**	16.34	**0.73%**
HB111	0.7973	**0.24%**	1.774	**0.62%**	16.37	**0.55%**
HB112	0.7953	**0.49%**	1.773	**0.57%**	16.33	**0.79%**
HB121	0.7999	**0.09%**	1.773	**0.57%**	16.39	**0.43%**
HB122	0.7973	**0.24%**	1.772	**0.51%**	16.38	**0.49%**
HB311	0.8014	**0.28%**	1.763	**0.00%**	16.4	**0.36%**
HB312	0.8016	**0.30%**	1.762	**0.06%**	16.42	**0.24%**

The effect of distortion magnitude on the accuracy of pressure ratio and mass flow is further analyzed by plotting pressure ratio versus corrected mass flow rate for the 1-per-rev simulations (Figure 5.8). The markers on the plot shows the results of various mode combinations as well as the

URANS simulations. The cluster of the 10% simulations is the most tightly packed, and the cluster of 20% simulations is the most scattered. This is further evidence that greater distortion correlates with more non-linear interaction. The greater non-linear interaction causes greater variance in the Harmonic Balance results. As more HB modes are included, the non-linear effects are better captured, and the HB simulations more closely match the URANS simulations.

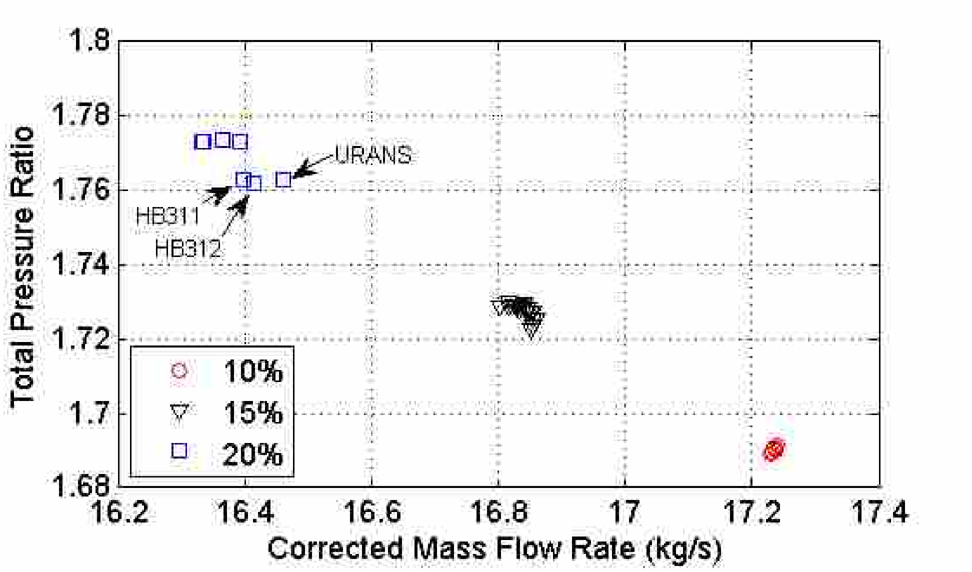

Figure 5.8: Pressure ratio versus corrected mass flow rate for the 1-per-rev simulations. Note that the simulations with the 10% profile all have very similar pressure ratio and corrected mass flow results no matter what mode combination is used. The 15% results are also very close, but the 20% results have a slight spread.

5.6 Computational Cost Comparison

Computational cost must be considered when running turbomachinery simulations because poor computational decisions can dramatically increase solve time without increasing accuracy. This is especially applicable for Harmonic Balance simulations because the amount of calculations that are performed per iteration correlates with the numbers of modes that are specified for the inlet and the blade rows. Adding modes has the same effect on solve time as increasing the mesh size by a certain amount. This is shown in Equation 5.2 (see [4]) where $N_{effective}$ is the predicted effective number of cells in the domain, BR is the number of blade rows, N_i is the number of cells in a given blade row, and TL_i is the number of time levels associated with that blade row. In a simple case with no inlet distortion profile, the number of time levels in a blade row would be determined in the following manner: If one mode is specified in the blade row, then there are three time levels (-1, 0, and 1). If two modes are specified, then there are five time levels (-2, -1, 0, 1, and 2), and so on. When inlet distortion is included, the numbers of time levels in the blade rows are computed in a more complex manner that depends on the number of modes specified at the inlet boundary. STAR-CCM+ computes the numbers of time levels in the blade rows internally. In general, specifying more modes increases the numbers of time levels exponentially, and so Equation 5.2 predicts that as more modes are specified, the effective mesh size increases, and therefore solve time is expected to increase in like manner.

$$N_{effective} = \sum_{i=1}^{BR} N_i \cdot TL_i \tag{5.2}$$

Results of a computational cost analysis are presented in Table 5.9. These results help to determine the relative time savings of the HB simulations versus the URANS simulations. The number of iterations per processor-hour are presented for each simulation as well as the total solve time on 256 processors. The total solve time takes into account the approximate number of iterations executed for each simulation.

The computational cost results shown in table 5.9 reveal the dramatic effect that increasing the number of modes in a simulation has on solve time. The total solve time of the HB511 simulations is about 84% that of the URANS simulations, and the HB312 simulations take about half as long as the URANS simulations, and so although a 16% reduction and a 50% reduction in solve time are good, HB511 and HB312 are not likely to be the best choice for minimizing computational costs unless the gains in accuracy are deemed necessary. HB311, by contrast, takes only 15.1 hours, which is about one-sixth the time of the URANS simulations. This is a significant decrease in time, and so HB311 is recommended as a good combination for minimizing computational costs

Table 5.9: Computational cost comparison for several of the mode combinations simulated.

Type of Simulation	Iterations/ (processor*hr)	Iterations	Total Solve Time on 256 Processors (hr)
URANS	3.41	86400	99.0
HB100	44.25	10000	0.9
HB300	25.58	10000	1.5
HB500	8.96	10000	4.4
HB111	11.74	10000	3.3
HB311	2.60	10000	15.1
HB312	0.81	10000	48.2
HB511	0.47	10000	83.2

while also providing sufficient accuracy of distortion transfer and generation as described in section 5.4.2. If the goal is to predict performance accurately, and distortion transfer and generation are not prioritized, then it is recommended to use HB111 or HB110 rather than HB311 to save even more on computational cost. This is because all the simulated mode combinations predicted performance to within 1% error as shown in table 5.8.

5.7 Comparison to Previous Harmonic Balance Research

In this section, findings from Peterson's HB research [4] with PBS rotor 4 are compared to findings from the present HB study with NASA rotor 37. In general, the two studies had very similar conclusions. Both showed that the HB solver had lower computational costs than the URANS solver. Both studies also showed that including modes at the inlet boundary was more important than including modes in the blade rows for calculating distortion transfer and generation. A few conclusions that did not agree between the two studies will be discussed. These discrepancies were likely due to the differences in inlet profiles between the two studies and the difference in the geometry and configuration. Peterson's HB simulations used a 90-degree sector of total pressure inlet distortion whereas the present HB study used sinusoidal profiles. Also, Peterson's configuration consisted of a rotor followed by a stator, whereas the present study consisted of an IGV followed by a rotor.

Both Peterson's study and the present study showed that the HB solver had significantly lower computational requirements and physical time requirements than the URANS solver. In Peterson's study, the total processor hours required for HB was five to seven times less than the amount required for the URANS simulation. Similarly, the recommended HB mode combination in the present study (HB311) resulted in a simulation that converged in one-sixth the time required by the URANS solver.

Another finding that both studies agreed upon was that including modes at the inlet boundary was more important than including modes in the blade rows. The more modes used to capture the inlet distortion profile, the more accurate the distortion transfer and generation predictions were. Inclusion of modes in the blade rows, on the other hand, had a relatively small effect on the accuracy of the distortion transfer and generation predictions. Peterson found the inclusion of modes in the blade rows to have no perceivable effect; however, the present study found two favorable effects of including modes in the blade rows. First, the simulations tended to achieve better convergence (more regular residuals with lower magnitudes) if each blade row had one mode than if either of the blade rows had zero modes. Second, there was a noticeable increase in accuracy by including one mode in each blade row rather than zero. For both Peterson's study and this study, including more than one mode in a blade row did not significantly increase the accuracy of the distortion transfer and generation predictions. This was because the majority of the distortion content imparted on the flow by the blade rows was of the 1-per-rev type and thus could be sufficiently captured with only one mode.

Both Peterson's study and this study found the HB solver to be excellent at capturing fan performance with distorted inlet conditions, but the two studies disagree on the effect that the modes in the blade rows have on performance. Peterson showed that including modes in the blade rows helped his simulations to more accurately predict performance, but the present study found that all the simulated HB mode combinations calculated the efficiency and pressure ratio values to within 1% of the values calculated by the URANS solver. Including more modes at the inlet boundary gave a slight increase in accuracy (0.1% vs 0.5% error), but including modes in the blade rows showed no increase in accuracy of the efficiency and pressure ratio values for this study. The discrepancy may be explained by the more complex geometry and inlet profile used in Peterson's study. This greater complexity necessitated that modes be specified in the blade rows to achieve accurate performance results.

Overall mode combination recommendations made by the two studies had some differences, but these differences were likely due to the different inlet distortion profiles used and the difference in the blade configurations. Peterson stated that the optimal HB mode combination for the 90-degree sector distortion profile he applied to the rotor 4 geometry is HB321. He reasoned that this was a good balance between computational resources and accuracy for both performance and distortion transfer and generation. The recommendation for the present study with a 1-per-rev 15% sinusoidal inlet profile applied to the rotor 37 geometry is HB111 if predicting performance is the greatest priority, but it is HB311 if calculating distortion transfer and generation is the greater priority. The fact that less modes were deemed necessary for the present study is partly due to the fact that the inlet profile of this study was sinusoidal. The HB solver uses Fourier series to construct the solution, and therefore it is expected to handle sinusoidal shapes very well. By contrast, the non-sinusoidal nature of the sector (which had abrupt transitions from clean to distorted flow) requires more Fourier terms to capture its shape, and so more modes are recommended. The more complex an inlet profile shape, the more modes that are necessary to recreate that shape.

Another reason why Peterson's recommendation differs from that of the present study is the difference in the configuration of blades for each study. Because Peterson's configuration had the rotor upstream of the stator, it was recommended to place two modes in the that blade row so that sufficient effects of the rotor could be passed downstream to interact with the stator. In the present study, however, the rotor was the final blade row in the configuration, and so only the upstream effects of the rotor could be impacted by adding more modes to the rotor. The upstream effects of the rotor blades interacting with the IGV blades were sufficiently captured with one mode in the rotor blade row, and the solution within the rotor blade row could not be directly affected by adding more modes in the rotor blade row. Were the present study to be repeated with another stator blade row downstream of the rotor blade row, then it is possible that greater accuracy in distortion transfer and generation and performance would be achieved by including two modes in the rotor blade row.

CHAPTER 6. CONCLUSIONS

This chapter describes the conclusions that are made from this research. Conclusions are first given for the study with Rotor 4, and then conclusions are given for the study with Rotor 37.

6.1 Conclusions of Rotor 4 Study

Flow physics and mechanisms of distortion transfer and generation were investigated in a single stage transonic fan by analyzing unsteady RANS simulations at choke, design, and near stall operating conditions at 10%, 30%, 50%, 70%, and 90% span. Moving from the design to near-stall operating condition was shown to increase total pressure distortion transfer and total temperature distortion generation. The distortion transfer near the hub was independent of operating point whereas distortion transfer near the tip greatly varied with operating condition.

It was shown that inlet total pressure distortion induces swirl at the inlet of the fan rotor. This resulted in a counter-swirl flow region at one of the inlet total pressure distortion sector boundaries and a co-swirl flow region at the other boundary. Counter-swirl increases the incidence angle of the flow on the rotor blade which increases the amount of power. Co-swirl decreases the rotor incidence angle and the rotor blade generates less power. Additional power increases the total pressure magnitude and reduced power decreases the rotor total pressure. The regions of less power result in lower total temperature and the regions of greater power result in higher total temperature.

Induced co- and counter-swirl were enhanced near-stall when compared to design. In contrast, there was almost no difference in pressure-induced swirl between the design and choke operating points. Moving from near-stall to design to choke resulted in increased magnitudes of the valleys in total pressure and total temperature (those due to co-swirl) and decreased magnitudes of the main peaks (those due to counter-swirl). Local power variations through the rotor correlated with total pressure and total temperature traverses. Power differences between operating points were very small at the hub and relatively large at the tip.

6.2 Conclusions of Rotor 37 Study

The ability of the Harmonic Balance solver in STAR-CCM+ to capture distortion transfer and generation for various inlet distortion profiles was investigated in a single stage compressor. The conclusions that follow are based on the rotor 37 geometry with the applied distortion profiles. These conclusions may prove true for other rotor geometries and other distortion profiles (especially those similar to the ones in this study), but caution must be taken when interpreting these conclusions generally.

Non-reflecting boundary conditions associated with the HB solver allowed applied properties at some boundaries to vary while reflecting boundary conditions associated with the URANS solver strictly held the properties at the boundaries to be their specified values. This resulted in the HB simulations having slightly higher amounts of inlet distortion than the applied amount. For an HB simulation, it is recommended to provide appropriate offsets in the applied distortion profile at the inlet to account for the differences introduced by the HB solver. It is also recommended for both the HB and the URANS simulations to extend the domain far enough away from the blades so that the different methods that the solvers use to handle boundary conditions will not significantly interfere with the resolving of the wakes from the blades.

Recommendations of mode combinations were made based on the accuracy of the calculated distortion descriptors. The recommended mode combinations differed for varying levels of applied inlet distortion. For the 15% and 20% simulations, the number of modes at the IGV inlet boundary had the greatest effect on the accuracy of the distortion descriptors. It is recommended that HB311 be used for simulations with 15% and 20% 1-per-rev sinusoidal distortion profiles to achieve the most accurate distortion descriptors. For the 10% 1-per-rev simulations, however, all the mode combinations give very accurate distortion results, and so HB111 is recommended for a simulation with a 10% 1-per-rev profile because HB111 solves significantly faster than HB311 while still giving accurate results. The fact that including more modes improves accuracy only for the simulations with greater magnitudes of distortion suggests that the greater magnitudes of distortion cause more non-linear interaction which shifts the energy to the higher modes. The 10% simulations resulted in very small amounts of distortion transfer and generation that could accurately be predicted even if very little modal content was included in the calculations.

Recommendations of mode combination were also made based on the accuracy of three calculated performance measures. Efficiency, pressure ratio, and mass flow results showed little dependence on mode combination. As magnitude of distortion was increased, the spread of the results for the different HB simulations increased slightly. This is further evidence that greater distortion causes more nonlinear interaction, but all of the simulations achieved very accurate results (less than 1% error) for all of the calculated overall performance measures. It was recommended that the HB111 or HB110 be used if the goal is only to predict performance accurately because these are very computationally inexpensive, but they still predict performance to within 1% error.

Some similarities and differences exist between 1-per-rev simulations and 2-per-rev simulations. For both the 1-per-rev and 2-per-rev simulations, keeping the mode combination the same while increasing the amount of distortion at the inlet tends to increase the difference between the HB distortion results and the URANS distortion results for total pressure. To compensate for this, higher mode combinations are recommended for higher amounts of distortion. For 1-per-rev simulations, the mode 1 amplitude contains the majority of the distortion content, and so reasonable results can sometimes be achieved with only one mode at the inlet boundary. By contrast, for 2-per-rev simulations at least two modes must be included at the inlet boundary.

A computational cost comparison for the simulated mode combinations reveals that total solve time increases dramatically as the numbers of modes increases. HB311 requires about one-sixth the computational resources of a URANS simulation, making it a good option to minimize computational cost while maximizing accuracy.

Comparisons were made between the findings of this study and the conclusions of a previous Harmonic Balance study. Both studies found that distortion transfer and generation and overall performance can be accurately predicted by the HB solver with much less computational resources than a URANS solver. Differences in mode combination recommendations made by the two studies were determined to be due to the different configurations used (IGV-rotor vs rotor-stator) and the applied inlet total pressure profile (90-degree sector vs sinusoidal 1-per-rev).

6.3 Future Work

Directions for future work that would add greater insight to distortion flow physics are the following:

1. Comparisons of distortion transfer and generation were made between multiple operating points at several radial locations; however, it would be instructive to also run clean inlet (undistorted) URANS simulations of rotor 4 at all three operating points and compare these to the distorted results. With clean inlet simulation results, it would be possible to determine how much of the variability that was seen is due to operating point alone, and how much of it is due to distortion.

2. All of the results in this thesis were from simulations at 100% speed (the design rotation rate). Conclusions are likely to be different for other speed lines such as 90% speed or 80% speed because for lower rotational speeds, the effects of shocks will be lessened or absent. Fans and compressors often operate at multiple rotational speeds during a single flight, and so it would be valuable to examine how the distortion flow physics change with rotational speed.

3. In this thesis, it was hypothesized that the sharpness of the transition from high to low total pressure was a primary factor in the amount of swirl induced at those locations as well as the amount of phase lag between the total pressure profile and the total temperature profile. Other factors may include the magnitude and extent of applied distortion. It is recommended

for future research that profiles of varying transition sharpness be simulated with rotor 4. Magnitude and extent may also be varied. This could lead to prediction models for the expected amounts of swirl and phase lag, both as functions of transition sharpness, distortion magnitude, and distortion extent.

4. The simulations that were run for this thesis all used the Spalart-Allmaras turbulence model. For Harmonic Balance simulations, Spalart-Allmaras is the standard turbulence model in STAR-CCM+, but for unsteady RANS simulations the recommended turbulence model is the SST k-omega model. It would be valuable to see how much the results of this thesis would change if the SST k-omega turbulence model were used. In general, for any future unsteady RANS simulations, it is recommended to use the SST k-omega model to achieve greater accuracy.

REFERENCES

[1] Gorrell, S. E., Yao, J., and Wadia, A. R., 2008. “High Fidelity URANS Analysis of Swirl Generation and Fan Response to Inlet Distortion.” AIAA Paper 2008-4985. 2, 13, 48, 64

[2] Yao, J., Gorrell, S. E., and Wadia, A. R., 2010. “High-Fidelity Numerical Analysis of Per-Rev-Type Inlet Distortion Transfer in Multistage Fans–Part I: Simulations With Selected Blade Rows.” *Journal of Turbomachinery,* **132**(041014), pp. 1–10. 2, 12, 63, 75

[3] Yao, J., Gorrell, S. E., and Wadia, A. R., 2010. “High-Fidelity Numerical Analysis of Per-Rev-Type Inlet Distortion Transfer in Multistage Fans–Part II: Entire Component Simulation and Investigation.” *Journal of Turbomachinery,* **132**(041014), pp. 1–17. 2, 12, 63, 75

[4] Peterson, M. W., 2016. “Implementations of Fourier Methods in CFD to Analyze Distortion Transfer and Generation Through a Transonic Fan.” M.S. Thesis, Brigham Young University. 4, 5, 6, 17, 23, 25, 28, 35, 41, 71, 76, 78, 79, 92, 94

[5] Peterson, M. W., Gorrell, S. E., List, M. G., and Custer, C., 2016. “Implementation of Fourier Methods in CFD to Analyze Distortion Transfer and Generation Through a Transonic Fan.” AIAA Paper 2016-4746. 5, 17

[6] Cousins, W., 2004. History, Philosophy, Physics, and Future Directions of Aircraft Propulsion System/Inlet Integration ASME Paper GT-2004-54210. 7, 17

[7] Nessler, C. A., Copenhaver, W. W., and List, M. G., 2013. “Serpentine Diffuser Performance with Emphasis on Future Introduction to a Transonic Fan.” AIAA Paper 2013-0219. 7

[8] Pearson, H., and McKenzie, A. B., 1959. “Wakes in Axial Compressors.” *Journal of the Royal Aeronautical Society,* **63**, July, pp. 415–416. 10

[9] Reid, C., 1969. “The Response of Axial Flow Compressors to Intake Flow Distortion.” *ASME*(69–GT–29). 10

[10] Cousins, W. T., and Davis, M. W., 2011. “Evaluating Complex Inlet Distortion with a Parallel Compressor Model: Part 1-Concepts, Theory, Extensions, and Limitations.” ASME Paper GT2011-45067. 10

[11] Davis, M. W., and Cousins, W. T., 2011. “Evaluating Complex Inlet Distortion with a Parallel Compressor Model: Part 2-Applications to Complex Patterns.” ASME Paper GT2011-45068. 10

[12] Calogeras, J. E., Mehalic, C. M., and Burstadt, P. L., 1971. Experimental Investigation of the Effect of Screen-Induced-Total-Pressure Distortion on Turbojet Stall Margin Technical Memorandum NASA TM X-2239, NASA Lewis Research Center, Cleveland, OH. 11, 26

[13] Rademakers, R. P. M., Bindl, S., and Niehaus, R., 2016. "Effects of Flow Distortions as They Occur in S-Duct Inlets on the Performance and Stability of a Jet Engine." ASME Journal of Engineering for Gas Turbines and Power, **138**(022605), February. 11, 26

[14] Weston, D. B., Gorrell, S. E., Marshall, M. L., and Wallis, C. V., 2015. "Analysis of Turbofan Performance Under Total Pressure Distortion at Various Operating Points." ASME Paper GT2015-42879. 13, 48, 49, 58, 63, 64

[15] Fidalgo, V. J., Hall, C. A., and Colin, Y., 2012. "A Study of Fan-Distortion Interaction Within the NASA Rotor 67 Transonic Stage." *ASME Journal of Turbomachinery,* **134**(051011), September. 13, 30, 48, 49, 64

[16] Yao, J., Gorrell, S. E., and Wadia, A. R., 2007. "A Time-Accurate CFD Analysis of Inlet Distortion Induced Swirl in Multistage Fans." AIAA Paper 2007-5059. 13

[17] Hall, K. C., Thomas, J. P., and Clark, W. S., 2002. "Computation of Unsteady Nonlinear Flows in Cascades Using a Harmonic Balance Technique." AIAA Journal 2008-4985, **40**(5). 14, 16

[18] Weiss, J. M., Subramanian, V., and Hall, K. C., 2011. "Simulation of Unsteady Turbomachinery Flows Using an Implicitly Coupled Nonlinear Harmonic Balance Method." ASME Paper GT2011-46367. 14

[19] Custer, C. H., Weiss, J. M., Subramanian, V., Clark, W. S., and Hall, K. C., 2012. "Unsteady Simulation of a 1.5 Stage Turbine Using and Implicitly Coupled Nonlinear Harmonic Balance Method." ASME Paper GT2012-69690. 14, 74

[20] Subramanian, V., Custer, C. H., Weiss, J. M., and Hall, K. C., 2013. "Unsteady Simulation of a Two-Stage Cooled High Pressure Turbine Using an Efficient Non-Linear Harmonic Balance Method." ASME Paper GT2013-94574. 14

[21] Marpu, R., Custer, C. H., Subramanian, V., Weiss, J. M., Hall, K. C., and Clark, W. S., 2015. "Comparison of Numerical Methods for the Prediction of Time-averaged Flow Quantities in a Cooled Multistage Turbine." ASME Paper GT2015-43717. 14

[22] Peterson, M. W., Gorrell, S. E., and List, M. G., 2017. "Fourier Descriptors for Improved Analysis of Distortion Transfer and Generation." ASME Paper GT2017-65031. 17, 23, 26, 28, 57

[23] SAE, 2002. *Aerospace Recommended Practice, Rev. B*. The American Society of Automotive Engineers, Warrendale, PA. 17, 26

[24] Law, C. H., and Puterbaugh, S. L., 1988. Parametric Blade Study Test Report Rotor Configuration Number 4 Air Force Wright Aeronautical Labs, Nov AFWAL-TR-88-2110. 20

[25] Soderquist, D. R., Gorrell, S. E., and List, M. G., 2018. "Radial Variation in Distortion Transfer and Generation through a Highly Loaded Fan Stage." ASME Paper GT2018-77221. 23

[26] Adamczyk, J. D., 1985. "Model Equation for Simulating Flows in Multistage Turbomachinery." ASME Paper 85-GT-226. 30

[27] CD-Adapco, 2015. *STAR-CCM+ User's Manual v11.04.010, Tutorial Guide, Compressible Flow, Turbo Wizard: Multiple Rows*. CD-Adapco. 35

[28] Reid, L., and Moore, R. D., 1978. "Design and Overall Performance of Four Highly Loaded, High-Speed Inlet Stages for an Advanced High-Pressure-Ratio Core Compressor." NASA Technical Paper 1337. 35

[29] Reid, L., and Moore, R. D., 1978. "Performance of Single-Stage Axial-Flow Transonic Compressor With Rotor and Stator Aspect Ratios of 1.19 and 1.26, Respectively, and With Design Pressure Ratio of 1.82." NASA Technical Paper 1338. 35

[30] Denton, J. D., 1997. "Lessons from Rotor 37." *Journal of Thermal Science,* **6**(1), March. 35

[31] Yao, J., Gorrell, S. E., and Wadia, A. R., 2007. A Time-Accurate CFD Analysis of Inlet Distortion Induced Swirl in Multistage Fans AIAA Paper 2007-5059. 48, 64

APPENDIX A. SUPPLEMENTARY PROCESSES

This appendix contains a MATLAB script created to calculate local power variations. The input for this script is 100 csv files containing static pressure data extracted from STAR-CCM+. The output is a 100-element vector that contains the values of power at the 100 locations where data was extracted.

This script requires 100 csv files because there are 20 blades for the rotor geometry, and there are 5 locations of interest on each blade (10%, 30%, 50%, 70%, and 90% span). Each csv file contains static pressure data from a plane that bisects the rotor blades at a specific location. Unfortunately, each csv file contains data for parts of several blades that are intersected, but only the center blade is desired in each case. This script filters all the irrelevant data points out of each csv file. Next, it determines which data points are part of the suction surface and which are part of the pressure surface. Then it sorts the points by axial location so that proper integration can be performed to calculate the overall power generation at the particular location on the particular blade.

The 20 blades are labeled A through T with A corresponding to the blade that is directly counterclockwise of bottom dead center (BDC) when viewed from forward looking aft. This is illustrated in Figure A.1.

A.1 MATLAB Code for Calculating Local Power

```
clc; clear; close all;
%Load in the points to be sorted
%First Column is x value, second column is y value, third column is
%z value, fourth column is static pressure.

blade=18*pi/180;
```

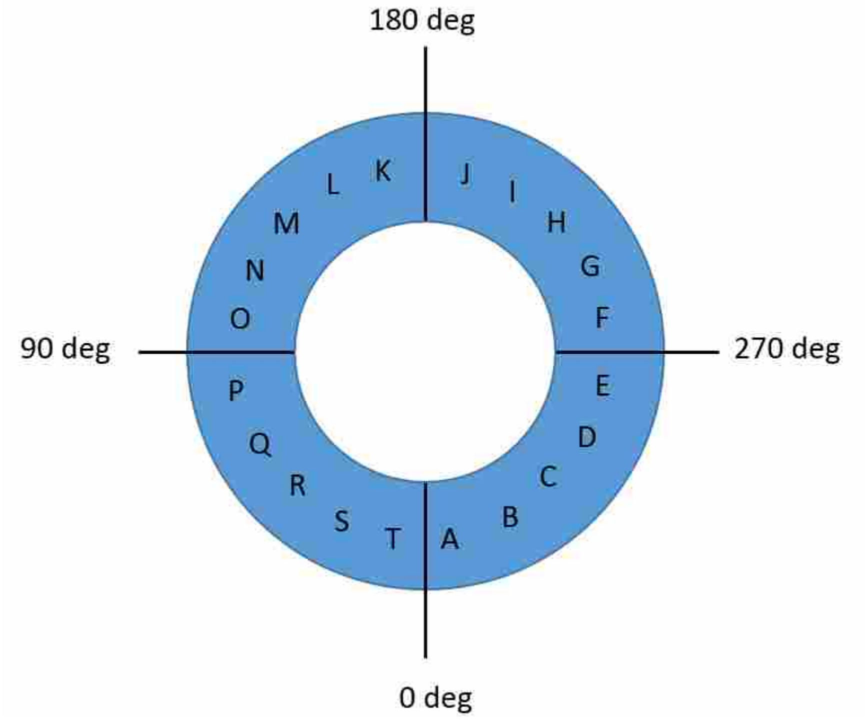

Figure A.1: Convention for the blades in the MATLAB script used for the blade loading method. Each letter is printed in the approximate circumferential location of the leading edge of the corresponding blade. View is forward looking aft.

```
PowerVals=zeros(100,1);

for iter=1:100
    iter
    clearvars -except iter PowerVals blade
    close all;

    if iter==1
        offset=10*blade;
        currentfile= 'ExtractedPressure10pspan_Design_BladeT.csv';
    elseif iter==2
        offset=10*blade;
        currentfile= 'ExtractedPressure30pspan_Design_BladeT.csv';
    elseif iter==3
        offset=10*blade;
        currentfile= 'ExtractedPressure50pspan_Design_BladeT.csv';
    elseif iter==4
        offset=10*blade;
        currentfile= 'ExtractedPressure70pspan_Design_BladeT.csv';
```

```
elseif iter==5
    offset=10*blade;
    currentfile= 'ExtractedPressure90pspan_Design_BladeT.csv';

elseif iter==6
    offset=9*blade;
    currentfile= 'ExtractedPressure10pspan_Design_BladeA.csv';
elseif iter==7
    offset=9*blade;
    currentfile= 'ExtractedPressure30pspan_Design_BladeA.csv';
elseif iter==8
    offset=9*blade;
    currentfile= 'ExtractedPressure50pspan_Design_BladeA.csv';
elseif iter==9
    offset=9*blade;
    currentfile= 'ExtractedPressure70pspan_Design_BladeA.csv';
elseif iter==10
    offset=9*blade;
    currentfile= 'ExtractedPressure90pspan_Design_BladeA.csv';

%%%%%%%%%%%%%%%%%%%%%%%%%%%%%%%%%%%%%%%%%%%%%%%%%%%%%%%%%%%%%%%%%%%%%%%%
%%%% Continue this pattern of elseif statements until iter==100
%%%%%%%%%%%%%%%%%%%%%%%%%%%%%%%%%%%%%%%%%%%%%%%%%%%%%%%%%%%%%%%%%%%%%%%%

elseif iter==91
    offset=12*blade;
    currentfile= 'ExtractedPressure10pspan_Design_BladeR.csv';
elseif iter==92
    offset=12*blade;
    currentfile= 'ExtractedPressure30pspan_Design_BladeR.csv';
elseif iter==93
    offset=12*blade;
    currentfile= 'ExtractedPressure50pspan_Design_BladeR.csv';
elseif iter==94
    offset=12*blade;
    currentfile= 'ExtractedPressure70pspan_Design_BladeR.csv';
elseif iter==95
    offset=12*blade;
    currentfile= 'ExtractedPressure90pspan_Design_BladeR.csv';

elseif iter==96
```

```
        offset=11*blade;
        currentfile= 'ExtractedPressure10pspan_Design_BladeS.csv';
    elseif iter==97
        offset=11*blade;
        currentfile= 'ExtractedPressure30pspan_Design_BladeS.csv';
    elseif iter==98
        offset=11*blade;
        currentfile= 'ExtractedPressure50pspan_Design_BladeS.csv';
    elseif iter==99
        offset=11*blade;
        currentfile= 'ExtractedPressure70pspan_Design_BladeS.csv';
    elseif iter==100
        offset=11*blade;
        currentfile= 'ExtractedPressure90pspan_Design_BladeS.csv';
    end

    rotationSpeedRPM=20200;
    U=rotationSpeedRPM*2*pi/60; %rad/s

span10_YN = strfind(currentfile,'10pspan');
span30_YN = strfind(currentfile,'30pspan');
span50_YN = strfind(currentfile,'50pspan');
span70_YN = strfind(currentfile,'70pspan');
span90_YN = strfind(currentfile,'90pspan');

AllDataUntrimmed=csvread(currentfile,1,0);

P_abs=AllDataUntrimmed(:,1);
Pt_abs=AllDataUntrimmed(:,2);
Coeff_p=AllDataUntrimmed(:,3);
Xvals=AllDataUntrimmed(:,5);
Yvals=AllDataUntrimmed(:,4);
Zvals=AllDataUntrimmed(:,6);

if offset==-5*blade
    for i=1:length(Xvals)
        if Xvals(i)>4
            Xvals(i)=Xvals(i)-2*pi;
        end
    end
end
```

```
clear AllDataUntrimmed
AllDataUntrimmed=[P_abs Xvals Yvals Zvals]; %If looking at static pressure
extra=abs(min(Zvals)-max(Zvals))*.01;
ylimMin=min(Zvals)-extra;
ylimMax=max(Zvals)+extra;
xlimMin=min(Xvals)-extra;
xlimMax=max(Xvals)+extra;
x=xlimMin:.001:xlimMax;

figure()
plot(Xvals,Zvals,'k.')
ylim([ylimMin ylimMax])
xlim([xlimMin xlimMax])
xlabel('x')
ylabel('z')

%Ask the user to click two points to form a line that cuts between the
%airfoil of interest and any points to the left of that airfoil
% PtsLineLeft = ginput(2);
% xL1=PtsLineLeft(1,1);
% zL1=PtsLineLeft(1,2);
% xL2=PtsLineLeft(2,1);
% zL2=PtsLineLeft(2,2);

%Or define and use the values here so you don't need to click everytime.
xL1=1.566966914457551+offset;
zL1=-0.201582170205000;
xL2=1.319625520243483+offset;
zL2=-0.137244617231553;

mL=(zL1-zL2)/(xL1-xL2);
zL=mL*(x-xL1)+zL1;
% hold on
% plot(x,zL,'b',xL1,zL1,'k*',xL2,zL2,'k<');
% ylim([ylimMin ylimMax])
% xlim([xlimMin xlimMax])

%Ask the user to click two points to form a line that cuts between the
%airfoil of interest and any points to the right of that airfoil
% PtsLineRight = ginput(2);
```

```
% xR1=PtsLineRight(1,1);
% zR1=PtsLineRight(1,2);
% xR2=PtsLineRight(2,1);
% zR2=PtsLineRight(2,2);

xR1=1.882721885794660+offset;
zR1=-0.206261264966705;
xR2=1.619592743013736+offset;
zR2=-0.134437160374530;

mR=(zR1-zR2)/(xR1-xR2);
zR=mR*(x-xR1)+zR1;
% hold on
% plot(x,zR,'r',xR1,zR1,'c*',xR2,zR2,'c<');
% ylim([ylimMin ylimMax])
% xlim([xlimMin xlimMax])

%Sort through each point to see if it falls between the two lines the user
%created. If it does, label the index of the point to keep.
k=1;
for i=1:length(Xvals)
    if Xvals(i)>(Zvals(i)-zL1)/mL+xL1 && Xvals(i)<(Zvals(i)-zR1)/mR+xR1
        keep(k)=i;
        k=k+1;
    end
end
AirfoilToKeep=zeros(length(keep),4);
for j=1:length(keep)
    AirfoilToKeep(j,:)=AllDataUntrimmed(keep(j),:);
end
NewX=AirfoilToKeep(:,2);
NewZ=AirfoilToKeep(:,4);
ylimMin=min(NewZ)-extra;
ylimMax=max(NewZ)+extra;
xlimMin=min(NewX)-extra;
xlimMax=max(NewX)+extra;
x=xlimMin:.001:10*xlimMax;

% hold on
% plot(NewX,NewZ,'g.')
```

```
%%
figure()
plot(NewX,NewZ,'g.')
ylim([ylimMin ylimMax])
xlim([xlimMin xlimMax])
xlabel('x')
ylabel('z')

%Ask the user to click two points to form a line that cuts between the
%left and right surfaces of the airfoil. It's okay if it doesn't cut
%through perfectly, just make sure it only divides away points that are on
%the suction surface (convex surface) of the airfoil. Then you can create
%another line below, and another, until you've separated away all but the
%points on the pressure surface (concave surface).
% pause
% PtsLineA = ginput(2);
% xA1=PtsLineA(1,1);
% zA1=PtsLineA(1,2);
% xA2=PtsLineA(2,1);
% zA2=PtsLineA(2,2);

[zA1,IndexMinZ]=min(NewZ);
xA1=NewX(IndexMinZ);

if span10_YN==18
    xA2=1.646834061050959+offset;
elseif span30_YN==18
    xA2=1.674292957898337+offset;
elseif span50_YN==18
    xA2=1.718523831402163+offset;
elseif span70_YN==18
    xA2=1.554086711801775+offset;
elseif span90_YN==18
    xA2=1.72924995684111+offset;
end

if span10_YN==18
    zA2=-0.189829399540004;
elseif span30_YN==18
    zA2=-0.194902961235285;
elseif span50_YN==18
```

```
    zA2=-0.198812499993954;
elseif span70_YN==18
    zA2=-0.172211566830566;
elseif span90_YN==18
    zA2=-0.193332132204947;
end

mA=(zA1-zA2)/(xA1-xA2);
zA=mA*(x-xA1)+zA1;
hold on
plot(x,zA,'b');

%Ask the user to click two points to form another line that cuts points
%away until you've separated away all but the points on the pressure
%surface (concave surface).
% pause
% PtsLineB = ginput(2);
% xB1=PtsLineB(1,1);
% zB1=PtsLineB(1,2);
% xB2=PtsLineB(2,1);
% zB2=PtsLineB(2,2);

if span10_YN==18
    xB1=1.555899037366443+offset;
elseif span30_YN==18
    xB1=1.607125612321258+offset;
elseif span50_YN==18
    xB1=1.619345689178494+offset;
elseif span70_YN==18
    xB1=1.520157324526427+offset;
elseif span90_YN==18
    xB1=1.463432128791109+offset;
end

if span10_YN==18
    zB1=-0.179560939058246;
elseif span30_YN==18
    zB1=-0.187357847191308;
elseif span50_YN==18
    zB1=-0.185939017917350;
elseif span70_YN==18
```

```
        zB1=-0.176268569205495;
    elseif span90_YN==18
        zB1=-0.177293242521097;
    end

    if span10_YN==18
        xB2=1.498362646554728+offset;
    elseif span30_YN==18
        xB2=1.436520146040675+offset;
    elseif span50_YN==18
        xB2=1.394967471293394+offset;
    elseif span70_YN==18
        xB2=1.388410018148186+offset;
    elseif span90_YN==18
        xB2=1.379336331432868+offset;
    end

    if span10_YN==18
        zB2=-0.137741655353957;
    elseif span30_YN==18
        zB2=-0.133753499040377;
    elseif span50_YN==18
        zB2=-0.137311767252598;
    elseif span70_YN==18
        zB2=-0.150452503398324;
    elseif span90_YN==18
        zB2=-0.163485389953022;
    end

    mB=(zB1-zB2)/(xB1-xB2);
    zB=mB*(x-xB1)+zB1;
    hold on
    plot(x,zB,'r');

    %Ask the user to click two points to form another line that cuts points
    %away until you've separated away all but the points on the pressure
    %surface (concave surface).
    % pause
    % PtsLineC = ginput(2);
    % xC1=PtsLineC(1,1);
    % zC1=PtsLineC(1,2);
```

```
% xC2=PtsLineC(2,1);
% zC2=PtsLineC(2,2);

if span10_YN==18
    xC1=1.495560972904143+offset;
elseif span30_YN==18
    xC1=1.439192343708043+offset;
elseif span50_YN==18
    xC1=1.416088822650177+offset;
elseif span70_YN==18
    xC1=1.6569856981850+offset;
elseif span90_YN==18
    xC1=1.622085795627385+offset;
end

if span10_YN==18
    zC1=-0.140188925336403;
elseif span30_YN==18
    zC1=-0.135071545467804;
elseif span50_YN==18
    zC1=-0.141426886826894;
elseif span70_YN==18
    zC1=-0.1871299328280422;
elseif span90_YN==18
    zC1=-0.1808210252968;
end

[zC2,IndexMaxZ]=max(NewZ);
xC2=NewX(IndexMaxZ);

mC=(zC1-zC2)/(xC1-xC2);
zC=mC*(x-xC1)+zC1;
hold on
plot(x,zC,'m');

%Sort through each point to see if it falls outside the lines that
%determine whether it is part of the right or left surface. Depending on
%the answer, label the index of the point that are right or left. Note that
%if the blades have the concave surface on the left, then you may need to
%change the > signs below to < or vice-versa, and change the Right(k) to
%Left(k) etc. in the if statements.
```

```
k=1;
h=1;
for i=1:length(NewX)
    if NewX(i)>(NewZ(i)−zA1)/mA+xA1 && NewX(i)>(NewZ(i)−zB1)/mB+xB1 && NewX(i)>(NewZ(i)−zC1)/mC+
        ↪ xC1
        Left(k)=i;
        k=k+1;
    else
        Right(h)=i;
        h=h+1;
    end
end
RightPoints=zeros(length(Right),4);
for j=1:length(Right)
    RightPoints(j,:)=AirfoilToKeep(Right(j),:);
end
RightX=RightPoints(:,2);
RightZ=RightPoints(:,4);
LeftPoints=zeros(length(Left),4);
for j=1:length(Left)
    LeftPoints(j,:)=AirfoilToKeep(Left(j),:);
end
LeftX=LeftPoints(:,2);
LeftZ=LeftPoints(:,4);

a=iter

figure()
plot(LeftX,LeftZ,'r.',RightX,RightZ,'b.')
ylim([ylimMin ylimMax])
xlim([xlimMin xlimMax])
xlabel('circumferential location (radians)')
ylabel('z')

b=iter

SortedL = sortrows(LeftPoints,4);
SortedR = sortrows(RightPoints,4);

PsL=SortedL(:,1);
XfinL=SortedL(:,2);
```

```
YfinL=SortedL(:,3);
ZfinL=SortedL(:,4);
PsR=SortedR(:,1);
XfinR=SortedR(:,2);
YfinR=SortedR(:,3);
ZfinR=SortedR(:,4);

UR=YfinR*U;
UL=YfinL*U;

HubRadius=[0.025406924896716  0.116918448137126];%m [RotorInlet StatorInlet]
TipRadius=[0.215883957901905  0.215881794640125];%m [RotorInlet StatorInlet]

%The h value should be the same for each span because it
%will always be just 20 percent of the blade height at some axial location,
%so I can just interpolate the hub and tip things.

%Integrate to get work on left surface
insideL=zeros(1,length(ZfinL));
for i=1:length(ZfinL)-1
    m5=-.128546;
    hL=(ZfinL(i)-(-.20789))*m5+.029806;
    insideL(i)=PsL(i)*hL*UL(i);
end
insideL(end)=insideL(end-1);
IntegralOfLeft=trapz(ZfinL,insideL);

%Integrate to get work on right surface
insideR=zeros(1,length(ZfinR));
for i=1:length(ZfinR)-1
    hR=(ZfinR(i)-(-.20789))*m5+.029806;
    insideR(i)=PsR(i)*hR*UR(i);
end
insideR(end)=insideR(end-1);
IntegralOfRight=trapz(ZfinR,insideR);

Power=IntegralOfLeft-IntegralOfRight

PowerVals(iter)=Power;

figure()
```

```
plot(ZfinL,PsL,'r',ZfinR,PsR,'b')
xlabel('axial location (m)')
ylabel('static pressure (Pa)')
ylim([0 175000])
if rem(iter,5)==0
    title(strcat('90% Span'))
else
    title(strcat(int2str(2*rem(iter,5)-1),'0% Span'))
end

%%% Uncomment following to save a file of blade loading for each location
% save(strcat("BladeLoading6Wheels",int2str(iter),'.mat'),'ZfinL','PsL','ZfinR','PsR')

% get(figure(1));
% Figurefile = strcat("BladeLoadingFigure_6Wheels",int2str(iter),'.png');
% saveas(figure(1),Figurefile);


end

save('PowerValues_Blade_T_thru_S_10_to_90_Desgn.mat','PowerVals')
```

APPENDIX B. SUPPLEMENTARY RESULTS

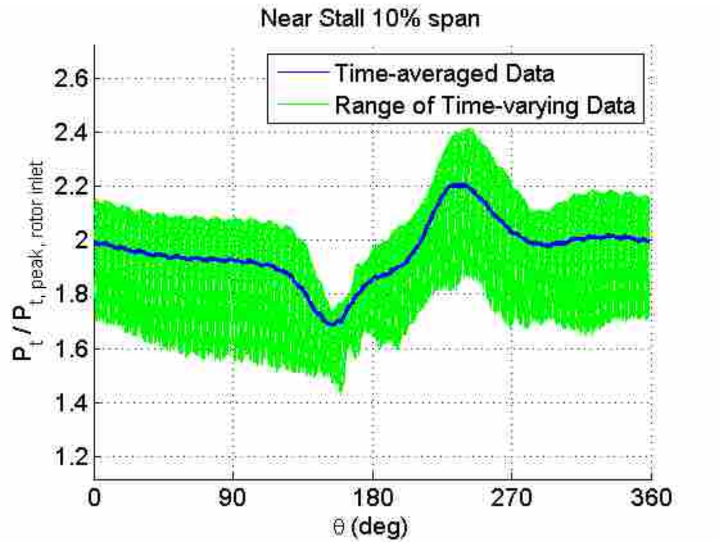

Figure B.1: Time-variation of total pressure at the stator inlet for near-stall data at 10% span.

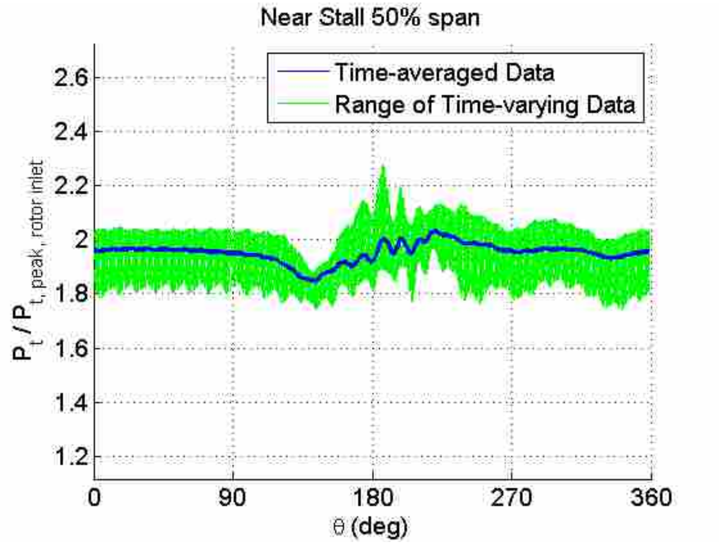

Figure B.2: Time-variation of total pressure at the stator inlet for near-stall data at 50% span.

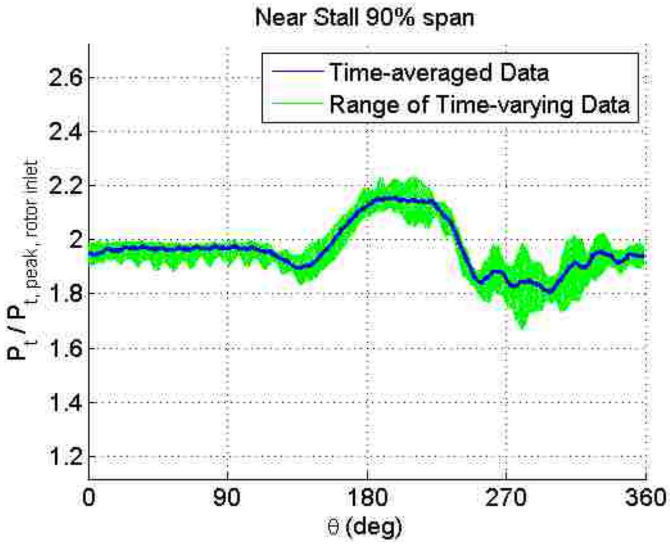

Figure B.3: Time-variation of total pressure at the stator inlet for near-stall data at 90% span.

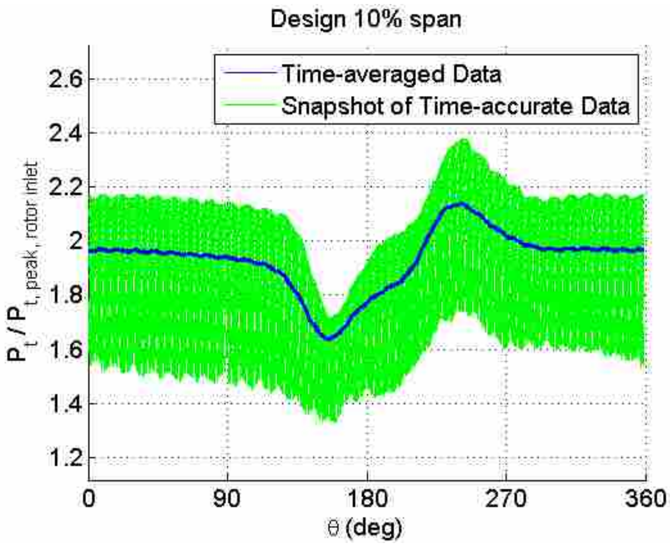

Figure B.4: Time-variation of total pressure at the stator inlet for design data at 10% span.

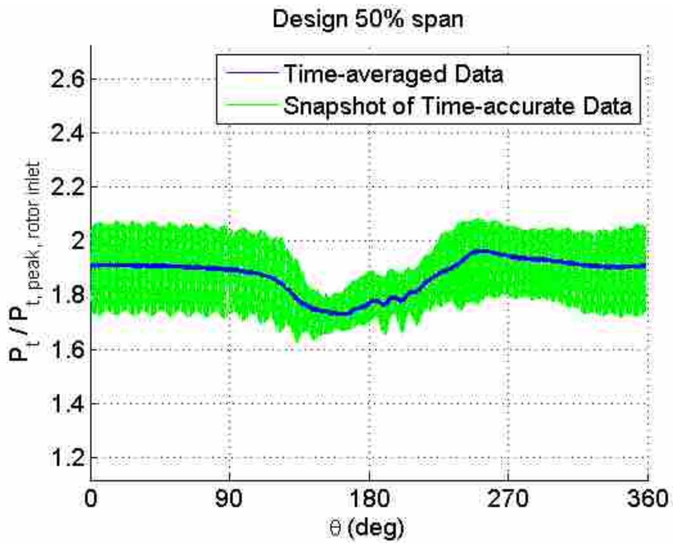

Figure B.5: Time-variation of total pressure at the stator inlet for design data at 50% span.

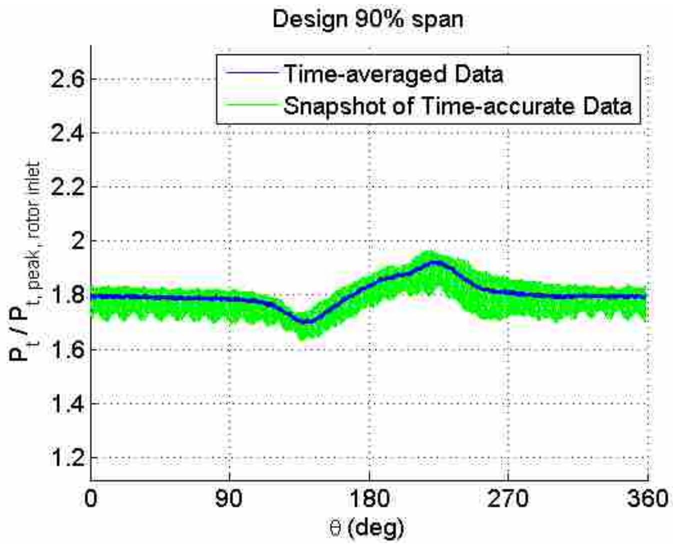

Figure B.6: Time-variation of total pressure at the stator inlet for design data at 90% span.

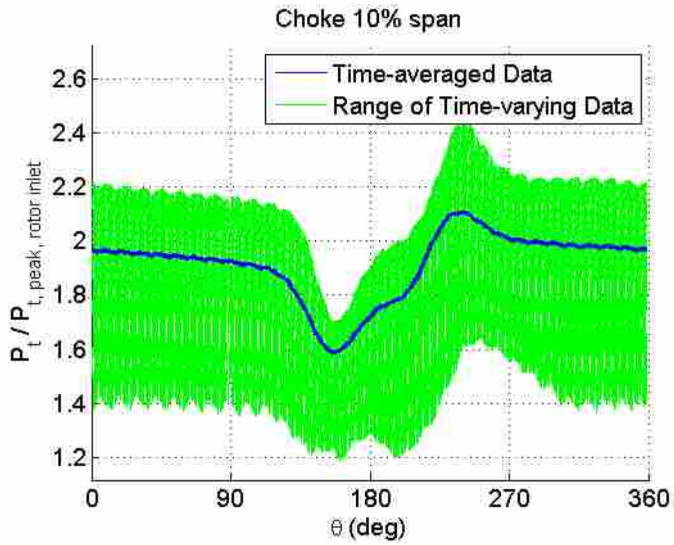

Figure B.7: Time-variation of total pressure at the stator inlet for choke data at 10% span.

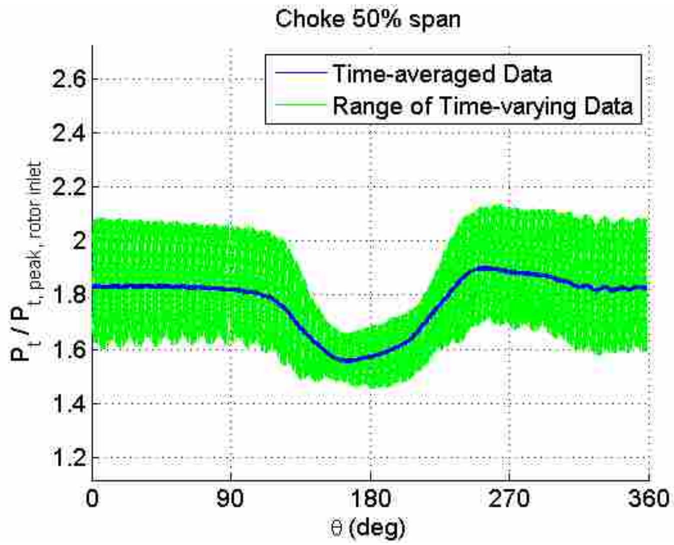

Figure B.8: Time-variation of total pressure at the stator inlet for choke data at 50% span.

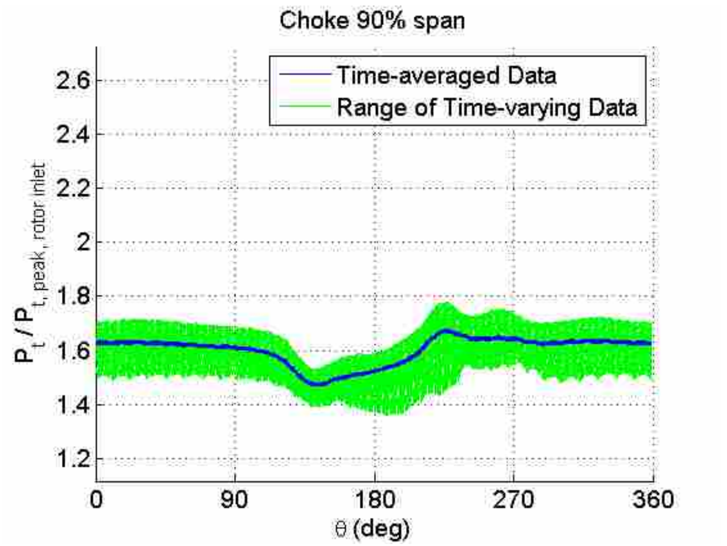

Figure B.9: Time-variation of total pressure at the stator inlet for choke data at 90% span.

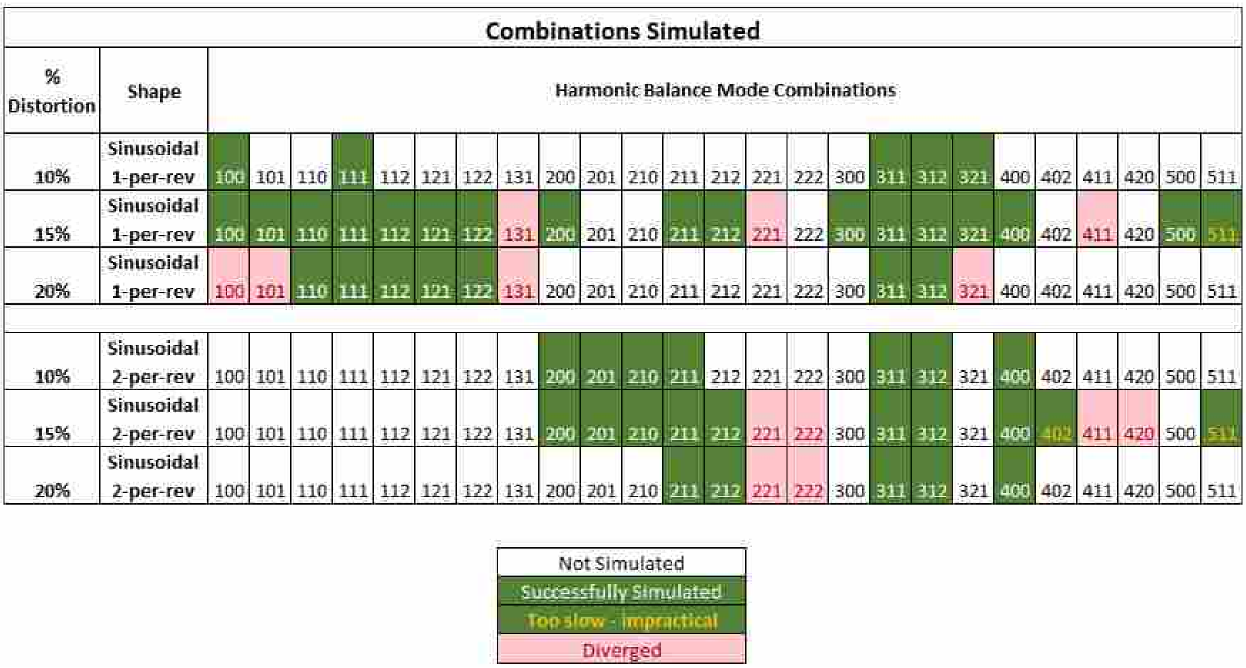

Combinations Simulated

% Distortion	Shape	Harmonic Balance Mode Combinations																								
10%	Sinusoidal 1-per-rev	🟩 100	101	110	🟩 111	112	121	122	131	200	201	210	211	212	221	222	300	🟩 311	🟩 312	🟩 321	400	402	411	420	500	511
15%	Sinusoidal 1-per-rev	🟩 100	🟩 101	🟩 110	🟩 111	🟩 112	🟩 121	🟩 122	🟥 131	🟩 200	201	210	🟩 211	🟩 212	🟥 221	222	🟩 300	🟩 311	🟩 312	🟩 321	🟩 400	402	🟥 411	420	🟩 500	🟨 511
20%	Sinusoidal 1-per-rev	🟥 100	🟥 101	🟩 110	🟩 111	🟩 112	🟩 121	🟩 122	🟥 131	200	201	210	211	212	221	222	300	🟩 311	🟩 312	🟥 321	400	402	411	420	500	511
10%	Sinusoidal 2-per-rev	100	101	110	111	112	121	122	131	🟩 200	🟩 201	🟩 210	🟩 211	212	221	222	300	🟩 311	🟩 312	321	🟩 400	402	411	420	500	511
15%	Sinusoidal 2-per-rev	100	101	110	111	112	121	122	131	🟩 200	🟩 201	🟩 210	🟩 211	🟩 212	🟥 221	🟥 222	300	🟩 311	🟩 312	321	🟩 400	🟨 402	🟥 411	🟥 420	500	🟨 511
20%	Sinusoidal 2-per-rev	100	101	110	111	112	121	122	131	200	201	210	🟩 211	🟩 212	🟥 221	🟥 222	300	🟩 311	🟩 312	321	🟩 400	402	411	420	500	511

Not Simulated
🟩 Successfully Simulated
🟨 Too slow - impractical
🟥 Diverged

Figure B.10: Mode combinations that were simulated for the HB study. For this study, the label "Too slow - impractical" meant that the simulation solve time was on the same order of magnitude or greater than the full-annulus URANS simulation.